UNIVERSITY OF CALIFORNIA,
IRVINE

A Modeling Study of the Biogoechemical Cycling of Iron, Ligands, and Phytoplankton in the Ocean

DISSERTATION

submitted in partial satisfaction of the requirements
for the degree of

DOCTOR OF PHILOSOPHY

in Earth System Science

by

Elliot Michael Sherman

Dissertation Committee:
Professor J. Keith Moore, Chair
Professor Adam Martiny
Professor François Primeau

2016

DEDICATION

To my parents, Kristy Lee and Gerald Sherman, my sister Melanie Sherman, my partner Aimée Gibbons, and my cats Charlie and Bagheera.

TABLE OF CONTENTS

LIST OF FIGURES

LIST OF TABLES

ACKNOWLEDGMENTS

I would like to thank my family and friends for their continual support, and my adviser for his mentorship and guidence.

This dissertation work was supported by a grant to J.K. Moore as a part of the BGC Feedbacks Scientific Focus Area within the Regional and Global Climate Modeling (RGCM) Programin the Climate and Environmental Sciences Division (CESD) of the Biological and Environmental Research (BER) Program in the U.S. Department of Energy Office of Science.This work was also received support from the NSF project Collaborative Research: Improved Regional and Decadal Predictions of the Carbon Cycle (AGS-1048890) awarded to J.K Moore.

CURRICULUM VITAE

Elliot Michael Sherman

EDUCATION

Doctor of Philosophy in Earth System Science **2016**
University of California, Irvine *Irvine, California*

Advanced Study Program Summer Colloquium:
Carbon-Climate Connections in the Earth System **2013**
National Center for Atmospheric Research *Boulder, Colorado*

Master of Science in Earth System Science **2013**
University of California, Irvine *Irvine, California*

Marine Ecosystem Evolution in a Changing Environment summer school **2011**
Middle East Technical University *Ankara, Turkey*

Bachelor of Science in Earth System Science **2011**
University of California, Irvine *Irvine, California*

PROFESSIONAL EXPERIENCE

Graduate Research Assistant **2012 – 2016**
University of California, Irvine *Irvine, California*

SELECT REFEREED JOURNAL PUBLICATIONS

E. Sherman, J.K. Moore, F. Primeau, D. Tanouye, "Temperature influence on community phytoplankton growth rates," *Global Biogeochemical Cycles*, 2016. doi:10.1002/2015GB005272.

CONFERENCE PRESENTATIONS

Sherman, E., Moore, J.K. Ligand-Iron Dynamics and their Influence on Dissolved Iron Distributions in a Global Model. *Talk, Ocean Sciences (2016).*

Sherman, E., Moore, J.K. Explicit Iron-Ligand Coupling in the CESM-BEC. *Poster,Ocean Carbon and Biogeochemistry Summer Workshop 2015.*

ABSTRACT OF THE DISSERTATION

A Modeling Study of the Biogoechemical Cycling of Iron, Ligands, and Phytoplankton in the Ocean

By

Elliot Michael Sherman

Doctor of Philosophy in Earth System Science

University of California, Irvine, 2016

Professor J. Keith Moore, Chair

Iron is a key micronutrient for marine biogeochemistry, limiting growth and nitrogen fixation in over a third of the ocean. However, the impacts of iron-binding ligands and iron source processes on dissolved iron distributions is not well known. The goal of this dissertation is to better understand the cycling of iron-binding ligands and the controls on their distributions and how that impacts dissolved iron. This dissertation also seeks to understand how individual iron sources influence iron distributions and biogeochemistry. To accomplish this, a new prognostic ligand tracer and iron-ligand speciation chemistry are incorporated into the Community Earth System Model (CESM). The CESM is now able to simulate realistic distributions of iron-binding ligands. The results show that with relatively few ligand sources and sinks the model was able to match observations of ligands, and that inclusion of a dynamic ligand tracer improves simulation of dissolved iron. To better understand the influence iron sources have on dissolved iron concentrations and biogeochemistry, sensitivity experiments for each source are conducted with the CESM. The results show that atmospheric dust and sedimentary iron inputs have the largest impact on dissolved iron concentrations and biogeochemistry. Hydrothermal vent inputs are important for deep ocean iron, and their inclusion in global biogeochemical ocean models would allow for more realistic iron simulation.

This dissertation work also reevaluates the parameters governing the temperature influence on community phytoplankton growth rates. A dataset of in situ community phytoplankton growth rates was compiled and parameter values for the Q10 and Arrhenius models were optimized for use in global biogeochemical and ecosystem models. The results show and optimized Q10 value of 1.47 and an activation energy of 0.277 eV. Both the Q10 and Arrhenius models do equally well for estimating the temperature influence on community phytoplankton growth rates against the dataset. Evaluation of global biogeochemical and ecosystem models against our dataset will allow for further constraints on phytoplankton ecology and associated biogeochemitry.

Chapter 1

Introduction

1.1 Background

Iron is a key micronutrient for marine phytoplankton which strongly limits primary production and nitrogen fixation in the oceans (Moore et al., 2004; Hunter and Boyd, 2007). The iron-carbon feedback has been hypothesized to have influenced Earths past climate during the Last Glacial Maximum through alleviating nutrient limitation and strengthening the biological carbon pump (Martin 1990). An in depth understanding of iron cycling processes is necessary to better predict past and future climate on Earth as well as the cycling of other biogeochemical tracers in the ocean. This dissertation focuses on modeling iron cycling processes at the global scale for the contemporary period. New treatments of iron speciation and their impact on dissolved iron and organic ligand distributions are modeled. The relative impacts of iron source processes on dissolved iron distributions, carbon export and nitrogen fixation are also studied though sensitivity simulations. Lastly the influence of temperature on community phytoplankton growth rates is reassessed with new observational data.

Iron is the sixth most abundant element in the Milky Way Galaxy by concentration, and the most abundant element on Earth by mass (Croswell, 1996; Morgan and Edward 1980). The majority of iron on Earth resides in the mantle with an additional 5.6% in the Earths

crust. Iron presents an interesting problem as it is an abundant element most places on Earth but is scarce in the oceans with concentrations ranging from 0.05 - 30 nM (Tagliabue et al., 2010; Mawji et al., 2015). The scarcity of iron in the ocean is due to its low solubility in seawater (Byrne and Kester 1976; Kuma et al. 1996; Liu and Millero 2002). Dissolved iron, defined as less than 0.2 - 0.45 micrometers, can exist in seawater in the oxidation states Fe(II) and Fe(III), as free ions, or complexed with organic or inorganic ligands. Fe(III) is the most thermodynamically stable form of iron in oxic seawater with 96% present in the form of Fe(III) (oxy)hydroxides if organic complexation is not considered (Raiswell and Canfield, 2012). The solubility of inorganically complexed iron in the forms of Fe(III) (oxy)hydroxides is $\sim$0.1 nM. The discrepancy between the solubility of inorganically complexed iron and observed iron concentrations can be explained by considering organic complexation of iron. Greater than 99.9% of iron in seawater is bound to organic ligands (Hirose 2006; Boyd and Ellwood 2010; Buck et al. 2015).

1.2 Ligand Sources and Sinks

Iron-binding ligands are organic molecules that bind with iron and can be most broadly categorized as saccharides (Hassler et al. 2011). More specific chemical characterization of natural ligands in the oceans has not been studied aside from siderophores (Barbeau et al. 2002). Ligands increase the solubility of iron in seawater and reduce losses through precipitation and particle scavenging (Buck et al. 2015). With the majority of iron solubility in seawater due to organic ligands, their impact on dissolved iron distributions and cycling processes is significant. Many hypotheses for ligand cycling processes have been put forth which can be tested through modeling efforts. This dissertation, in part, aims to test the plausibility of some of these hypotheses.

Ligands are detected using the competitive ligand exchange-adsorptive cathodic stripping

voltammetry (CLE-ACSV) method which determines concentration and binding strength (Gledhill and van den Berg, 1994; Gledhill and Buck, 2012). With this method, aliquots of seawater samples are titrated with dissolved iron 10-20 times the original sample concentration and left to equilibrate with ambient iron-binding ligands for several hours. The aliquots are then amended with a characterized competing ligand (CP) of known quantity and left to equilibrate to form Fe(CP)x. The aliquots of the titration are then analyzed by adsorptive cathodic stripping voltammetry using a hanging mercury drop electrode (HDME). A voltage of -0.5V, the reduction potential of iron, is applied to the HMDE. The Fe is reduced from the Fe(CP)x complex and generates a peak in current which is measured by the HDME. The peak is recorded for each aliquot and plotted against the added dissolved iron to generate a titration curve. Linear or non-linear transformations are applied to the titration curve to determine the iron-binding ligand concentration and the associated conditional stability constant. Iron-binding ligands are placed into classes based on the strength of their conditional stability constants where strong binding ligands (L1) have conditional stability constants of log KFeL1 greater than ∼12.0. Weak binding classes, L2 and L3, have conditional stability constants of log KFeL2 = 11-12 and log KFeL3 = ∼11-10.

The current state of iron-binding ligand research is relatively unexplored with only ∼1,200 observations globally, and few studies providing ligand production and removal rates. Most hypotheses regarding ligand sources emphasize the role of biology. Siderophores are some of the strongest iron-binding ligands and are produced by bacteria and cyanobacteria as a strategy to help solubilize dissolved iron under Fe-limiting conditions (Reid et al., 1993; Maldonado et al., 2002; Buck et al., 2010). Studies have also shown ligand production during iron fertilization experiments, hypothesized to be siderophores (Rue and Bruland, 1993; Boye et al. 2005). It should be noted this behavior of producing siderophores under iron replete conditions is contradictory to what has been observed by Malanodo et al. (2002) and Buck et al. (2010). It is possible that increasing iron concentrations via fertilization, could have led to artificially high ligand concentrations as the ligand measurements are based off of iron

concentrations in the samples (Buck et al., 2010). Production of ligands by degradation of organic matter has been quantified by Boyd et al. (2010). They measured the rate of ligand production from bacterial remineralization of sinking organic matter to be 10-4 (mol ligand/mol organic matter). The study sampled at ∼100m, but remineralization of organic matter is likely a source for ligands throughout the water column. More rate measurements are needed to better constrain this rate of production and if the ligand/organic matter ratio is constant throughout the oceans. Sato et al. (2007) observed ligand formation during incubation experiments of microzooplankton and copepod grazing on phytoplankton. They found that the accumulation of ligands was approximately proportional to the decrease in chlorophyll a concentration. Ligand production from phytoplankton grazing likely came from intracellular fluid and ligands imbedded within cellular membranes responsible for iron uptake (Sato et al., 2007). A similar pathway for ligand production has been hypothesized to be viral lysis and colloid formation from senesced phytoplankton, however the rates of ligand production were not quantified (Poorvin et al., 2004; Boye et al., 2001). Production of fluorescent dissolved organic matter and humic substances are also thought be a source of ligands to the ocean with the majority of inputs of humics from rivers (Laglera and van den Berg, 2007; Batchelli 2010; Boyd et al., 2010; Misumi et al., 2013).

There have been many hypotheses put forth for ligand sources but relatively little attention has been given to ligand sink processes. The most studied removal process for ligands is photochemical degradation (Barbeau et al., 2001; 2003; 2006; Powell and Wilson-Finelli, 2003; Rijkenberg et al., 2006, Bundy et al., 2016). This process is restricted to the upper ocean as light attenuates strongly with depth. Results from studies that measured ligand degradation from sunlight have produced mixed results with experiments showing slight increases, no change, and appreciable decreases in ligand concentration. It is also possible that the degradation of ligands from light decreases the conditional stability constant of ligands converting them to a weaker ligand class (Bundy et al., 2016). Biological uptake has also been hypothesized to be a removal pathway for ligands in the upper ocean (Sunda,

1989; Sunda, 2001). As phytoplankton assimilate the iron ligand complex into their cells, the iron is bound to a strong ligand within the cell membrane, and the original ligand is cleaved off. The fate of the original ligand is unknown. It may have been degraded to where it can no longer bind with iron, degraded into a weaker ligand, or may have the same conditional stability constant and able to bind with another iron atom (Boukhalfa and Crumbliss, 2002). Ligands are a component of the dissolved organic carbon pool and are thus thought to be susceptible to removal by bacterial consumption (Voelker and Tagliabue et al. 2014). However there have been no studies that have observed or quantified this process observationally. Observations of this process are critical to understanding ligand cycling in the oceans as it is the only hypothesized removal process operating throughout the water column, and may prove to be an important removal pathway.

How ligand source and sink processes influence ligand distributions in the oceans is not well known because observations are lacking for the both ligand concentrations and ligand cycling processes. We have compiled a database of ligand measurements using the CLE-ACSV method has been compiled from the literature by Sherman and Moore (2016, in prep.), but there are no clear regional trends in the data. While all studies used the same methods, not all studies used the same competing ligand which changed the detection window for ligands (Ibisanmi et al., 2011; Gledhill and Buck, 2012). These studies also did not standardize the definition of ligand classes based on stability constants so many of the reported ligands have overlapping stability constant values. The discrepancies within the measurements make it difficult to differentiate human induced versus natural variability. The recent GEOTRACES program has helped to standardize the methods, procedure and definition of ligands (Gledhill and Buck, 2012; Buck et al., 2015). Ligand data from studies by Buck et al. (2015) and Gerringa et al. (2015) are the first full profile basin transect measurements. Buck et al. (2015) shows relatively constant ligand concentrations between 1 and 2 nM along the GEOTRACES GA03 (east to west transect through mid Atlantic) for L1, L2 and L3 ligand classes. Elevated ligand concentrations are seen along continental margins for the L1 class.

Data from Gerringa et al. (2015) along the GEOTRACES GA02 (north to south transect along the east Atlantic) again showed relatively homogenous concentrations between 1 and 2 nM with slightly higher ligands in the North Atlantic versus the Southern Ocean. Based on current observations, ligand profiles do not fit the profiles of other classic ocean tracer categories: nutrients, scavenged, or conservative. Modeling the cycling processes of ligands and comparing the results to observations can highlight areas of uncertainty and provide insight into what cycling processes drive ligand distributions in the ocean.

1.3 Iron Sources and Sinks

Dissolved iron is operationally defined as being less than 0.2 - 0.45 micrometers and is regulated by multiple source and sink processes in the ocean. Sources for iron include atmospheric dust (Jickells et al., 2005), ocean sediments (Elrod et al., 2004), hydrothermal vents (Bennett et al., 2008; Tagliabue et al., 2010), rivers (Rijkenberg et al., 2014), glaciers (Gerringa et al., 2012) and regenerated iron (Kirchman, 1996). Removal processes include particle scavenging (Nozaki et al., 1987) and biological uptake (Sunda and Huntsman, 1997).

Iron from atmospheric dust primarily comes from the large deserts on Earth and its inputs to the ocean are heterogeneous in space and time. The production of dust depends on the supply of wind-erodible material and from the processes of saltation and sandblasting (Jickells et al., 2005; Prospero et al., 2002). Dust aerosols are typically between 0.1 to 10 micrometer and have a lifetime from hours to weeks, which allows for long range transport of thousands of kilometers (Duce et al., 1995). Models and observations estimate dust inputs at approximately 245 to 450 Tg/year (Jickells et al. 2005; Mackie et al., 2008) with iron at approximately 3.5% of the dust by weight (Duce and Tindale 1991). The majority of dust inputs occur in the Northern Hemisphere with model estimates ranging from 81% to 94% (Mackie et al., 2008). Dust inputs are continuous from the Sahara and Gobi with peaks in the

boreal spring and summer months. Deposition is influenced by atmosphere dynamics such as the oscillation of the intertropical convergence zone and the North Atlantic Oscillation (Prospero et al., 2014; Schlosser et al., 2014; Moulin et al., 1999). Southern hemisphere dust inputs are highly seasonal, peaking in austral summer. The solubility of iron in the dust particles is impacted by transport time, weathering, photochemistry, and acidic pollutants such as NO_x and SO_x (Meskhidze et al., 2003; Sasakawa and Uematsu, 2005; Hand et al., 2004). Combustion products also produce aerosols with a highly soluble fraction of iron (Sedwick et al., 2007; Luo et al. 2008). All of these processes produce large variability in the fraction of iron that is soluble within dust particles. Estimates of dust iron inputs to the oceans range from $2x10^9$ to $1.6x10^{10}$ mol Fe/year (Fung et al., 2000; Jickells and Spokes 2001; Luo et al., 2008; Tagliabue et al., 2016). Dust also likely impacts iron concentrations throughout the water column through slow dissolution of iron from sinking dust particles (Jickells et al., 2005). This process may be facilitated in low pH microenvrionments such as zooplankton guts, within aggregates and via stripping iron from particles by biology (Frew et al., 2006).

Iron inputs from sediments come from resuspended sediment (Johnson et al., 1999) and decomposition of organic matter (Elrod et al., 2004). Iron observations show higher dissolved iron concentrations near shore and off continental margins which decrease towards the center of ocean basins, highlighting the influence of sediment derived iron (Elrod et al., 2004; Moore and Braucher, 2008). A study by Elrod et al. (2004) used benthic flux chambers and found a strong correlation between carbon oxidation and iron flux from sediments. They hypothesize that iron reduction is mediated by carbon oxidation and that reduced iron escapes the sediment (Van Cappellen and Wang, 1996). Estimated iron flux from the continental shelf sediments based on benthic flux chambers are 89 Gmol Fe/year (Elrod et al., 2004) and 109 $\pm$55 Gmol/year (Dale et al., 2015), althought most global biogoechemical ocean models assume a lower input (Tagliabue et al., 2016). The benthic flux chamber estimates likely overestimate the iron flux to the water column, with high scavenging losses near the source.

Hydrothermal inputs of iron may be a significant source of iron to the deep ocean and buffer changes in iron inputs over timescales relevant to Earths climate (Toner et al., 2012; Tagliabue et al. 2010). Estimated inputs of dissolved and particulate iron to the oceans range from 7.2 to 450 Gmol Fe/year (Baker et al. 1993; Bennett et al. 2008; Elderfield and Schultz 1996; Hawkes et al. 2013; Tagliabue et al. 2010). The majority of iron from vents is in the form of iron sulfides and iron oxyhydroxides which precipitate and sink out near the vent sites (Feely et al., 1987; Bennett et al. 2008). However, some iron is stabilized in the dissolved fraction and is able to advect away from the vent site, contributing to the dissolved iron inventory. The mechanisms for stabilization of hydrothermal vent iron remains unknown, but current hypothesis suggest a role for organic complexation by ligands (Bennett et al., 2008; Fitzsimmons et al., 2014; Fitzsimmons et al., 2016). The distribution of vent sites normally occur along spreading ocean ridges and some subduction zones, but observations of active vent fields and iron concentrations near vents are scarce, which makes quantifying this iron source difficult (Baker and German, 2004).

Iron inputs from rivers are of marginal importance for the global iron budget, but are likely a significant source of iron near river mouths and may explain high iron concentrations observed near major river systems (de Baar and de Jong, 2001; Krachler et al., 2005; Rijkenberg et al., 2014). Most river iron is lost via flocculation during estuarine mixing due to changes in pH and ionic strength (Dai and Martin, 1995). River iron sources may be of particular importance for the Arctic Ocean as it is comparatively a small basin by volume with a significant amount of freshwater discharge from Siberian and North American rivers.

The iron sources mentioned thus far refer to new iron inputs, but recycled or regenerated iron is also an important component of the iron cycle. Regenerated iron is unique to other sources as it is strongly mediated by biology. Regenerated iron has been shown to come from zooplankton grazing (Hutchins and Bruland, 1994), remineralization of phytoplankton debris (Lee and Fisher, 1993) and sinking particulates (Lamborg et al., 2008). This rapid recycling

of particulate biogenic iron to bioavailable iron in surface waters by zooplankton, viruses (Mioni et al., 2005) and heterotrophic bacteria (Strzepek et al., 2005) has been termed the ferrous wheel. The ferrous wheel can vary between regions and is thought to depend on the partitioning of iron between biogenic pools (Strzepek et al., 2005). The Fe-ratio (new iron / (new iron + regenerated iron)) quantifies the contribution of new iron to the total iron supply and gives a sense of the role of the ferrous wheel within a system. In high nutrient low chlorophyll waters, where new iron inputs are low, the Fe-ratio has been calculated at $\sim$10% emphasizing the role of the ferrous wheel (Boyd et al., 2005) . Conversely a higher Fe-ratio of 50% has been calculated for regions where new iron inputs are relatively high (Sarthou et al., 2008).

The dominant removal pathway for iron throughout the water column is scavenging by sinking particles. The concentration and flux of sinking particles exerts a strong control on the rate of scavenging such that increasing sinking fluxes generates higher rates of scavenging (Honeyman et al., 1988). Iron, or trace metal scavenging in general, can be described as the reversible exchange between iron and a sinking particle between the dissolved and particulate phases (Nozaki et al., 1987; Honeyman et al., 1988). The proposed mechanism for which this happens is Brownian-Pumping (Honeyman and Santschi, 1989). No observations and few estimates of iron scavenging rates exist (Wu and Boyle, 2002).

An important removal process for dissolved iron in the surface ocean is biological uptake. Phytoplankton require iron for cellular processes such as chlorophyll synthesis, carbon and nitrogen fixation, and electron transport for photosynthesis and respiration (Sunda, 1989; Raven et al., 1999). Inorganically complexed iron, specifically ferric oxides and oxyhydroxides, are not thought to be bioavailable to phytoplankton (Sunda, 1989). Free iron ions or organically complexed iron is available for uptake by phytoplankton (Sunda, 1989). For phytoplankton to take up iron into the cell, iron must first bind to a strong ligand on the cell surface. Bilayer membranes generally prohibit uptake of charged or polar species so chelation

with the transport ligand in the membrane is an important process for cellular uptake and transport. Following complexation with the transport ligand, the original ligand is cleaved and the new iron-ligand complex is taken up by cell. The rate of uptake is described by using MichaelisMenten kinetics.

$$V = \frac{V_{max}[Fe]}{[Fe] + K_s} \tag{1.1}$$

V is uptake rate of iron by the cell, V_{max} is the maximum uptake rate of iron by the cell and K_s is half of V_{max}. The iron quotas in phytoplankton can vary between phytoplankton groups, ocean regions, ambient iron concentrations and are often negatively correlated with light availability (Sunda and Huntsman, 1998; Finkel et al., 2006; Twining and Baines, 2012). Iron quotas are generally highest in non-iron limiting waters (Fe:P = 1.1 mmol/mol) and lowest in the Southern Ocean (Fe:P = 0.2 mmol/mol) (Twining and Baines, 2012 and references within). Variability in iron stoichiometries of marine phytoplankton has been recognized but is not well understood. Further observations are needed to understand variations between ocean regions.

1.4 Iron Distributions

Iron distributions in the oceans are a manifestation of the interactions of the mentioned source and sink processes. In general, iron profiles are a hybrid of a nutrient and scavenged tracer exhibiting characteristics of both. Iron is low in surface waters from biological consumption and particle scavenging. Increases in iron concentration with depth to ∼1000m to 2000m occur from remineralization. Below intermediate depths, iron concentrations gradually reduce which is indicative of scavenging. Large variability is seen in iron observations

and is a reflection of local source and sink processes and iron's relatively short residence time. High iron concentrations (>∼0.6 nM) are typically seen along continental margins which decrease towards the center of ocean basins, exemplifying the influence of sedimentary iron inputs. Observational data, mostly from the recent GEOTRACES campaigns, shows very high iron concentrations near hydrothermal vent sites (> 10 nM) (Mawji et al., 2015). Regions of high dust inputs also exhibit high iron concentrations (Measures et al., 2008). Low iron concentrations in surface waters occur in the North Pacific, Eastern tropical Pacific and Southern ocean due to low iron inputs. It was thought that iron concentrations homogenized in the deep ocean due to constant ligand concentrations of ∼0.6 nM (Johnson et al., 1997). However, data has shown that as in the surface ocean, iron concentrations are variable in the deep as well (Boyd and Ellwood, 2010). The variability of iron throughout the deep ocean (> 2000m) is evident from the recent GEOTRACES campaigns where iron is observed between 0.1 nM to greater than 5 nM (Mawji et al., 2015; Rijkenberg et al., 2014; Resing et al., 2015). Combining the historical iron data compiled by Tagliabue et al. (2010) and the available GEOTRACES data there are ∼23,000 iron observations for the entire ocean. 72% of that data is for the upper 1000m. The number of iron observations is growing, but still more are needed to understand distributions of iron in the oceans.

1.5 Research Objectives

This dissertation seeks to reduce the uncertainties in iron and ligand cycling processes in the ocean using the ocean biogeochemistry component of the Community Earth System Model. The model includes a new ligand tracer with explicit iron-ligand speciation and ligand source and sink processes. The ligand sources and sinks in the model are thought to be the most important for ligand cycling in the ocean and reflect the current knowledge of ligand cycling processes in the literature. Simulated ligand distributions are compared against observed concentrations. These comparisons help to test hypotheses about ligand cycling processes

and their impacts on dissolved iron distributions. As new data and hypotheses come forth, this ligand model can be used by the scientific community to study the cycling of ligands and iron in the ocean.

There is a great deal of uncertainty in the rates of iron source and sink processes. The uncertainties with regards to modeling the iron cycle was evaluated and discussed in the Iron Model Intercomparison Project (FeMIP) (Tagliabue et al., 2016). An outcome of FeMIP was the recognized need to conduct sensitivity experiments varying iron sources in each of the models to better understand each models sensitivity to iron sources. Quantifying the sensitivity for iron sources in each model will allow for a more detailed understanding of the feedbacks between iron and other biogeochemical processes and how they might impact climate. This dissertation expands upon FeMIP and conducts sensitivity experiments varying iron source processes and quantifies the impacts on dissolved iron concentrations and biogeochemical processes.

This dissertation also reassesses the temperature influence on community phytoplankton growth rates (Sherman et al., 2016). A dataset of community phytoplankton growth rates is complied and optimized parameter values for the Q10 and Arrhenius equations are calculated for use in global ocean biogeochemical and ecosystem models. This study found that using a weaker temperature-growth relationship for phytoplankton than is typically used in models produced a better fit to observations. Models that prescribe a stronger temperature-growth relationship may over predict phytoplankton growth response to warming oceans.

Chapter 2

Controls on iron binding ligand distrubtions in the oceans and their impacts on modeling dissolved iron

2.1 Abstract

The majority of iron in the oceans is stabilized in the dissolved pool through complexation with organic ligands. In this study we dynamically model ligands using a global biogeochemical model with explicit ligand source and sink processes to better understand the controls on ligand concentrations and their influence on dissolved iron concentrations in the ocean. The modeled ligand cycle includes a source from particulate organic matter remineralization and dissolved organic matter production. Ligand sink processes include photochemical degradation in the surface ocean, bacterial degradation, biological uptake, and aggregation and scavenging onto sinking particles. Our ligand model is able to reproduce general patterns of observed ligand concentrations along GEOTRACES transects. Model-data mismatch such as regional underestimations and a relatively conservative ligand tracer highlights areas of uncertainty within ligand cycling processes. We compare simulated dissolved iron distributions using a prognostic ligand model, constant ligand model, and implicit ligand model. Inclusion of variable ligand concentrations produces the best simulated iron distributions

compared to observations for the upper ocean. Prescribing a constant ligand concentration (often 1.0 nM) will underestimate iron concentrations in regions of high iron inputs such as continental margins or hydrothermal vents.

2.2 Introduction

It is well known that iron (Fe) is a key micronutrient for phytoplankton in the oceans, limiting growth over one third of ocean area (Moore et al., 2004; Hunter and Boyd, 2007). What remains unclear is how the cycling of iron-binding ligands influence dissolved iron distributions, and what processes control iron-binding ligand concentrations. The solubility of inorganic iron in seawater is extremely low, ∼0.1 nM, compared to measured values of dissolved iron (Liu and Millero, 2002). The relatively high iron measured in the oceans is due to its complexation with organic ligands which reduces losses to precipitation and particle scavenging. The strength of the ligands complexation with iron is quantified through its conditional stability constant. The classification of a ligand into the strong binding class (L1, log KFeL1 >∼12.0) or weak binding classes (L2, log KFeL2 = 11-12; L3, log KFeL3 = ∼11-10) is operationally defined by the conditional stability constant (Gledhill and Buck 2012; Buck et al., 2015). Ligands do not rigidly adhere to one class in a step wise manner based on stability constants, but rather exist across a large spectrum of stability constants (Bundy et al., 2014; Bundy et al., 2016). However, categorizing ligands into classes by stability constants allows for comparisons amongst observations and may provide insights into cycling processes.

The majority of dissolved iron in the oceans is bound to iron-binding ligands of unknown origins. Studies that measured ligand concentrations have provided insights into source and sink processes (Rue and Bruland, 1995). A ligand source for the upper water column comes from bacteria (Martinez et al., 2000; Gledhill et al., 2004). These ligands, called

siderophores, are classified as strong binding ligands due to their high conditional stability constants (Butler, 2005; Hider and Kong, 2010). Weaker binding ligands in the upper water column have been measured from remineralization of sinking organic matter (Boyd et al., 2010), the rupture of phytoplankton cells by viral lysis (Witter et al., 2000; Vong et al., 2007), and zooplankton grazing (Sato et al., 2007). Deeper water column ligand sources are thought to be primarily from humic like substances but may also come from remineralization of sinking organic matter and are more refractory (Laglera and van den Berg, 2007; Batchelli 2010; Boyd et al., 2010; Misumi et al., 2013). A less noted source for deep sea ligands could also be carboxyl-rich alicyclic molecules (Hertkorn et al., 2006). Although sources for ligands have been hypothesized and identified, the relative importance of each source remains almost completely unconstrained.

Relative to ligand sources, there has been less attention given to removal processes. It is not currently possible to conclude how sunlight impacts surface ligand concentrations as studies have produced varied results (Barbeau et al., 2001; 2003; 2006; Powell and Wilson-Finelli, 2003; Rijkenberg et al., 2006, Bundy et al., 2016). Further investigation of this loss process is important for the understanding of ligand and iron cycles as it may be a ubiquitous sink for ligands in surface waters. Loss of ligands via biological uptake is likely another important loss term for ligands in the upper ocean (Sunda, 2001). However it is also likely that the ligand is sometimes released after the uptake of iron and is able to re-bind with another iron atom with the same or weaker conditional stability constant (Boukhalfa and Crumbliss, 2002). The rate of ligand loss, or transformation into a weaker ligand class, is also unconstrained. Iron-ligand complexes in the colloidal size fraction are also susceptible to aggregation and adsorption onto sinking particles. An iron-ligand modeling study by Voelker and Tagliabue (2014) imposed a ligand sink through bacterial degradation. The rate of loss is dependent upon the local ligand concentration in an exponential fashion. In their study a high ligand concentration would yield a short residence time (1 year minimum) and low concentration would yield a long residence time (1000 year maximum). Although no studies have measured

the rate of ligand loss from bacterial degradation, ligands are a component of the dissolved organic carbon pool and are likely susceptible to bacterial consumption (Zweifel et al., 1993; Arnosti et al., 1994).

The inclusion of iron-binding ligands in ocean biogeochemical models has thus far been simplistic, usually with an assumed constant concentration of 1nM (Parekh et al., 2004; Tagliabue et al., 2016). A study by Voelker and Tagliabue (2014) prognostically modeled a generic class of ligands and found it helped to generate a more nutrient like profile for iron but created surface concentrations higher than observed. In this study we simulate dynamic ligand concentrations with explicit sources and sinks using the Community Earth System Model (CESM) ocean component to better understand the cycling of ligands, the controls on their distributions, and their interaction with iron cycling. We compare results from this dynamic ligand simulation with simulations using an assumed constant ligand concentration, and with the implicit ligand approach developed previously for the CESM.

2.3 Methods

2.3.1 CESM-BEC model description

We used the Community Earth System Model Biogeochemical Elemental Cycling model to simulate iron and ligand concentrations (CESM-BEC; Hurrell et al., 2013; Moore et al., 2004; 2013; 2015). The CESM is a global Earth System Model with biogeochemical cycles, atmospheric chemistry and physics and ice sheet dynamics (Hurrell et al., 2013). Further description of the CESM can be found in cited references and model code can be downloaded online (www2.cesm.ucar.edu). The BEC model runs within the Parallel Ocean Program model which is the ocean physics component of CESM (Gent et al., 2011). The Parallel Ocean Program version used in this study has a nominal resolution of 3 degrees with

60 vertical levels. The upper 150m of the model has 10m vertical resolution which thickens with depth to several hundred meters in the deep ocean.

The BEC component includes three phytoplankton functional groups: pico-nano phytoplankton, diatoms and diazotrophs and one adaptive zooplankton group. Dissolved biogeochemical tracers include: organic and inorganic carbon, nitrate, ammonium, silicate, iron, phosphate, oxygen, and alkalinity. The model has been validated against numerous observational datasets (Moore et al. 2002, 2004; Moore and Braucher 2008; Doney et al. 2009b, Long et al. 2013). Moore et al. (2015) contains a more full description of the model and treatment of phytoplankton groups and marine biogeochemical processes.

2.3.2 Iron cycling processes

Iron sources include atmospheric dust deposition, sedimentary diffusion, hydrothermal vents and rivers. These sources are balanced by loss of iron to ocean sediments. A climatological soluble iron deposition to the oceans is used comes from both mineral dust and combustion sources allowing for spatial and temporal variability (Luo et al., 2008). Dust deposition is from the same climatology. Some subsurface release of iron also occurs as the dust sinks though the water column (Moore and Braucher 2008). Rates of sedimentary iron diffusion are a function of the sinking particulate organic carbon flux to the bottom ocean grid (Elrod et al., 2004; Moore and Braucher 2008). Iron inputs from hydrothermal vents occur along mid-ocean ridges at a constant rate of 10 Gmol/year (Beaulieu et al, 2013; earthchem.org). No ligands are released at the vents. The source of iron is prescribed at 300m above the geographic location of the ridge to account for displacement by buoyancy (Tagliabue et al., 2010). Iron input from rivers is set to a constant concentration of 10 nM in the river water as it enters the ocean. The total flux of iron from rivers is 0.33 Gmol/year.

Two pools of iron are considered in the model: dissolved and particulate. The dissolved

fraction represents both dissolved and colloidal iron, which is subject to scavenging by sinking particles. Iron in phytoplankton is routed to either pool through mortality and excretion. The amount of iron routed to the sinking particulate or dissolved pools is dependent on phytoplankton size, where more particulate iron is routed from the grazing mortality of larger phytoplankton than small (Moore et al., 2004; Misumi et al., 2014). All scavenged iron is placed in the sinking particulate pool, and the iron reaching the bottom of the ocean grid is lost to sediments. Physical desorption of iron from particulate iron is also included in the model, and is released as a constant low fraction of the sinking particulate iron flux.

2.3.3 Description of iron-ligand models

In this study we use three variations of the CESM-BEC where we modified iron cycling processes. We define the Explicit Dynamic ligand model as having explicit iron-ligand speciation, dynamic ligand sources and sinks, and variable ligand concentrations. We set a relatively high scavenging rate for iron in the excess of ligand concentration (the rate is 25 times the rate for bound iron) based on the assumption that much of this iron would be bound to weaker ligands. Previous model studies often assumed much higher rates for "free" iron, sometimes instantaneous removal (i.e, Archer et al., 2000; Parekh et al., 2004). This "free" iron scavenging parameter allows dissolved iron to sometimes exceed the ligand concentration in areas of high iron inputs. The Explicit Constant ligand model is defined by explicit iron-ligand speciation with a constant generic ligand concentration of 1.52 nM, which is the average ligand concentration in the Explicit Dynamic model control simulation. This treatment of ligands, with a constant concentration, is in the fashion of Parekh et al. (2004), where any iron exceeding the ligand concentration is rapidly removed. The Implicit ligand model has no explicit simulation of iron-ligand speciation or ligands, but includes the impact on iron solubility through the scavenging parameter. An implicit ligand concentration of 0.8 nM is assumed with increased rates of iron scavenging above 0.8 nM, and reduced rates of

scavenging below 0.8 nM (Moore and Braucher, 2008; Moore et al., 2013). This is meant to capture increased scavenging and iron oxidation as iron exceeds the implicit ambient ligand concentration. All model parameters for the Explicit Dynamic and Explicit Constant are the same; the only difference is in the treatment of ligands. The iron scavenging parameter in the Implicit model was tuned independently of the Explicit ligand models, but all other model parameters are equal.

2.3.4 Ligand source and sink processes

Explicit simulation of iron binding ligands was incorporated into the CESM-BEC model. Due to discrepancies in the procedure for measuring ligands and lack of observational constraints it is challenging to model multiple ligand classes with any certainty (Ibisanmi et al., 2011; Voelker and Tagliabue, 2014). The Explicit Dynamic model considers one strong ligand class. Ligand concentrations are variable in space and time and are a function of source and sink processes. The ligand source is set as a constant proportion of remineralized particulate organic carbon (POC) and dissolved organic carbon (DOC) production. This value is 10^{-4} (mol ligand/mol organic carbon) and is from studies by Boyd et al. (2010) and Wagener et al (2008). The conditional stability constant for the iron-ligand complex is 10^{13} (M^{-1}) (Gledhill and Buck, 2012; Buck et al., 2015).

Ligand sink terms include scavenging of iron-bound ligands, biological uptake of bound ligands, bacterial consumption/degradation and photochemical degradation of free and bound ligands. The scavenging is a function of the sinking mass particle flux which includes, POM, $CaCO_3$, SiO_2, and dust. The model does not differentiate between colloidal and dissolved iron pools. We impose a weaker scavenging rate for iron that exceeds the simulated ligand concentration in order to represent the spectrum of weaker ligands subclasses such as L2 and L3 ligands without the additional computational expense of adding other tracers. This parameter is insensitive to the iron bound to the explicit ligand, but is sensitive to iron that

exceeds the local ligand concentration.

As the phytoplankton consume the iron-ligand complex, we assume 24% of the ligands are destroyed by the uptake process and the remaining ligands are released back into the ocean able to rebind with another iron atom.

$$\textit{bacterial ligand degradation} = \textit{POC remineralization rate} \cdot \textit{scaling factor} \tag{2.1}$$

Bacterial ligand degradation in our model is a function of POC remineralization. We assume that POC remineralization rates are a proxy for heterotrophic bacterial activity. Areas of high POC remineralization lead to high rates of organic ligand degradation and low remineralization rates would cause less ligand degradation building on correlations between primary production, remineralization rates and bacterial biomass (Cole et al., 1988; Ducklow, 2000; Obernosterer et al., 2008).

$$\textit{photochemical degradation} = \textit{[Ligand]} \cdot \textit{PAR} \cdot \textit{reference liftime} \tag{2.2}$$

Our photochemical degradation parameter follows that of Voelker and Tagliabue et al. (2014). Photochemical degradation of ligands occurs only in the surface layer of the ocean as UV radiation attenuates rapidly with depth. We use photosynthetically active radiation (PAR) as a proxy for UV radiation. The rate of degradation is a function of PAR where PAR is greater than 1.0 W/m^2. This product is then scaled to give a minimum surface lifetime of three months (Barbeau et al. 2003, Schlosser & Croot 2009).

Ligand parameters were optimized by comparing against ligand data from Buck et al. (2015),

ligand observations compiled from published experiments, and by comparing resulting simulated iron against the Tagliabue et al. (2012) observational dataset and iron data from GEOTRACES (Mawji et al., 2014). In sum, a dataset of 1,125 ligand observations using the competitive ligand equilibration and absorptive cathodic stripping voltammetry was compiled. The dataset contains iron binding ligand concentration, geographic location, depth, conditional stability constant and iron observations in every ocean basin except the Arctic. The data from Buck et al. (2015) (452 observations) used consistent procedures with the same analytical window, while the compiled dataset (1,125 observations) used the same method with different procedures, analytical windows and different definitions of ligand based on conditional stability constants.

2.3.5 Model experiments

Model simulations using the three variations of the CESM-BEC are conducted to elucidate how the treatment of ligands impacts dissolved iron distributions. The constant ligand concentration used for the Explicit Constant model is the average concentration of ligands in the Explicit Dynamic model. Using the average value from the Explicit Dynamic model simulation of 1.52 nM, as opposed to using a constant 1.0 nM as described in Parekh et al. (2004) and Tagliabue et al., (2016), will produce a more direct comparison of the impacts of ligand concentration on dissolved iron distributions between the Explicit Dynamic and Explicit Constant models. We increase the "free" iron scavenging parameter for the Explicit Constant model to rapidly remove iron above the ambient ligand concentration, to replicate what is done in Parkeh et al. (2004) and other biogeochemical models (Tagliabue et al. 2016). We also conduct sensitivity experiments varying the desorption rate of iron from particulate iron by a factor of ± 10 of the optimized value, and the "free" iron scavenging parameter by a factor of ± 10 using the Explicit Dynamic model. All parameters between the three models are the same and only the treatment of ligands differ. Simulations are run

for 310 years and results are computed from the average of the last 20 years of simulation. The length of the simulation is sufficient for upper ocean biogeochemical fluxes and pools to approach a steady state.

2.4 Results

2.4.1 Ligand and dFe distributions in the Explicit Dynamic model

Figure 2.1 compares simulated ligand distributions from the Dynamic Explicit model averaged over specified depth intervals and ligand observations from Buck et al. (2015) and observations from the literature. Simulated ligand concentrations correlate with primary productivity for the upper ocean. The North Pacific and Eastern Equatorial Pacific exhibited ligand concentrations of ∼2 nM in the upper 100m. The Eastern Equatorial Pacific has the highest concentration at ∼2.25 nM. Lower ligand concentrations are seen in the Southern Ocean and South Atlantic between 1 and 1.75 nM. The lowest simulated concentrations are in the Sargasso Sea at between 0 and 1 nM. Low concentrations of 0.5 to 1 nM are seen in the Indian Ocean, North Atlantic and Arctic. Below 100m the pattern of ligand distributions begins to homogenize with concentrations ranging between 1 and 2.25 nM. The highest concentrations are again seen in the Eastern Equatorial Pacific. Below 1000m ligands generally vary between 1.25 and 2 nM. Note that in the North Atlantic transect from Buck et al. (2015) there is a similar upper-ocean pattern, with elevated ligand concentrations along the more productive continental margins.

Figure 2.2, left panels, compare BEC simulated ligands to measured L1 ligands along the GEOTRACES GA03 transect (Buck et al. 2015). The model is able to reproduce the general concentrations of L1 ligands along this transect, but does not reproduce some key features. Buck et al. (2015) found relatively uniform ligand concentrations of ∼1.3 nM along the

transect with higher concentrations of ∼2 nM near continental margins and greater than 4 nM at the TAG hydrothermal vent site. The BEC did not simulate the high concentrations near continental margins and TAG vent site. The model underestimates ligand concentration along the transect by an average of -0.37 nM. Overestimation of ∼0.3 nM occurs between 300-700m. Table 1 compares simulated ligand against three ligand datasets: historic data from published literature values, L1 and L2 data from Buck et al. (2015). The simulated ligands from the Explicit Dynamic model matched L1 data from Buck et al. (2015) well based on correlation coefficients and root mean square error values. The model also compared reasonably well against the L2 data. Comparing ligand observations with the constant 1.52 nM ligand concentration simulation results slightly smaller rms errors for L1 than the Explicit Dynamic model, but larger rms errors for the L2 (Table 1).

Figre 2.2, right panels, compare simulated dFe versus observed along the GEOTRACES GA03 transect. The model slightly overestimates iron along this transect, but it is generally able to capture the major patterns of dissolved iron. The BEC simulates low iron in surface waters which increase with depth due to remineralization. The model also captures higher iron concentrations seen on the western portion of the transect from remineralization and sedimentary sources (Buck et al., 2015). The placement of iron from the Saharan dust plume on the eastern portion of the transect is simulated well, but underestimations of iron concentration of ∼1 nM are seen between 200m to 800m. Underestimations by the model of ∼0.5 nM are seen in the dust plume between 2000m and 3000m. The BEC simulates the placement of the hydrothermal vent plume well (between 50°W and 40°W below 3000m), but it underestimates the concentration. The model simulates hydrothermal plume concentrations approaching 2 nM, but observed concentrations are greater than 30 nM (Buck et al., 2015; Mawji et al., 2014). Simulating such high iron concentrations near vent sites is challenging as the mechanism for iron stabilization is unknown. The leading hypothesis for iron stabilization in the dissolved fraction at vent sites suggests the role of ligands. The BEC does not currently include a ligand source at hydrothermal vents, but future research

efforts include implementing a ligand source at vent sites to test this hypothesis. Of the three models used in this study, the Explicit Dynamic ligand model produced the best correlation and lowest rms error to observed iron along this transect.

2.4.2 Comparison of dissolved iron distributions from Explicit Dynamic, Explicit Constant, and Implicit models

All three models produce similar patterns of dissolved iron distributions for the upper 1000m with the Explicit Dynamic model capturing more of the high-end variability in iron concentrations throughout the water column (Figure 2.3). All models are able to simulate iron-limiting concentrations in the HNLC regions and high iron near continental margins and in areas of high dust deposition. The Explicit Dynamic model produces the highest correlation to observed iron (r = 0.389) and lowest root mean squared error (rmse = 0.733) of the three models tested for the upper 100m (Table 2). In the upper 100m the Explicit Constant model overestimates iron in the Arctic and in regions of high dust deposition like the Atlantic and Indian Oceans. Below 1000m both the Dynamic Ligand and Constant Ligand models underestimate iron in the North Pacific and overestimate in the North Atlantic and Arctic. The Implicit model produces more homogenous iron distributions at an average of 0.69 nM with modest overestimation in the Southern Ocean. The Implicit model is also rarely simulates iron concentrations above 2 nM seen near continental margins and hydrothermal vents. The Explicit Constant ligand model rarely produces iron concentrations greater than 1.52 nM as iron is rapidly scavenged when it exceeds the local ligand concentration. This tight lid on iron concentrations is apparent in Figure 2.4, which depicts scatter plots of observed versus simulated iron using the raw data and regionally binned data within 30x30 degree grid boxes.

2.5 Discussion

2.5.1 Ligand distributions in the Explicit Dynamic model

Surface ligand distributions generally follow patterns of chlorophyll and sinking carbon export for the surface ocean as remineralization of POC and DOC are the sources of ligands in the model. The low ligand concentrations simulated in the Sargasso Sea are a result of overly strong phosphorus limitation, which leads to little carbon export, remineralization and ligand production. Below 100m ligand concentrations and distributions homogenize with little variability within ocean basins. A peak in average ligand concentration is seen at intermediate depths coinciding with increased remineralization of organic matter, and reductions in loss rates compared to surface waters. The homogenous distribution in the deep is largely due to a balance between ligand production and bacterial degradation. The additional removal processes and variability in phytoplankton production cause variability in ligand concentrations in the surface ocean.

Ligand concentrations in the surface ocean are sensitive to the phytoplankton degradation parameter in regions where iron-ligand, also known as dissolved iron, concentrations are relatively high because only the iron-ligand complex is directly impacted by the phytoplankton degradation parameter. The pattern and degree of change in ligand concentration is governed by the iron-ligand concentration and its availability to phytoplankton. In regions where iron concentrations are relatively low, this parameter has little impact on ligand concentrations. Observational constraints on the fraction of degraded ligand from iron uptake by phytoplankton would help constrain the upper ocean ligand budget.

The photochemical degradation is also a sensitive parameter for the surface ocean. This parameter is most sensitive where ligand concentrations are high and where photosynthetically active radiation is high. Experiments have observed photochemical degradation of various

ligand classes (Barbeau et al., 2003; Powell and Wilson-Finelli 2003; Schlosser and Croot 2009). The average rate of loss of ligand from photochemical degradation in the Explicit Dynamic control simulation is 4.78 nM/year in the surface layer. Powell and Wilson-Finelli (2003) conducted incubation experiments exposing sea water to sunlight and observed the degradation of ligands. Our simulations show much slower removal of ligands from photochemical degradation compared to their experiments. However, some of their experiments also showed little change or even increases in ligand concentration making the comparison challenging to interpret. It is likely we are missing additional ligand sources in the surface ocean such as siderophore production or viral lysis which could cause us to bias the photochemical loss parameter high to an unknown extent. Further rate constraints on this process and other ligand cycling processes would help to show the relative importance of ligand cycling processes on ligand and iron distributions in the ocean.

Comparing simulated and observed ligands along the GEOTRACES GA03 transect highlights regions of model error and provides insight into possible causes. Given what is known about ligand sources one might expect to see something similar to a profile of dissolved organic carbon, however this is not what is observed by Buck et al. (2015). The BEC underestimates ligands along this transect. Increasing the ligand production rate could have helped produce a better match to observations, but would have deviated from measurements of ligand production rates by Boyd et al. (2010). It is possible the model is missing a ligand source from humic substances or CRAM which would alleviate some of the underestimation. The model underestimates ligands at continental margins while capturing high POC flux in the upwelling region off the West African coast and Eastern North America. Observations show sustained ligand concentration greater than 2 nM at continental margins down to 4000m. Table 2 shows the comparison of modeled ligands versus observed ligands for L1 and L2 data from Buck et al. (2015). Simulated ligands correlate better with the L1 class than the L2 class while exhibiting similar errors. This suggests the simulation of our ligands are able to partially capture the distribution patterns of both L1 and L2 classes. Prognostic

simulation of ligands as described in this study is a more realistic way to represent ligands in the ocean than a constant ligand value, and may simulate better distributions under changing climate and biogeochemical conditions.

Gerringa et al. (2015) measured ligands along the GEOTRACES GA02 transect and found heterogeneous distributions with a general pattern of decreasing ligands from the North Atlantic to the Southern Ocean. Simulated ligands along the GA02 transect produced a pattern that mostly follows the major water masses, indicative of a relatively conservative tracer. The simulated ligand residence time below 2000m in the North Atlantic is 305 years, sufficient time to follow North Atlantic Deep water south of the equator (Gebbie and Huybers, 2012). Simulated ligands along the GA02 transect appear too conservative compared to distributions from Gerringa et al. (2015), and our model is likely missing source and sink processes that would help contribute to the variability seen in the observations. The observed decreasing ligand concentration in the NADW indicates greater removal of ligands than supply. It is possible we underestimate the removal of ligand from bacterial degradation or scavenging relative to supply within the NADW, or that ligands exhibit rates of removal similar to some first order decay process. Gerringa et al. (2015) also observed no increase in ligand concentration in the oxygen minimum zone between 20°S and 20°N, where we simulated the highest ligand concentrations along the transect. It is also possible we are overestimating ligand production from organic carbon remineralization. However this could contradict our previous statement of underestimating removal because underestimating removal from bacterial degradation has the same effect as overestimating ligand production. Without further observational rate constraints on ligand source and sink processes its difficult to discern whether we are overestimating ligand production or underestimating ligand removal.

We also compare simulated ligands against a database of observed ligand concentrations using the competitive ligand equilibration and absorptive cathodic stripping voltammetry

(CLE-ACSV) (Gledhill and Van den berg, 1994; Rue and Bruland, 1995). Figure 2.1 and Table 2.1 compares averaged simulated and observed ligand over specified depth ranges. The observations show no clear trend with depth and concentrations are highly variable. The lack of trend and high variability are likely due to inconsistencies in method procedures between studies, but biases in sampling locations or seasonal variability may also play a role. All studies in the dataset used the CLE-ACSV method, but not all studies used the same competing ligand or had the same side reaction coefficient, which determines the detection window (Ibisanmi et al., 2011). Varying detection windows amongst studies could partially explain the highly variable ligand concentrations, and lack of consistent patterns. Many of the studies also defined the ligand class using different conditional stability constants making it difficult to compare the results of one study against one another or a specific modeled ligand class. The discrepancies amongst the methods make it challenging to assess model performance. There must be more consistency in the competitive ligand and detection window used and a standard definition of ligand classes based on conditional stability constants to better document trends in ligand concentration and for model validation.

2.5.2 Comparison of model iron simulations

All models, with their different implementation of ligands, were able to reproduce realistic iron distributions for the upper ocean with the Explicit Dynamic and Implicit models performing better than the Explicit Constant model at nearly all depths (Figure 2.4 and Table 2.2). Any implementation of ligands described in this study will allow for simulation of realistic contemporary iron distributions. However, the Explicit Dynamic model best captures high iron concentrations near continental margins and at hydrothermal vents. This is in part due to the "free" iron scavenging parameter which is meant to capture the reductions in iron removal from adsorption and scavenging for the weaker spectrum of ligands we do not explicitly simulate. Implementing our "free" iron scavenging parameter using the Explicit

Constant model would allow for simulation of high iron concentrations in regions where iron fluxes are high and would likely produce iron concentrations more similar to the Explicit Dynamic model. The Implicit model also captures high iron concentrations by increasing rates of scavenging as a function of increasing iron concentration above a threshold of 0.8 nM (Moore et al., 2004; Moore and Braucher, 2008). Some representation of variable ligand concentration, whether explicit or implicit, helps to improve simulation of dissolved iron distributions and variability. Prescribing a constant ligand concentration without representing the weaker spectrum of ligands sets and upper limit on simulated iron concentrations (Figure 2.4). Current hypotheses for ligand sources and sinks emphasize the role of biology. Inclusion of variable ligand concentrations for different climate scenarios will allow for the simulation of more realistic iron concentrations and associated feedbacks between iron, ligands, biology and other biogeochemical tracers. Prescribing a constant ligand concentration in a biogeochemical model not only sets an upper limit on the dissolved iron concentration, but also on the potential total iron inventory in the ocean. This may be problematic if one were to use a biogeochemical model with constant ligand concentration for a paleoceanographic or future climate change scenario study, where the iron inventory and concentrations could be drastically different.

Simulation of NPP was 49.9 (PgC/year) for the Explicit Dynamic and 50.0 (PgC/year) Explicit Constant models. The implicit model produced a similar NPP of 52.2 (PgC/year). The increase in production occurred in the Central Pacific and northern boundary of the Southern Ocean. The Explicit Dynamic and Explicit Constant models both produced export production values of 7.41 (PgC/year), and the Implicit model produced an export production of 7.74. The increase in export production occurred from the increase in NPP. The relatively small difference in the export ratio shows that the treatment of ligands between models had little to no effect on phytoplankton community composition. The simulated concentrations and distributions of iron were similar enough to produce very small differences in the biological response for the contemporary period. Using any treatment of ligands described in this

study will likely produce little change in the biogeochemical response for the contemporary period, but might give markedly different distributions under another climate/productivity state.

2.5.3 Desorption sensitivity experiments

Increasing desorption by a factor of 10 increased dissolved iron inventories by 68% from the control experiment (Figure 2.5). This is partly because there is no upper limit to the amount of iron adsorbed onto sinking particles which creates a large reservoir of iron in the particulate pool in the model. Particulate iron represents a large fraction of iron in the oceans, but further constraints are needed on the rate of desorption of dissolved iron from particulate iron and on the amount of particulate iron in sinking particles. The uncertainty associated with this process could lead to overestimation of iron removal processes in models, further confounding the rates of sources and sinks for iron. The uncertainty of iron cycling parameters was explored by Tagliabue et al. (2016) and this sensitivity experiments highlights another uncertain parameter. Reducing the desorption rate of iron showed a much smaller impact relative to the experiment increasing desorption. The iron inventory decreased by 9.3% when desorption was decreased. Both experiments showed the most significant change in iron concentration deeper in the water column, greater than 1000m.

2.5.4 "Free" iron scavenging sensitivity experiments

The "free" iron scavenging parameter allows for an implicit inclusion of the broad spectrum of weaker ligand classes not explicitly simulated. This parameter is only sensitive where iron is above the ligand concentration due to strong input fluxes, which is most often near hydrothermal vents or continental margins. Increasing the "free" iron scavenging parameter by a factor of ten removed nearly all iron above the ambient ligand concentration, decreasing

the iron inventory by 2.8% compared to the control run. The model was not able to capture the high iron concentrations seen in observations with such strong scavenging. Decreasing this parameter had the opposite effect, producing higher iron near continental margins and along hydrothermal vents. Decreasing the "free" iron scavenging parameter by a factor of ten increased the iron inventory by 15.5% compared to the control run. Not all of this excess iron is scavenged away locally, circulation and mixing moves some iron out of the high input regions to where iron concentrations are less than the ligands. Inclusion of the "free" iron scavenging parameter would be useful in models that assume a constant ligand concentration. It would help capture the impact of high iron concentrations in regions where iron inputs are high and exceed strong ligand concentrations.

2.6 Conclusions

Our study provides insight into ligand cycling processes and their impacts on dissolved iron in the oceans. We are able to reasonably match observed ligand concentrations with few source and sink processes. Comparing our modeled results against ligand data from the GEOTRACES GA02 and GA03 shows that our current understanding of ligand cycling processes is not enough to fully recreate what is observed, but does highlight areas of uncertainty which can guide future research (Gerringa et al., 2015; Buck et al., 2015). Our ligand tracer appears to be too conservative and it is likely we are missing additional source and sink processes.

Inclusion of varying ligand concentration, whether explicit or implicit, improves simulation of dissolved iron distributions. Ocean biogeochemical models should work towards including some non-static representation of iron binding ligands. Implementing a constant ligand concentration sets a hard upper limit on iron concentrations. The inability to capture variability in iron concentrations could lead to inaccuracies in simulation of past and future

climate scenarios. Further observational constraints on ligand source and sink processes and more ligand observations would greatly help future modeling efforts. The high resolution measurements from the GEOTRACES campaigns are ideal for evaluating model results and will be instrumental in future ligand and iron cycling model development.

2.7 Figures

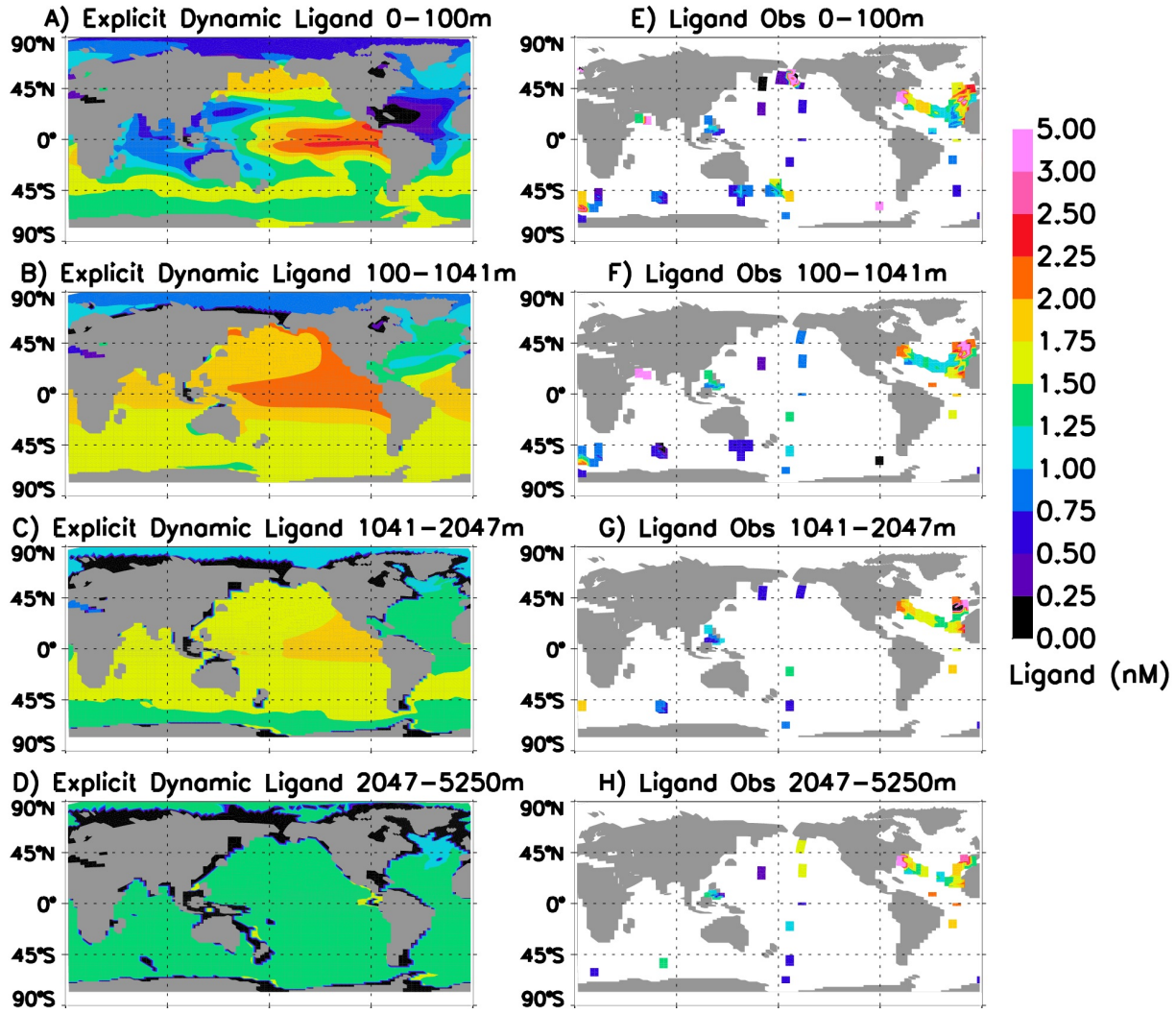

Figure 2.1: Left panels (A-D) show the averaged simulated ligand concentration over the specified depths. Right panels (E-H) show observed ligand concentrations.

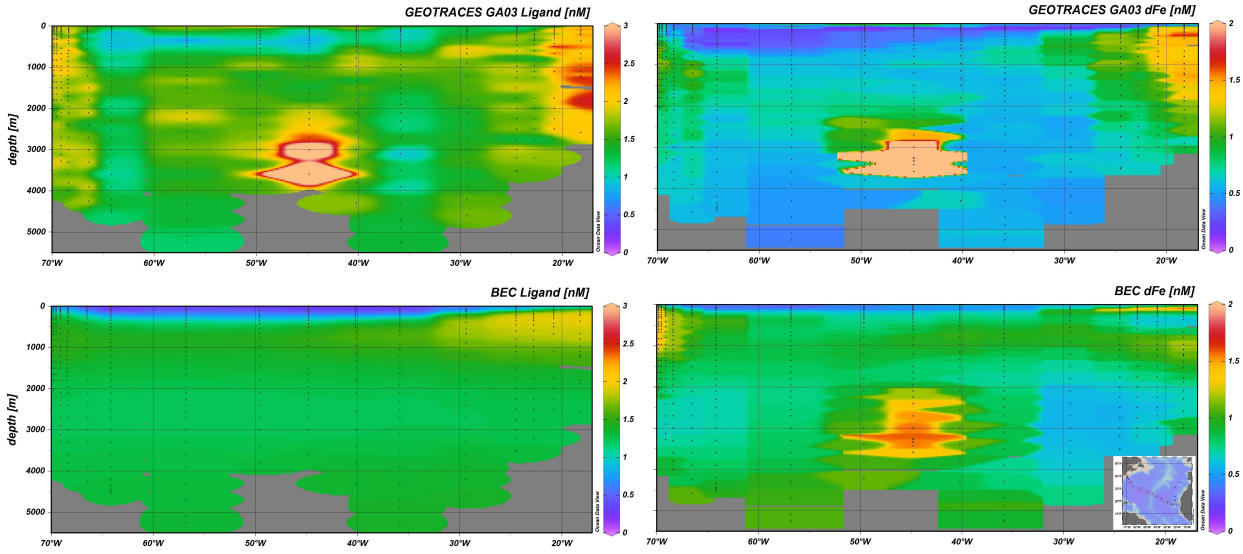

Figure 2.2: Top left panels shows observed ligand concentrations along the GEOTRACES GA03 transect (Buck et al., 2015). Bottom left panel shows simulated ligand concentrations from the BEC Dynamic Explicit model along the GA03 transect. Top right panel shows observed iron along the GA03 transect (Buck et al., 2015). Bottom right panel shows simulated iron from the BEC Dynamic Explicit model along the GA03 transect.

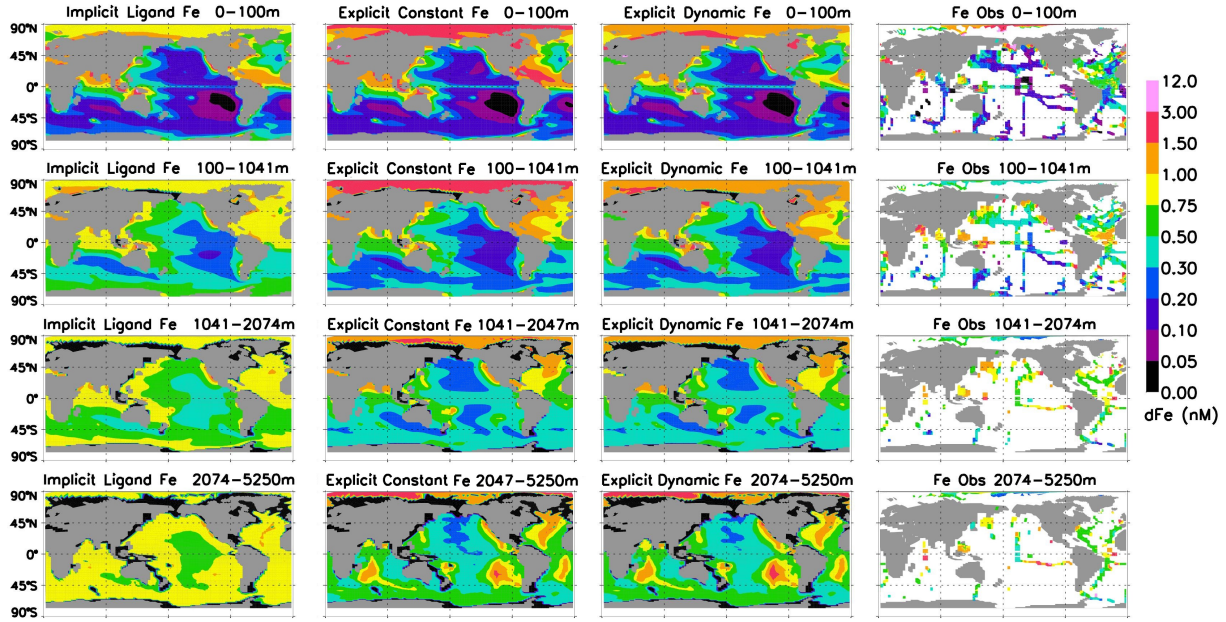

Figure 2.3: First column panels show iron from Implicit ligand model. Second column panels show iron from the Explicit Constant model. Third column panels show iron from the Explicit Dynamic model. All model data is averaged over specified the depths. Fourth column panels show iron from the Tagliabue et al. (2012) and Mawji et al. (2014) datasets.

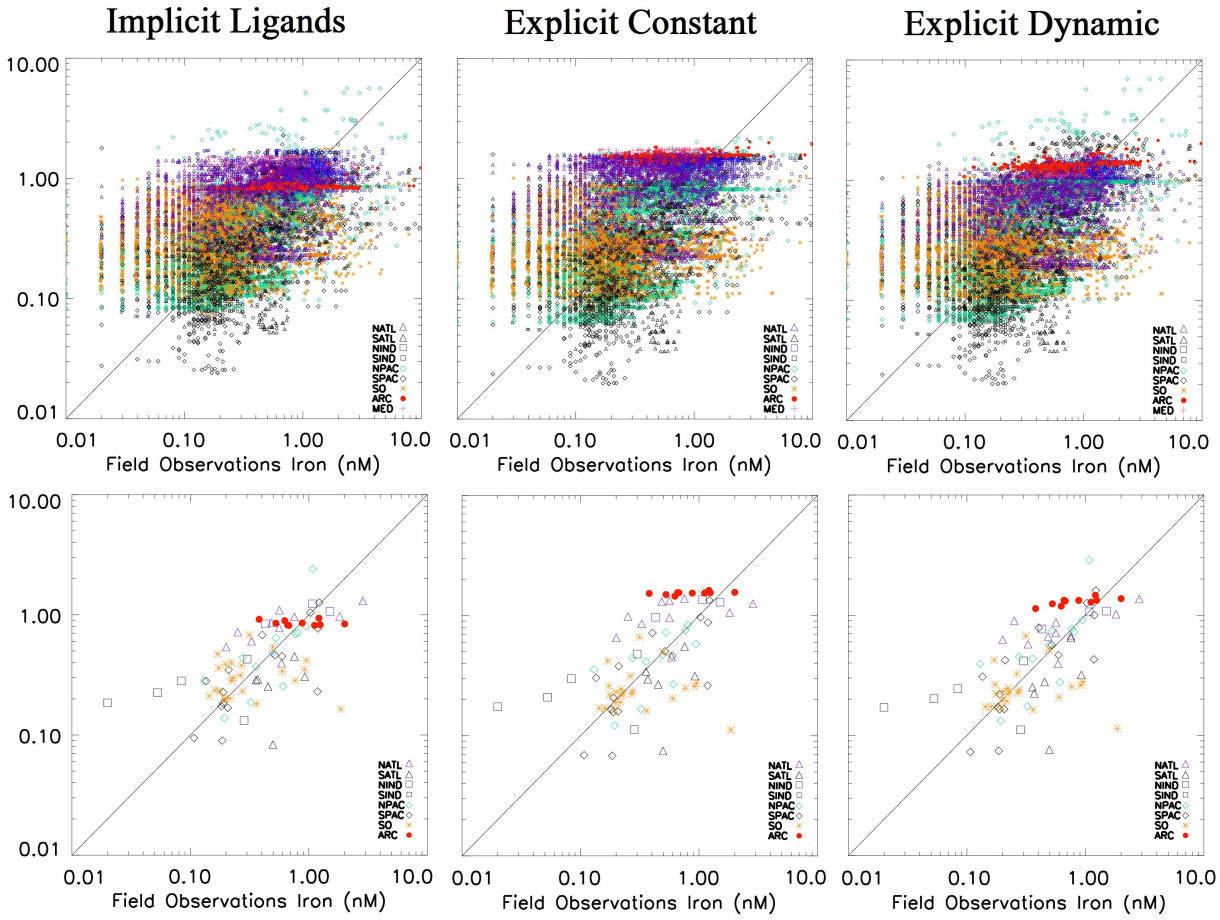

Figure 2.4: Top panels show modeled iron for the different ligand models versus observed iron from the Tagliabue et al., (2012) and Mawji et al., (2014) datasets for the upper 315m. Bottom panels show modeled iron averaged over 30x30 degree boxes for the different ligand models versus observed iron from the Tagliabue et al., (2012) and Mawji et al., (2014) datasets for the upper 315m. Statistics presented in Table 2.

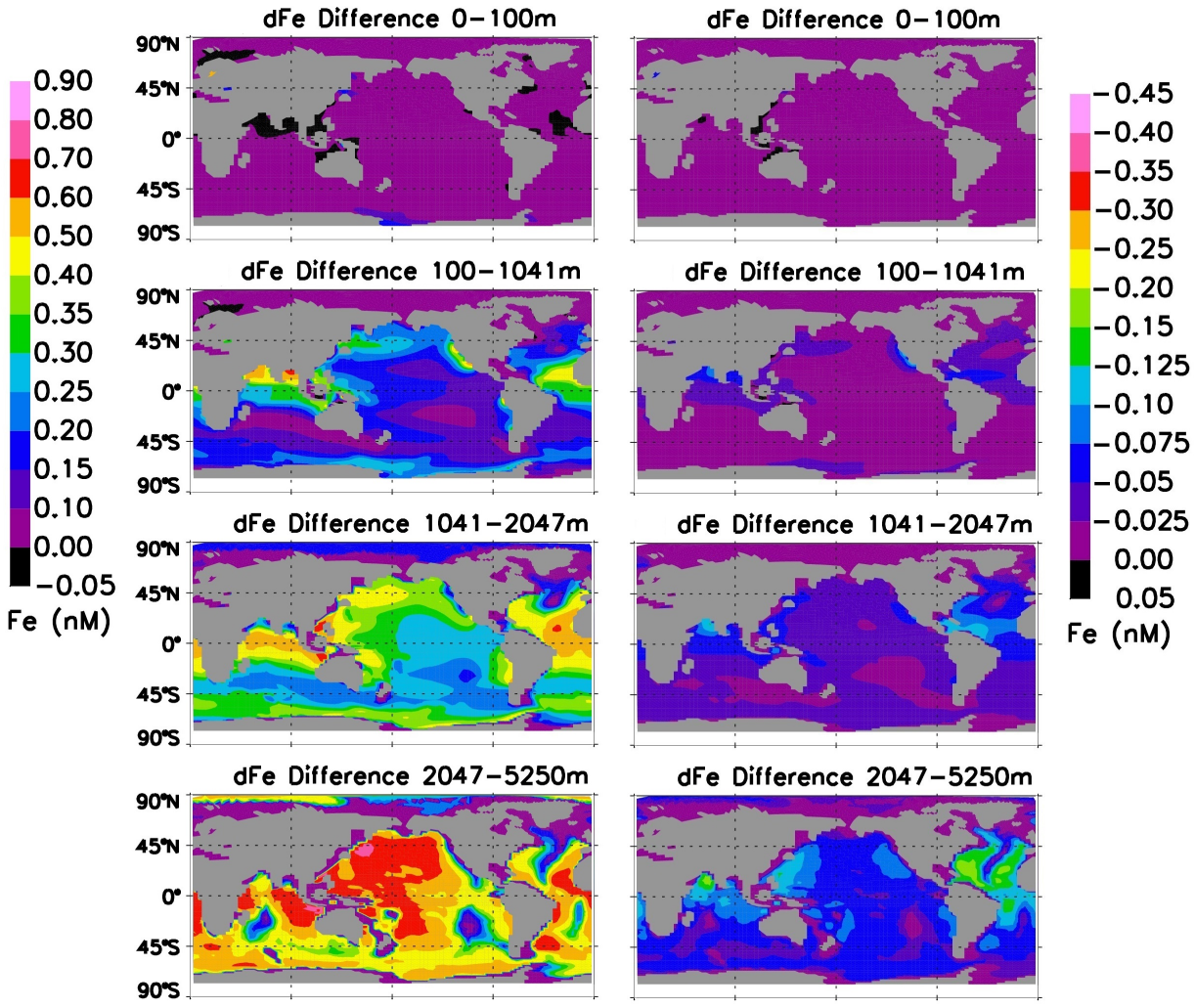

Figure 2.5: Left-hand panels show difference in iron concentration from the Explicit Dynamic increased desorption simulation averaged over the specified depths. Right-hand panels show difference in iron concentration from the Explicit Dynamic and decreased desorption simulation averaged over the specified depths.

2.8 Tables

	Literature data			GA03 L1			GA03 L2			GA03 L1+L2		
depth (m)	r	rmse	mean bias	r	rmse	mean bias	r	rmse	mean bias	r	rmse	mean bias
0-100	-0.080	3.462	-1.042	0.093	1.016	-0.895	-0.010	0.679	-0.367	-0.150	1.731	-1.544
100-500	-0.230	1.281	0.159	0.575	0.500	-0.234	0.226	0.689	0.290	0.411	1.021	-0.797
500-1000	-0.170	2.210	-0.222	0.396	0.442	-0.154	0.177	0.790	0.491	0.395	1.042	-0.811
1000-2000	-0.420	3.438	-0.659	0.363	0.442	-0.326	0.246	0.797	0.339	0.160	1.179	-1.024
2000-5250	-0.760	0.845	0.004	-0.040	0.728	-0.371	0.251	0.587	0.063	0.157	1.589	-1.157
0-5250	-0.150	2.729	-0.512	0.292	0.642	-0.367	0.119	0.697	0.155	0.174	1.337	-1.043
0-5250[a]	1.1e-7	2.613	-0.298	1.5e-6	0.498	-0.08	1.5e-13	0.768	0.469	7.1e-7	1.112	-0.075

Table 2.1: Explicit Dynamic modeled ligands compared to our compiled observational dataset (See text for details). [a] shows statistics of the constant ligand concentration of 1.52 nM compared to the observational datasets.

	Explicit Dynamic			Constant Dynamic			Implicit		
depth (m)	r	rmse	mean bias	r	rmse	mean bias	r	rmse	mean bias
0-100	0.389	0.733	-0.034	0.320	0.801	0.085	0.309	0.773	0.001
0-315a	0.375	0.748	0.011	0.319	0.798	0.092	0.325	0.763	0.014
0-315b	0.707	0.322	-0.006	0.653	0.345	0.040	0.649	0.309	-0.050
100-500	0.354	0.742	0.066	0.304	0.761	0.073	0.361	0.712	0.027
500-1000	0.250	0.583	-0.104	0.178	0.618	-0.111	0.341	0.513	-0.079
1000-2000	0.030	0.930	-0.105	0.001	0.960	-0.092	0.080	0.863	-0.027
2000-5250	0.168	1.420	-0.084	0.156	2.730	-0.210	0.181	1.404	-0.070
0-5250	0.256	1.090	-0.029	0.213	1.116	0.021	0.233	1.090	-0.017

Table 2.2: Modeled iron compared to the Tagliabue et al. (2012) dataset for the specified depth intervals at the same geographic location. 0-315a refers to modeled iron compared to observed iron at the same geographic location and depth interval. 0-315b compares averaged modeled and observed iron over 30x30 degree boxes.

Chapter 3

Controls on dissolved iron in the oceans

3.1 Abstract

We conduct sensitivity experiments with iron sources in the CESM-BEC to better understand the impact iron sources have on dissolved iron distributions and biogeochemsitry in the oceans. The sedimentary iron source had the strongest impact on dissolved iron concentrations throughout the water column. Removing the sedimentary iron source reduced iron concentrations by as much as 40% compared to the control simulation. Atmospheric iron inputs had a strong impact on surface dissolved iron concentrations and showed particular importance for subtropical gyre systems. Hydrothermal iron inputs had little impact on upper ocean iron concentrations, but did impact iron in the deep ocean mostly along mid ocean ridges. Biogeochemical processes were most sensitive to atmospheric iron inputs. The largest reductions in NPP, export production and nitrogen fixation occurred when removing the surface atmospheric iron source. This atmospheric source is the most spatially and temporally variable with strong links to climate forcings. Our results suggest that iron from hydrothermal vent systems has little impact on surface ocean biogeochemistry on a basin-wide scale, but that shallow vent systems may be of regional importance. Shallow vents in the North East Pacific in the model are shown to support a significant fraction of carbon export. These results highlight the relative importance of iron sources to dissolved

iron distributions in the CESM-BEC and associated biogeochemistry. Comparisons of similar sensitivity experiments with other global ocean biogeochemical models would help to reduce uncertainty of iron cycling processes on dissolved iron distributions in the oceans but also amongst models.

3.2 Introduction

The importance of iron as a limiting nutrient and its influence in the cycling of carbon and nitrogen is well accepted (Boyd and Ellwood, 2010). The identification of iron as a limiting nutrient in the High Nutrient Low Chlorophyll regions and potential influence on climate has spurred a great effort to measure iron and identify its cycling processes in the ocean. Johnson et al. (1997) used known iron cycling processes and sparse observations to describe global patterns of iron concentrations. They showed a nutrient like profile for iron with relatively constant deep sea concentration of $\sim$0.6 -0.7 nM and noted almost no fractionation between ocean basins. They proposed inputs from atmospheric deposition and reductions in deep sea scavenging were the cause of the observed trends. As the number of iron observations grew it became apparent that iron concentrations are more spatially variable than previously thought, and other source processes likely influence this variability. Elrod et al. (2004) measured iron fluxes on continental margins and hypothesized this as a significant source of iron to the oceans. Moore and Braucher (2008) compiled a dataset of 6,540 observations and showed higher iron concentrations near continental margins. They also conducted model sensitivity experiments and showed that inclusion of both atmospheric deposition and sedimentary diffusion of iron are necessary to simulate realistic iron distributions in the ocean. Dust inputs were observed to be spatially and temporally varying and thus not an equal source of iron to all ocean basins highlighting the importance of regional dust sources (Jickels et al., 2005; Kaufman et al., 2005; Prospero et al., 2014). Bennett et al. (2008) suggested the potential importance of hydrothermal vent sources to the deep sea iron

budget. Tagliabue et al. (2010) expanded upon this research and used a global biogeochemical model to suggest that hydrothermal sources are important for simulating Southern Ocean iron concentrations and may act to buffer iron inventories against short term atmospheric dust variability. Recycling of biogenic iron is also an important component of re-supply of iron to the ocean. Biogenic iron is recycled in surface water by zooplankton, heterotrophic bacteria and viruses and has been dubbed the ferrous wheel (Lee and Fisher, 1993; Hutchins et al., 1994; Kirchman, 1996). Studies have also noted other iron source such as icebergs (Raiswell et al. 2008; Lin et al., 2011) and rivers (Gibbs et al., 1973; Krachler et al., 2005; Rijkenberg et al., 2014).

Major removal processes for iron include biological uptake and scavenging by sinking particles. Uptake of iron by phytoplankton in surface waters can vary widely by species and in response to ambient iron concentrations (Sunda and Huntsman 1997; Twining and Baines 2013). Much of what has been learned about iron scavenging has been through studying the scavenging of Thorium isotopes. Scavenging of iron, and other trace metals, can be described as a reversible exchange of the metal and some particle between the dissolved and particulate phases (Nozaki et al., 1987; Honeyman et al., 1988). A proposed mechanism by which is this happens is Brownian-Pumping, sometimes referred to as colloidal pumping (Honeyman and Santschi 1989). A strong control on scavenging removal is particle concentration where increased particle concentration facilitates higher rates of scavenging (Honeyman et al. 1988).

Much has been learned about iron cycling in the oceans. However a great amount of uncertainty still remains for iron cycling rates and processes. The Iron Model Intercomparison Project (FeMIP) quantified this uncertainty amongst global biogeochemical ocean models and showed that rates of source inputs can vary by as much as an order of magnitude across models (Tagliabue et al., 2016). Despite the large variability in source rates, the models produced similar iron concentrations to one another and observations by tuning of the scav-

enging parameters. The large uncertainty in the source and sink parameters for iron may produce an unrealistic simulated response to different climate scenarios. Sensitivity experiments varying the rates of source and sink processes amongst the models would show their relative impacts on simulated iron concentrations and help to interpret the response to different climate forcings. In this study, we conduct sensitivity experiments with the CESM-BEC to better understand and quantify the impact iron sources have on dissolved iron inventories and distributions in the model.

3.3 Methods

3.3.1 CESM-BEC Model Description

The model used for these sensitivity experiments is Community Earth System Model - Biogeochemical Elemental Cycling model (CESM-BEC; Hurrell et al., 2013; Moore et al., 2004; 2013). The CESM is an Earth System model which includes land, ocean, atmosphere and cryosphere components with dynamic feedbacks between systems (Hurrell et al., 2013). For these simulations we use the physical ocean model (Parallel Ocean Program model; Gent et al., 2011) coupled to the ecosystem/biogeochemical module (Biogeochemical Elemental Cycling model; Moore et al., 2013) at a nominal resolution of three degrees and sixty vertical levels. The CESM-BEC tracks the dissolved nutrients, nitrate, ammonium, silicate, iron, phosphate as well as oxygen, dissolved organic carbon, dissolved organic nitrogen, dissolved organic phosphorus, dissolved inorganic carbon and alkalinity. Sinking particulate fractions of carbon, nitrogen, phosphorus, iron, calcium carbonate, biogenic silica and mineral dust are also tracked in the model. The CESM-BEC represents the following phytoplankton functional groups: diatoms, diazotrophs, small phytoplankton of the pico-nano- size class and an adaptive zooplankton group. A more detailed description of the ecosystem model can be found in Moore et al. (2004; 2013).

Dissolved iron sources include sediments, atmospheric deposition, hydrothermal vents and rivers at fluxes of 18, 11.1, 10 and 0.33 Gmol/year respectively (Figure 3.1). All iron inputs are balanced by consumption by biology or scavenging losses and eventually lost to sediments via the sinking particulate iron pool. Iron inputs from sediments are a function of particulate organic carbon flux to the bottom grid cells and based on Elrod et al. (2004), but here with a lower iron efflux rate. A full description of the sedimentary iron source can be found in Moore and Braucher (2008). Iron from dust is 3.5% by weight and the soluble fraction of iron at the surface ocean is variable. Dust climatology and variable solubility of the iron within dust as well as dFe from combustion sources are from Luo et al. (2008). The CESM also includes subsurface release of iron from sinking dust particles. The model includes two fractions of iron within dust for the subsurface dissolution source (Moore and Braucher, 2008). A small fraction of the iron (1.5%) is released in the upper water column with an e-folding length scale of 150 meters for the soft fraction. A much longer length scale is used for the remaining dust, such that about 0.1% would dissolve through a 4000m water column. Hydrothermal vent locations were compiled from the InterRidge Vents Database and from spreading ridge locations from earthchem.org (Beaulieu et al., 2013). To account for displacement of hydrothermal vent waters by buoyancy, we move the source flux up 300m from the depth of the bottom grid cell (Tagliabue et al., 2010). We apply a constant flux of iron for each grid box that has vents, and then apply a scaling factor to all vent locations so the total hydrothermal vent iron flux is equal to 10 Gmol/year. River iron inputs are simulated assuming constant iron concentration in river waters of 10 nM as they enter the ocean.

The model considers particulate and dissolved iron pools. All sources are in the dissolved pool of iron which encompasses the colloidal size fraction. Removal processes include biological uptake in the surface ocean and particle scavenging and adsorption throughout the water column. Iron that is scavenged is routed to the sinking particulate iron pool. Iron from biotic pools is routed to both the dissolved and sinking particulate iron pools via mortality (Moore

et al., 2004; Misumi et al., 2014). Remineralization and physical desorption of particulate iron occur throughout the water column. Physical desorption is released as a constant fraction of the particulate iron flux and remineralization is defined over a prescribed length scale (Moore et al., 2004). We have previously examined the sensitivity of simulated dissolved distributions to variations in the desorption rate (Sherman et al., in prep.).

The model also includes explicit simulation of ligands and iron-ligand speciation (Sherman et al., 2016 in prep.). Ligand concentrations are prognostically simulated with sources from particulate organic matter remineralization and dissolved organic matter production (Boyd et al., 2010). Ligand sinks include biological uptake, bacterial degradation, photochemical degradation and scavenging/adsorption to sinking particles. The model explicitly simulates one strong ligand class and implicitly represents weaker ligands through modification of the scavenging parameters (Sherman et al, in prep.). Stronger scavenging rates apply where iron exceeds the local ligand concentration. We assume that almost all of this free iron will actually be bound to weaker ligands that are not explicitly simulated. This represents the large background concentration of weaker ligands and the increased scavenging rates represent the weaker affinity they have for iron, but scavenging rates are still lower than they would be for truly free iron ions. This allows the simulated dissolved iron to exceed the concentration of our simulated strong binding ligands in areas with high iron inputs to the oceans, and improves the match to observed distributions (Sherman et al., in prep.).

3.3.2 Fe sensitivity experiments

The goal of these experiments is to better understand how iron source processes influence dissolved iron distributions in the ocean. The CESM-BEC has four primary iron sources: sediments, atmospheric deposition, hydrothermal vents and river inputs. In each experiment one of the sources was turned off while the others remained active. All other iron cycling and biogeochemical parameters remained the same throughout the experiments. Atmospheric

iron deposition is a two component iron source. 1) instantaneously soluble iron fraction for the surface ocean and 2) a fraction of iron that dissolves at depth. Experiments are run where each component of the atmospheric iron source is turned off while the other remains active.

3.4 Results

3.4.1 Control simulation

The control run is able to simulate realistic iron concentrations and distributions compared to observations from the Tagliabue et al (2012) and GEOTRACES (Mawji et al., 2014) datasets. Table 3.1 shows statistics comparing averaged simulated and observed iron over 10°x10° boxes over the specified depth intervals. The highest correlations to observations are in the upper 1000m with low root mean squared error throughout the water column. Simulated iron in the surface ocean closely matches observations. The model is able to capture high iron in areas of high dust deposition, along continental margins and upwelling regions (Figure 3.2). The model also simulates low iron concentrations in the center of ocean basins and in the HNLC regions. At intermediate depths the model is able to capture the trend of high iron near land masses with decreasing concentrations moving towards the center of ocean basins. Modest overestimations occur in the North and tropical Atlantic and Arctic Ocean, with underestimations in the North Pacific. Its difficult to ascribe error to specific sources or removal processes as there is a large amount of uncertainty in the flux rates for iron source and sink processes (Tagliabue et al., 2016). Increasing a source or decreasing a removal process may improve one region at the cost of another. Further observational constraints are needed on the source and removal rates for iron to better constrain model parameters.

3.4.2 Sedimentary iron source sensitivity experiment

Removing sedimentary iron inputs produced large decreases in iron concentrations along continental margins and modest decreases near bottom ocean sediments compared to the control run (Figure 3.3). Decreases between 0.2 and 0.4 nM are seen in the western boundary currents in the upper ocean above 1000m (Figure 3.3). Sedimentary iron also had a large impact on dissolved iron concentrations deep in the water column. At depths below 2000m iron concentrations decreased by 33% compared to the control simulation (Table 3.2). A greater than 70% decrease in iron concentrations occurred in the Arctic for the upper 1000m compared to the control simulation, the largest decline of any basin. The Arctic Ocean is unique in that it is relatively shallow with a large continental shelf. The relatively shallow water column, large shelf and minimal dust inputs make the Arctic Ocean iron concentrations very sensitive to the sedimentary iron source. Regions with significant dust inputs, like the North Atlantic, were more resilient to changes in sedimentary iron inputs, although still showed decreases between 23% and 27% compared to the control simulation. Some very minor increases in iron are seen along land masses or regions where iron inputs from either dust or hydrothermal inputs are high. In the surface this is due to decreases in biological production, which decreased the sinking flux and alleviated scavenging losses. The increases near vent systems are likely due to decreases in scavenging from decreasing the sinking mass flux due to the surface productivity decline.

The biogeochemical impacts of removing the sedimentary iron sources are quantified in Table 3.3. Decreases of 3% for net primary production (NPP), 8% for export production and 31% for nitrogen fixation occurred compared to the control simulation. Regions of iron limitation increased by 59%, 36% and 51% for the diatoms, diazotrophs and small phytoplankton respectively compared to the control simulation.

3.4.3 Atmospheric iron deposition source sensitivity experiment

In the upper 100m iron concentrations decreased similar to the pattern of dust deposition when removing the surface atmospheric iron source (Figure 3.4). The largest decreases in surface waters of 0.3 to 0.6 nM occurred in the Indian and Pacific basins and in regions where dust deposition is high like the mid-Atlantic. Below 100m decreases in iron still resembles fields of dust deposition. Increases in iron concentrations are also seen below 100m. Increases in iron concentrations are generally below 0.1 nM which increase to ∼0.3 nM below 2000m. The increase in subsurface iron is due to reductions in the sinking mass flux from severe iron limitation of the biology in surface waters. The sinking mass flux decreased by 9.31% at 100m, 21.39% at 1000m and 21.18% at 2000m compared to the control run. Comparatively, removing the sedimentary input decreased the sinking mass flux by 7.56% at 100m, 14.97% at 1000m and 11.76% at 2000m. Removing the subsurface atmospheric iron source decreased iron concentrations under regions of dust deposition throughout the water column but had less impact in surface iron concentrations in the gyres than the surface atmospheric iron source. Decreases of iron in the gyres was generally less than 0.1 nM. Larger decreases between 0.4 nM and 1 nM were seen in the mid Atlantic and Arabian Sea where dust deposition is high. Increases in iron concentration generally less than 0.1 nM are seen deeper in the water column of the Southern Ocean.

The atmospheric surface iron source had the largest impact on biology and biogeochemistry in the CESM. NPP decreased by 7.21%, export production by 8.77%, nitrogen fixation by 39.05% compared to the control run. Regions of iron limitation for diatoms increased by 76%, diazotrophs to 46% and small phytoplankton to 57% compared to the control simulation. The atmospheric subsurface iron source had less of an impact on biogeochemistry than atmospheric surface iron. NPP decreased by 1%, export production decreased by 2% and nitrogen fixation decreased by 4%. Regions of iron limitation increased by 9% for diatoms and diazotrophs, and by 8% for small phytoplankton compared to the control simulation.

3.4.4 Hydrothermal vent iron source sensitivity experiment

Removing the hydrothermal iron source had minimal effect on iron concentrations in the upper 1000m (Figure 3.5, Table 3.2). More significant reductions in iron occurred below 1000m, specifically along ocean ridges. Iron concentrations decreased by 22% between 1-2 km and by 35% below 2 km across all basins. The largest decreases in iron concentrations occurred in the deep Atlantic, South Pacific and Southern Ocean basins where mid ocean ridges are pervasive. Overall hydrothermal vents had little influence on biology and other biogeochemical processes. There was less than a one percent change in primary production, export production and nitrogen fixation.

Tagliabue et al. (2010) conducted similar sensitivity experiments with the PICES model varying the strength of their hydrothermal vent source. The BEC hydrothermal source is 10 Gmol/year and we compare to the results of Tagliabue et al. (2010) that used a hydrothermal source of 9 Gmol/year. Our results generally support the findings of Tagliabue et al. (2010). The BEC showed a better match to observed iron for the deep ocean when including hydrothermal vent inputs, similar decreases in mean iron concentrations to Tagliabue et al. (2010) for the upper and deep ocean and decreases in carbon export for the Southern Ocean (Tagliabue et al., 2010). Tagliabue et al. (2010) found inclusion of a hydrothermal vent source increased iron by 0.07 nM for the upper 2000m and we also found an increase of 0.07 nM. The authors found an increase in iron of 0.312 nM below 2000m and we found an increase of 0.22 nM. A stronger influence on iron concentrations in the southern hemisphere was also observed in the CESM. However, we do not find as strong of an impact on Southern Ocean carbon export as Tagliabue et al. (2010). The authors found increases of carbon export at 100m of 5% globally and 15% in the Southern Ocean due to the hydrothermal vent source. The BEC produced increases of 0.67% globally and 3.42% in the Southern Ocean. Figure 3.6 shows export production for the control simulation, no hydrothermal iron simulation and the percent change between simulations. Our results show that there was a

larger percent decrease in export production for the NW North Pacific. Iron from shallow hydrothermal vents in the North West Pacific is advected by the Kuroshio Current fueling production in the North Pacific. This highlights the importance of shallow vent systems may have on primary production.

3.4.5 River iron source sensitivity experiment

The iron river source had a very minor impact on iron concentrations. Iron decreased by 1.5% in the upper 100m and less than 1% below 100m across all basins compared to the control simulation. The largest decrease for a basin occurred in the upper 100m of the Arctic with a decrease in iron concentration of 3%. More significant decreases of between 0.1 and 0.3 nM occurred at river mouths (Figure 3.7). NPP and export production did not change compared to the control simulation. Nitrogen fixation decreased by 2% and iron limitation for phytoplankton groups increased no more than 2.4% compared to the control simulation.

Mean dissolved iron profiles from the simulations are shown in Figure 3.8. Removing the sedimentary iron source leads to sharp declines throughout the water column. Removing the atmospheric source lowers surface concentrations sharply relative to our control. Turning off the hydrothermal vent source results in large declines at mid-depths, but has relatively little impact on surface waters.

3.5 Discussion

3.5.1 Sediment iron impacts on biogeochemistry

The conducted sensitivity experiments show the relative impacts of iron source processes on iron distributions and biogeochemistry in the CESM . The sedimentary iron source gen-

erally had the strongest control on iron concentrations through the water column, except where dust inputs were large. Removing the sedimentary source highlighted the strong sensitivity of Arctic Ocean iron to the sediments, along continental margins and in deep ocean water close to sediments. In the upper ocean iron concentrations decreased the most near continental margins. Lesser change was seen in the gyres. Removing the sedimentary iron source decreased total phytoplankton biomass by 7.73% from the control run and shifted the community towards small phytoplankton (Table 3.4). This shift in the phytoplankton community composition mitigated the reduction in NPP because small phytoplankton are able to grow at faster rates than larger phytoplankton and exported less efficiently than diatoms (Moore et al., 2004). For the small decrease in NPP there was a comparatively large decrease in export production (8%). There was a 26% reduction in diatom biomass from the control run. Diatoms do well in high nutrient environments, such as coastal and upwelling regions where the sedimentary iron source is strong. Any changes to the iron flux in these regions will likely influence phytoplankton communities and resulting biogeochemical cycles. Although diazotroph biomass changed very little, there was a large decrease in nitrogen fixation (31%, Table 3.3). The largest decreases in nitrogen fixation occurred mostly in the subtropical gyres of the Pacific. The lateral advection of iron from the continental shelves in the Pacific is a important process for new iron to enter the subtropical gyres in the model (see also Moore and Braucher, 2008). Removing the supply of iron inhibited diazotrophs from fixing nitrogen in these regions the most. High atmospheric iron puts in the Atlantic and Indian oceans helped mitigate the reduction in nitrogen fixation in these basins.

3.5.2 Atmospheric iron deposition impacts on biogeochemistry

In the surface ocean, removing the surface atmospheric iron source caused iron concentrations to decrease sharply in regions near dust sources but appreciable decreases also occurred within subtropical gyres. Surface deposition is an important iron source in the CESM for

the gyre systems. Although advection of sedimentary iron is also important, it needs to be advected far from continental margins to reach the gyres. The residence time of iron in the upper 100m in the CESM is 0.89 years. Residence times increase with depth and biological uptake rapidly removes iron in the upper 100m. Much of the lateral transport from continental margins takes place below the euphotic zone. Letscher et al. (2016) recently showed that lateral transport supplies approximately 50% of the macronutrient inputs that support gyre productivity. Lateral fluxes of dFe appear to be equally important. Below the surface layer iron decreases in regions of high dust input, but generally increases elsewhere. The increase in iron concentration in the subsurface is driven by the reduction in the sinking mass flux, which reduces scavenging losses of iron. The largest decreases in export production, nitrogen fixation and primary production occurred when removing the surface atmospheric iron source. These large biogeochemical changes are due to the strong and widespread influence atmospheric iron inputs have on surface iron concentrations. Removing this source created widespread iron nutrient limitation. Compared to removing the sedimentary iron source, the relative change in NPP and export production were similar. This is because the proportion small phytoplankton to diatoms (Table 3.4) is essentially the same compared to the control simulation. Removing the surface atmospheric iron source did not change iron distributions enough to significantly shift phytoplankton community composition.

Removing subsurface atmospheric iron decreased iron concentrations throughout the water column, with increases less than 0.2 nM in the Southern Ocean. Iron limitation across phytoplankton groups increased by $\sim$9% compared to the control run, but generally had little impact on surface ocean biogeochemistry. Inclusion of a subsurface atmospheric iron source in biogeochemical models may be an important additional component of the overall atmospheric iron source. Inclusion of this source improves the match to observations in high dust flux regions.

3.5.3 Hydrothermal iron impacts on biogeochemistry

Simulated iron concentrations were only sensitive to hydrothermal vent inputs in the subsurface ocean, with the southern hemisphere iron being more sensitive than northern hemisphere iron. The largest changes in iron concentration from the control simulation occurred near spreading ridges where the majority of hydrothermal vents in the CESM exist. Inclusion of hydrothermal vent sources produced a better match between observed and simulated iron in the deep ocean. GEOTRACES data from the Atlantic and Pacific show dissolved iron in the deep oceans are greatly impacted by hydrothermal vents (Rijkenberg et al., 2015; Resing et al., 2015; Conway and John, 2015; Buck et al., 2015). Inclusion of hydrothermal iron sources in biogeochemical models is necessary to reproduce realistic dissolved iron distributions for the deep ocean (Tagliabue et al., 2016). Omission of this source could lead biogeochemical models to bias their sedimentary sources high to compensate. Our results showed hydrothermal iron inputs had little effect on surface ocean biogeochemistry and do not support the hypothesis that hydrothermal iron has any significant impact on carbon uptake into the oceans for the contemporary period. Although the total change in export production between the sensitivity and control simulation was small (0.05 GtC/year, Table 3.2), the percent change in some regions of the Southern Ocean and North Pacific were larger (Figure 3.6). The NW North Pacific showed a percent change greater than 25%. This large change in export production is driven by shallow coastal hydrothermal vents in the NW Pacific. Iron from these vents are advected by the Kuroshio Current into the iron limited waters of the North Pacific. This highlights the importance of shallow hydrothermal vents on ocean productivity. The distribution and flux of iron from hydrothermal vents is highly unconstrained and further research is needed to fully understand their impacts on carbon cycling and climate. We release only dissolved iron from the hydrothermal vents in our simulations. Resing et al. (2015) showed how including a vent source for ligands could dramatically alter the lifetimes and resulting iron distributions, leading to larger biogeochemical

impacts. Ligand release from vent sites will be a future subject of research with the CESM.

3.6 Conclusions

The model results show the sensitivity of iron concentrations and biogeochemical processes to major iron sources in the CESM. Sedimentary and atmospheric iron inputs had the largest impact on iron concentrations and biogeochemistry. Sedimentary iron inputs are significant along continental margins and upwelling regions where nutrients are generally high. Removing iron inputs in these areas caused a large shift in phytoplankton community composition from diatoms to small phytoplankton. This shift in the phytoplankton community caused less change in NPP but a relatively large change in export production. Iron concentrations were sensitive to atmospheric iron inputs near dust sources and within the subtropical gyre in the surface ocean. NPP, export production and nitrogen fixation are most sensitive to iron inputs from the atmosphere in the CESM. Iron concentrations were most sensitive to hydrothermal vent iron inputs in the deep ocean, specifically along spreading ridges. The insensitivity of surface iron concentrations to hydrothermal vent iron caused little change in biogeochemistry on a global scale. However, shallow vents may have significant regional influence. More observations of hydrothermal vent inputs and locations will help elucidate their influence on iron concentrations and biogeochemistry. River sources had small impacts on iron concentrations and biogeochemistry, with mainly local impacts near large river mouths.

Our results show the sensitivity of iron concentrations to iron sources for one model. To better understand the impacts of iron sources on iron concentrations and biogeochemistry, additional experiments should be conducted with other global biogeochemical models and compared. The FeMIP project noted a large uncertainty in iron source rates (Tagliabue et al., 2016). Further constraints on iron source or sink rates would greatly aid modeling efforts

and help close the marine iron budget.

3.7 Figures

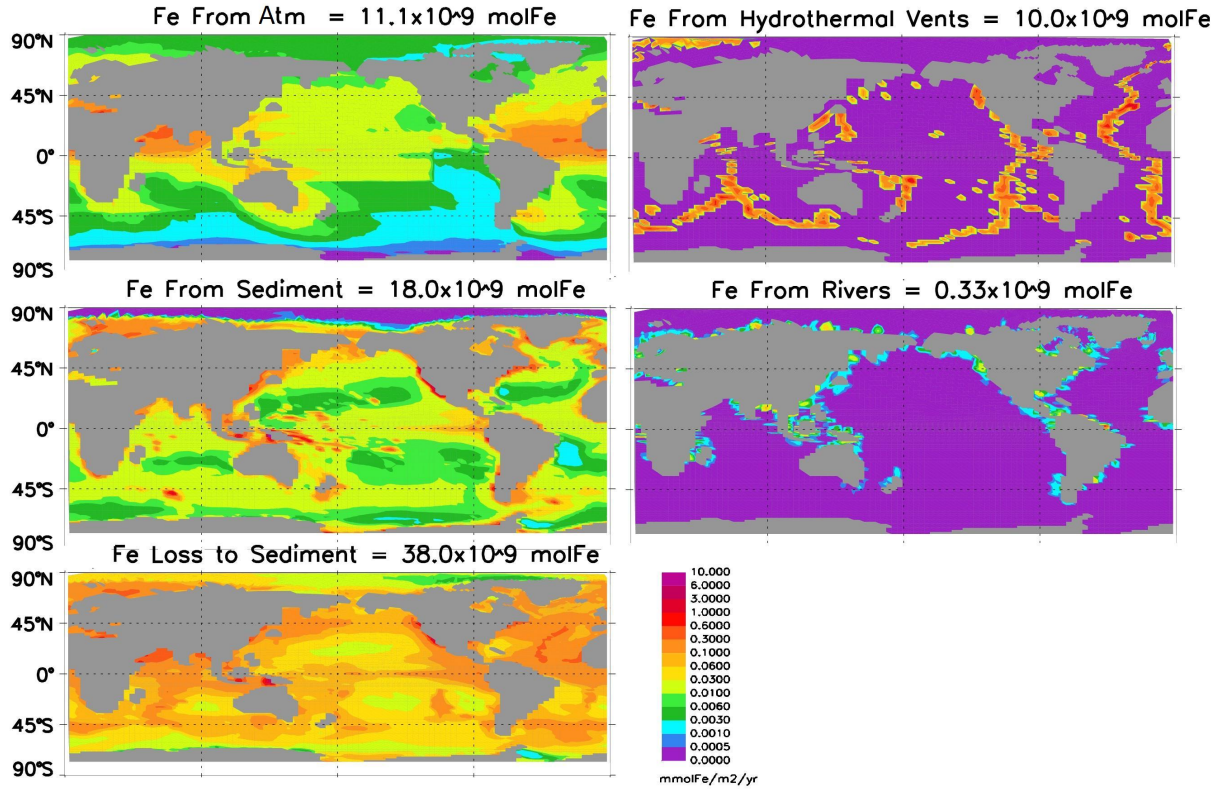

Figure 3.1: Iron source and sink fluxes (mol Fe/year) for the CESM-BEC.

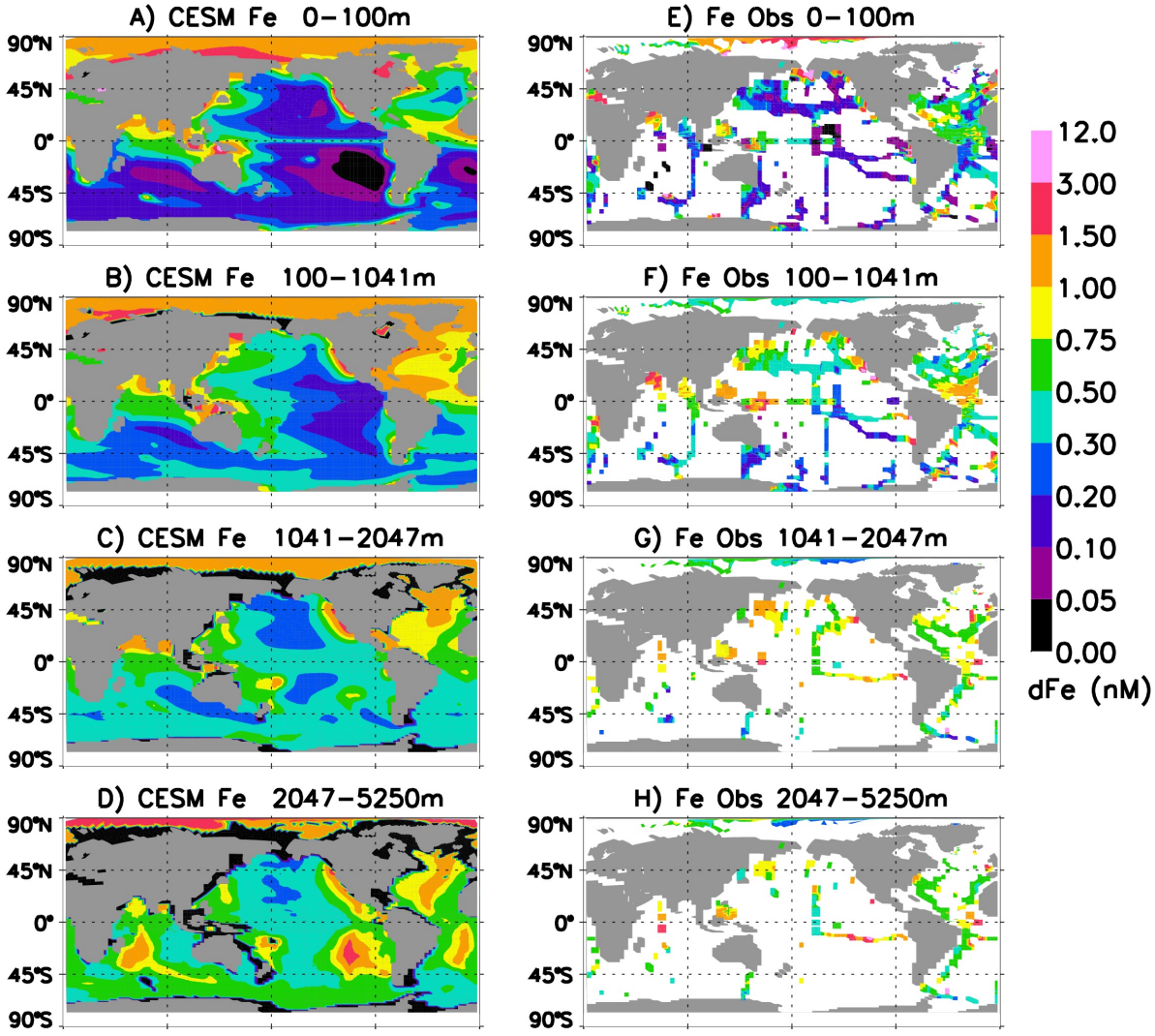

Figure 3.2: Panels A-D show CESM-BEC simulated iron averaged over the specified depth intervals. Panels E-H show observed iron for the specified depth intervals.

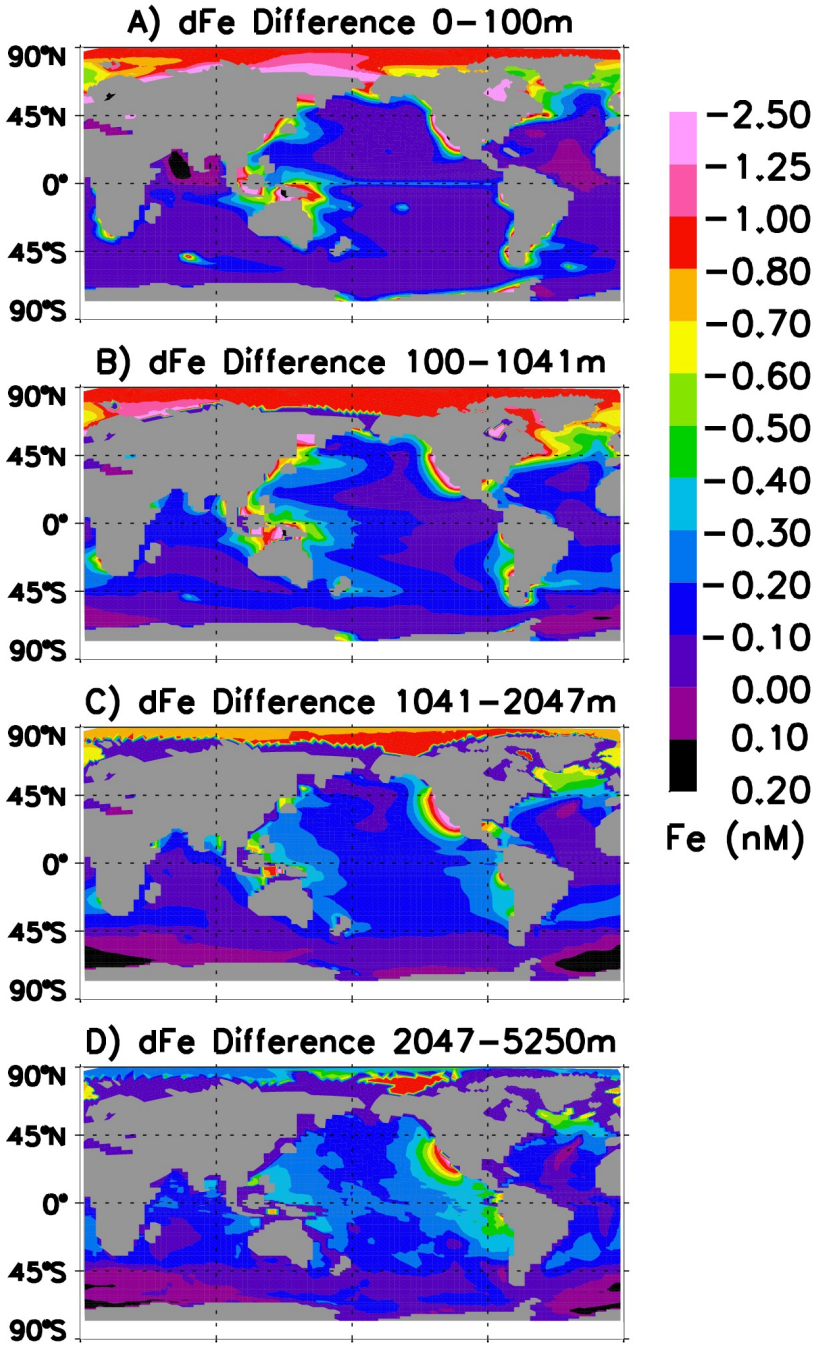

Figure 3.3: Difference in iron concentration between the control simulation and simulation with no sedimentary iron, averaged over specified depth intervals.

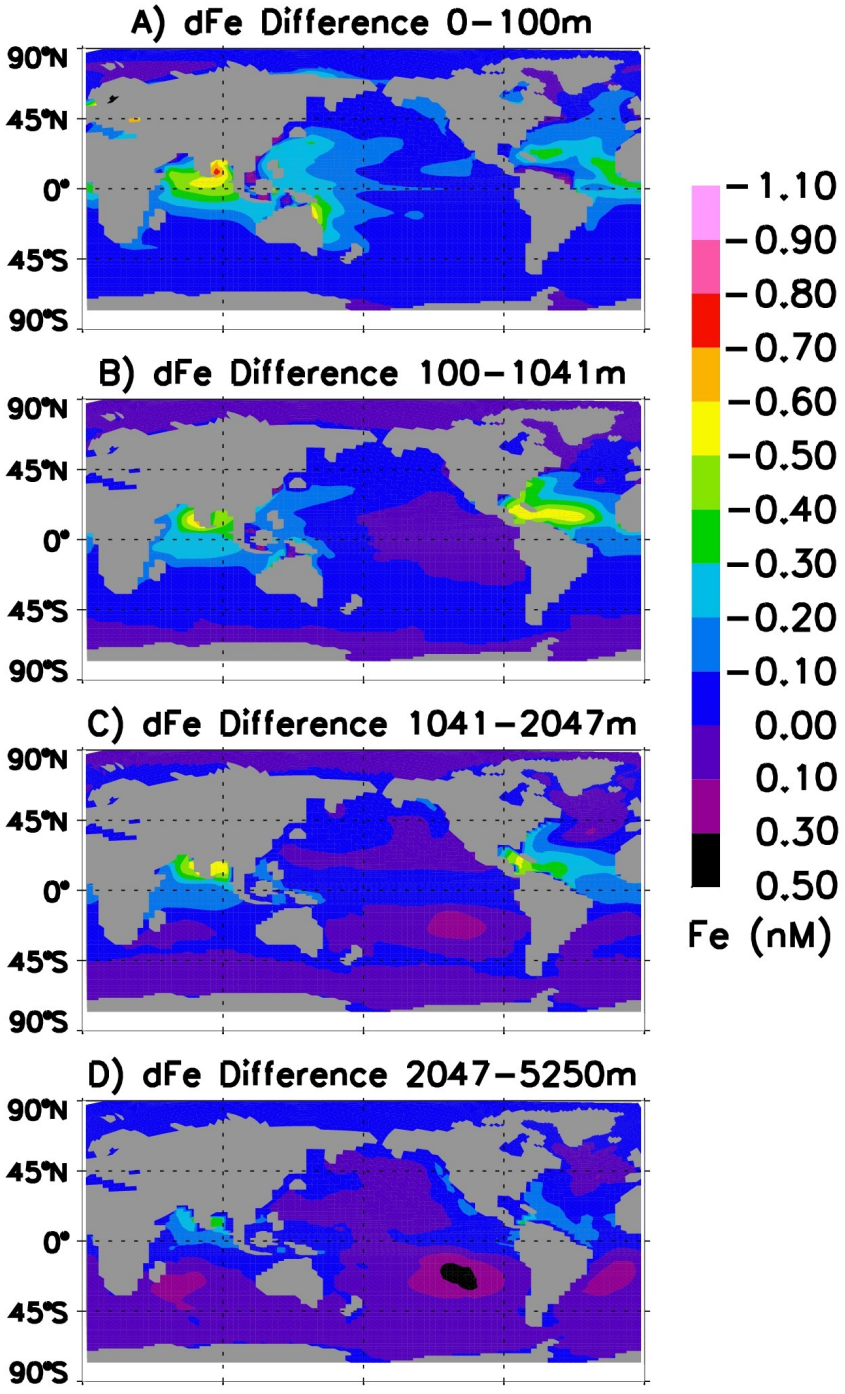

Figure 3.4: Difference in iron concentration between the control simulation and simulation with no surface atmospheric iron, averaged over specified depth intervals.

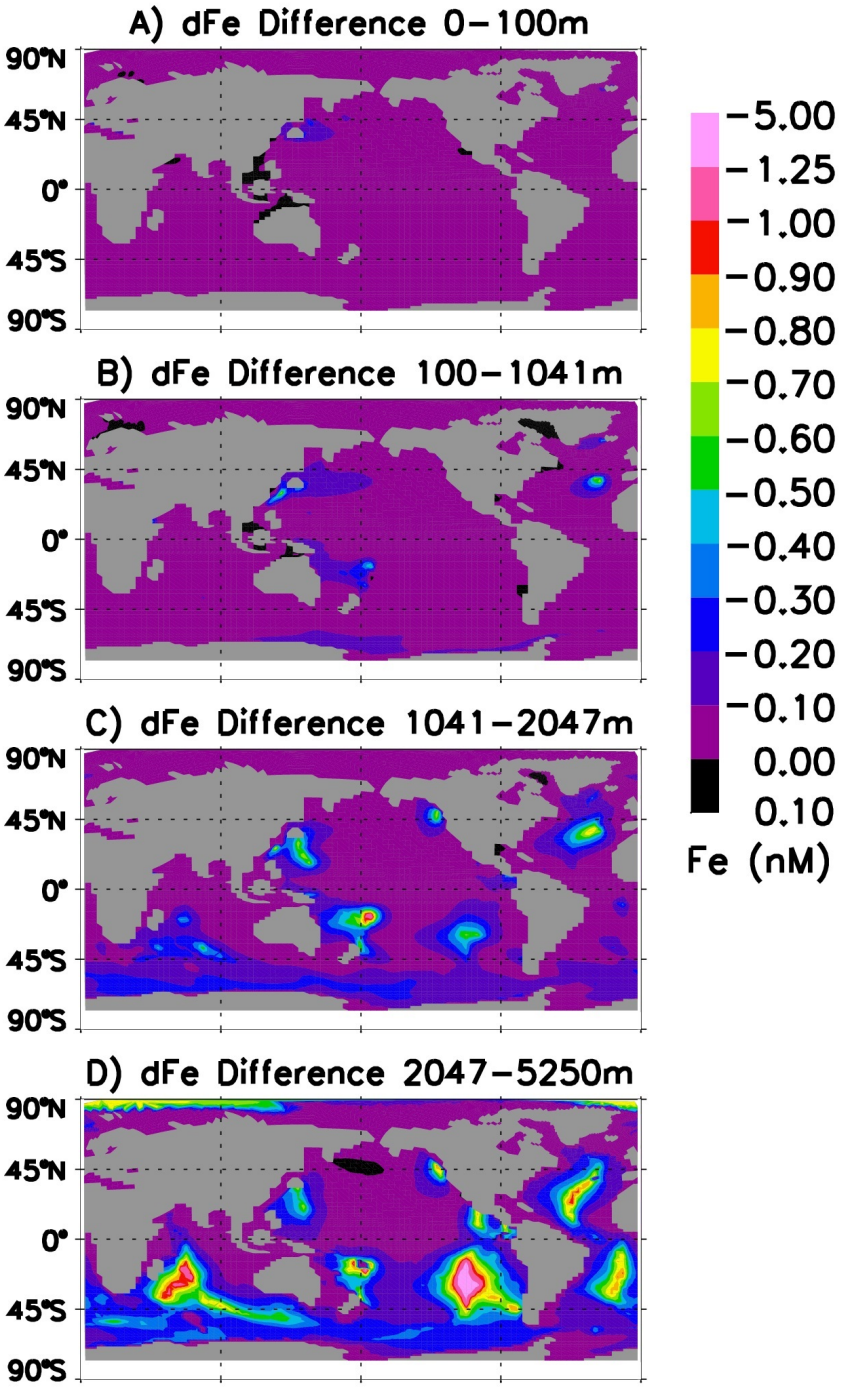

Figure 3.5: Difference in iron concentration between the control simulation and simulation with no hydrothermal vent iron, averaged over specified depth intervals.

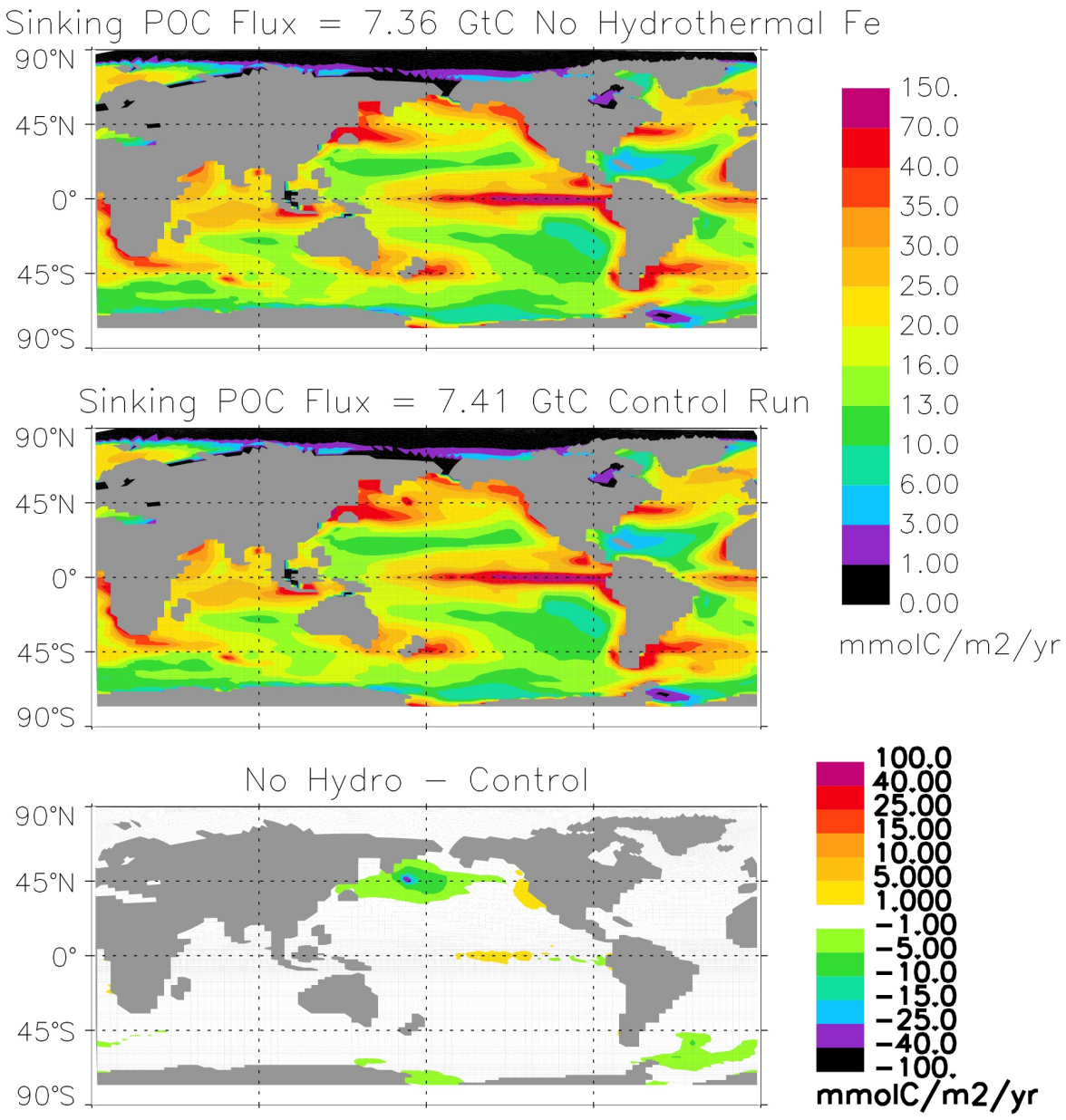

Figure 3.6: Top panel shows sinking POC flux at 100m for the simulation with no hydrothermal vent iron inputs. Middle panel shows sinking POC flux at 100m for the control simulation. Bottom panel shows the percent difference in POC flux at 100m between simulations.

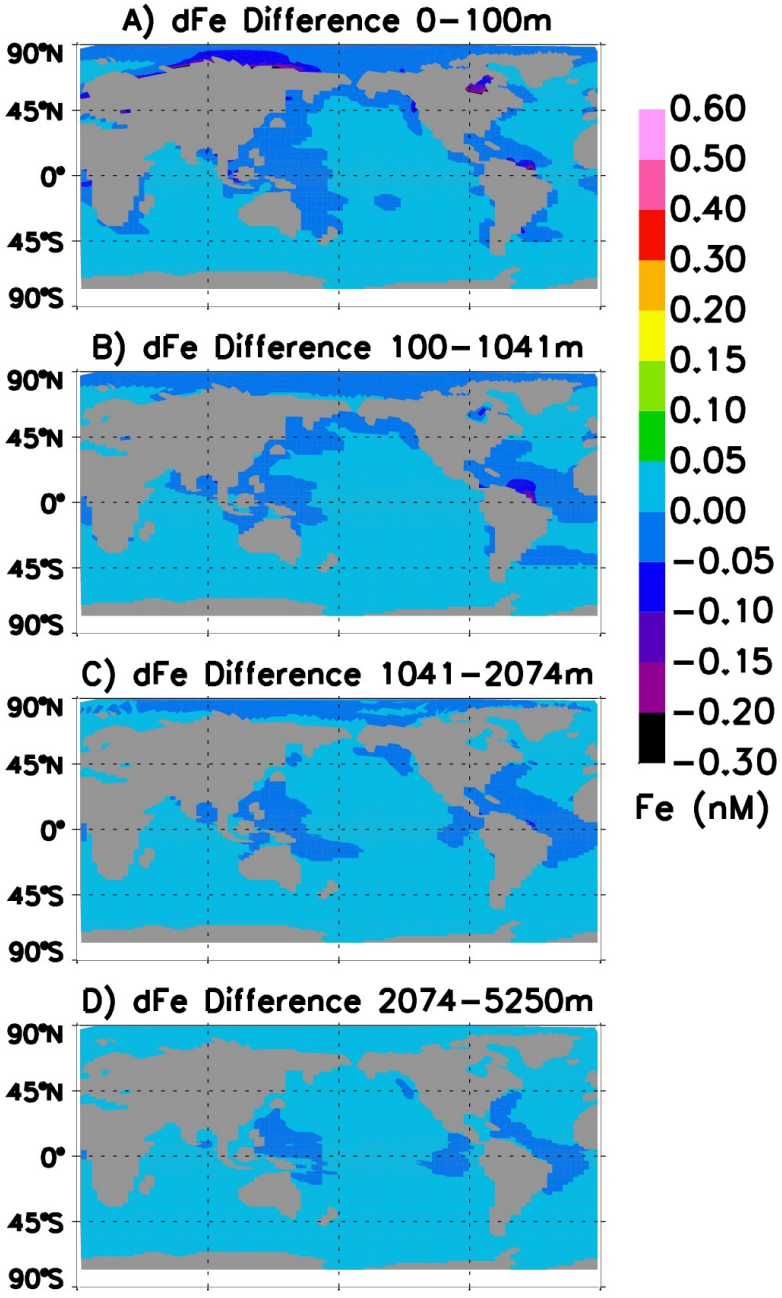

Figure 3.7: Difference in iron concentration between the control simulation and simulation with river iron, averaged over specified depth intervals.

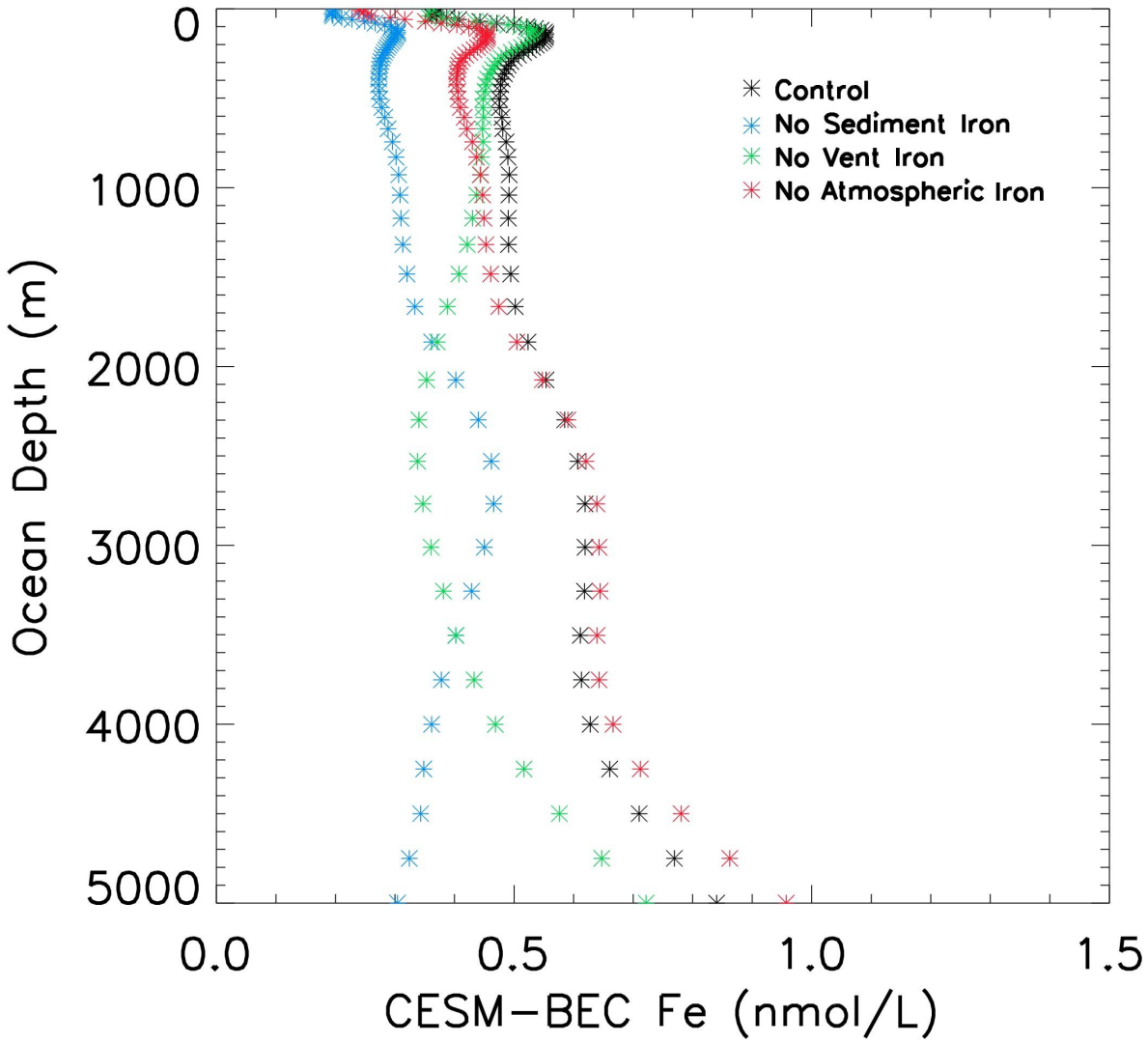

Figure 3.8: Iron averaged at each model depth for the iron source sensitivity and control experiments.

3.8 Tables

	r	rmse	r avg	rmse avg
0-100m	0.389	0.733	0.615	0.407
100-1000m	0.333	0.706	0.625	0.292
1000-2000m	0.03	0.93	0.181	0.321
2000-5000m	0.168	1.42	0.231	0.315

Table 3.1: Statistics for comparing simulated iron from the control and observed iron at the same geographic location and depth (r and rsme) and averaged over 10x10 degree boxes (r avg and rmse avg).

	Control	Sediment	Vents	Surface Atm	Subsurface Atm
All Basins					
0-100m	0.41	0.23 (-45)	0.41 (-2)	0.31 (-25)	0.37 (-10)
100-1000m	0.49	0.29 (-41)	0.46 (-7)	0.43 (-14)	0.42 (-16)
1000-2000m	0.51	0.34 (-33)	0.4 (-22)	0.48 (-6)	0.44 (-13)
2000-5000m	0.62	0.41 (-33)	0.4 (-35)	0.64 (4)	0.58 (-6)
N. Atlantic					
0-100m	0.68	0.51 (-26)	0.68 (0)	0.55 (-21)	0.58 (-15)
100-1000m	1.03	0.75 (-27)	0.98 (-4)	0.82 (-20)	0.73 (-29)
1000-2000m	0.89	0.68 (-23)	0.76 (-14)	0.76 (-15)	0.65 (-26)
2000-5000m	0.83	0.66 (-27)	0.58 (-30)	0.77 (-8)	0.67 (-13)
S. Atlantic					
0-100m	0.28	0.19 (-33)	0.28 (0)	0.19 (-33)	0.21 (-24)
100-1000m	0.46	0.27 (-41)	0.46 (0)	0.41 (-12)	0.33 (-29)
1000-2000m	0.48	0.32 (-32)	0.42 (-11)	0.45 (-6)	0.34 (-30)
2000-5000m	0.72	0.52 (-27)	0.43 (-40)	0.77 (7)	0.62 (-13)
N. Indian					
0-100m	0.93	0.95 (3)	0.93 (0)	0.54 (-41)	0.83 (-10)
100-1000m	0.87	0.65 (-25)	0.86 (-1)	0.54(-38)	0.61 (-30)
1000-2000m	0.92	0.74 (-20)	0.92 (-1)	0.62 (-32)	0.61 (-33)
2000-5000m	0.75	0.53 (-30)	0.69 (-9)	0.59 (-22)	0.55 (-28)
S. Indian					
0-100m	0.31	0.2 (-37)	0.31 (0)	0.17 (-46)	0.28 (-10)
100-1000m	0.40	0.25 (-37)	0.39 (-2)	0.28 (-31)	0.33 (-16)
1000-2000m	0.42	0.3 (-27)	0.33 (-22)	0.37 (-11)	0.36 (-15)
2000-5000m	0.67	0.49 (-26)	0.4 (-41)	0.69 (3)	0.62 (-6)
N. Pacific					
0-100m	0.36	0.15 (-57)	0.34 (-5)	0.24 (-32)	0.34 (-6)
100-1000m	0.44	0.2 (-55)	0.39 (-11)	0.4 (-8)	0.41 (-8)
1000-2000m	0.44	0.2 (-55)	0.35(-21)	0.43 (-4)	0.41 (-7)
2000-5000m	0.48	0.2 (-59)	0.37 (-22)	0.5 (4)	0.45 (-7)
S. Pacific					
0-100m	0.28	0.09 (-68)	0.28 (-1)	0.19 (-31)	0.26 (-5)
100-1000m	0.36	0.15 (-58)	0.33 (-9)	0.34 (-5)	0.34 (-6)
1000-2000m	0.46	0.25 (-46)	0.3 (-35)	0.48 (4)	0.44 (-4)
2000-5000m	0.64	0.37 (-41)	0.35 (-44)	0.71 (12)	0.62 (-2)
Southern Ocean					
0-100m	0.20	0.09 (-54)	0.19 (-4)	0.19 (-7)	0.18 (-11)
100-1000m	0.30	0.2 (-32)	0.26 (-15)	0.3 (-2)	0.29 (-5)
1000-2000m	0.37	0.34 7)	0.23 (-38)	0.39 (5)	0.39 (4)
2000-5000m	0.57	0.5 (-12)	0.32 (-43)	0.61 (-7)	0.62 (9)
Arctic					
0-100m	1.35	0.36 (-74)	1.35 (0)	1.31 (-3)	1.35 (0)
100-1000m	1.26	0.35 (-72)	1.27 (0)	1.3 (3)	1.28 (1)
1000-2000m	1.29	0.46 (-64)	1.28 (0)	1.31 (1)	1.29 (0)
2000-5000m	1.67	1.16 (-30)	1.33 (-20)	1.66 (-1)	1.66 (0)

Table 3.2: Average iron concentrations for model simulations for varying depths and ocean basins. Percent difference from control simulation is in parenthesis.

	Control	No Sediment	No Vents	No Surface Atm	No Subsurface Atm
NPP (PgC/year)	49.9	48.4 (-3.01)	49.7 (-0.40)	46.3 (-7.21)	49.4 (-1.00)
Exp P (PgC/year)	7.41	6.82 (-7.96)	7.36 (-0.67)	6.76 (-8.77)	7.26 (-2.02)
N Fix (TgN/year)	195.9	134.8 (-31.19)	194.6 (-0.66)	119.4 (-39.05)	188.1 (-3.98)
Dait % Fe limited	40.69	64.69 (58.98)	41.09 (0.98)	71.58 (75.92)	44.27 (8.80)
Diaz % Fe limited	37.72	51.25 (35.87)	38.17 (1.19)	55.03 (45.89)	41.2 (9.23)
Sp % Fe limited	50.69	76.42 (50.76)	51.66 (1.91)	79.51 (56.86)	54.77 (8.05)

Table 3.3: [a] is net primary production. [b] is export production. [c] is nitrogen fixation. [d] is the percent of ocean area where iron is the limiting nutrient. Parenthesis show percent change relative to the control simulation.

	Control	No Sediment	No Atm
% biomass sp[a]	0.50	0.59	0.51
% biomass diat[b]	0.47	0.38	0.46
% biomass diaz[c]	0.03	0.03	0.03
% change sp from ctrl[d]		8.54	-1.78
% change diat from ctrl[e]		-25.52	-6.01
% change diaz from ctrl[f]		-1.61	-2.36
% change total from ctrl[g]		-7.73	-3.78

Table 3.4: [a] The percent of total phytoplankton biomass that are small phytplankton. [b] The percent of total phytoplankton biomass that are diatoms. [c] The percent of total biomass that are diazotrophs. [d] The percent change in small phytoplankton biomass from the control simulation. [e] The percent change in diatom biomass from the control simulation. [f] The percent change in diazotroph biomass from the control simulation. [g] The percent change in total phytoplankton biomass from the control simulation.

Chapter 4

Temperature influece on phytoplankton community growth rates

As appears in:

Sherman, E., Moore, J. K., Primeau, F., Tanouye, D. "Temperature influence on phytoplankton community growth rates," ***Global Biogeochemical Cycles*****, 2016**

4.1 Abstract

A large database of field estimates of phytoplankton community growth rates in natural populations was compiled and analyzed to determine the apparent temperature effect on phytoplankton community growth rate. We conducted an ordinary least squares regression to optimize the parameters in two commonly used growth-temperature relations (Arrhenius and Q10 models). Both equations fit the observational data equally with the optimized parameter values. The optimum apparent Q10 value was 1.47 $\pm$0.08 [95% C.I.]. Microzooplankton grazing rates closely matched the temperature trends for phytoplankton growth. This likely reflects a dynamic adjustment of biomass and grazing rates by the microzooplankton to match their available food source, illustrating tight coupling of phytoplankton growth and microzooplankton grazing rates. The field-measured temperature effect and growth rates

were compared with estimates from the satellite Carbon-based Productivity Model (CbPM) and three Earth System Models (ESMs), with model output extracted at the same month and sampling locations as the observations. The optimized, apparent Q10 value calculated for the CbPM was 1.51, with overestimation of growth rates. The apparent Q10 value in the Community Earth System Model (CESM V1.0) was 1.65, with modest underestimation of growth rates. The GFDL-ESM2M and GFDL-ESM2G models produced apparent Q10 values of 1.52 and 1.39 respectively. Models with an apparent Q10 that is significantly greater than ≈1.5 will overestimate the phytoplankton community growth response to the ongoing climate warming, and will have spatial biases in estimated growth rates for the current era.

4.2 Introduction

In order to accurately simulate marine carbon cycling, it is essential for models to accurately simulate marine net community production and export production. As global climate models and earth system models continue to grow in complexity, it is beneficial to revisit parameterizations as new data and findings come forth. A study comparing simulated marine primary production from numerical models of varying complexity has concluded that to improve modeled primary production there needs to be a better understanding of the temperature effect on photosynthesis and better parameterization of the maximum photosynthetic rate (Carr et al., 2006). The temperature influence on community phytoplankton growth rates is fundamental to simulating current and future marine primary production, and a reevaluation of this parameterization is needed to constrain how productivity will respond to climate change (Taucher and Oschlies 2011).

The influence of temperature on growth rates exist due to the control temperature exerts over metabolic rates (Raven and Geider 1988; Brown et al., 2004). A commonly used function

that describes the relation between temperature and growth rate is the Q10 model,

$$g = g_o \cdot Q10^{\frac{T-T_o}{10}} \tag{4.1}$$

where g_o is a reference growth rate (day^{-1}) at the reference temperature T_o = 303.15 K (30°C), and the Q10 value gives the factor change in growth rate for a 10 degree change in temperature. All temperatures used in the Q10 model are in Kelvin. Another commonly used function is the Arrhenius equation,

$$g = A \cdot e^{\frac{-E}{kT}} \tag{4.2}$$

where A is an adjustable constant (day^{-1}), E is the activation energy (eV), and k is the Stefan-Boltzmann constant (8.617 10^{-5} eV K^{-1}). In both equations the temperature, T, is measured in Kelvin. Both equations can be used to describe the influence of temperature on phytoplankton growth assuming other factors such as light and nutrients are held constant.

One key early study, compiling mostly laboratory growth rate data, suggested a phytoplankton Q10 value of 1.88 (Eppley 1972), while another suggested a value of 2.08 (Goldman and Carpenter 1974). At the time, growth rate data were scarce, and mostly from lab cultures. As a result, the sample size of early synthesis efforts was relatively small and limited to species in culture. Thus, the described temperature effects may not be representative of in situ rates for natural populations. Calbet and Landry (2004) compiled field estimates of phytoplankton community growth rates, and showed increasing growth rates as one moved from polar to tropical waters. However, the change in growth rate implied a weaker temper-

ature effect than a Q10 value of 1.88 or 2.0 would imply. This study attempts to build on these efforts by collecting and analyzing a large database of field observations of phytoplankton community growth rates, in comparison with satellite and Earth System Model (ESM) estimates.

4.3 Methods

The goal of this study is to evaluate the temperature effect on phytoplankton community growth rates, and to estimate optimal growth-rate parameters for marine ecosystem models, based on either the Arrhenius equation or the Q10 model. To this end we compiled from the literature a large dataset of in situ phytoplankton community growth rates (n = 835, Table 4.1, Figure 4.1; building on a previous compilation by Calbet and Landry (2004)) measured using the dilution method (Landry and Hassett 1982). (Refer to supplementary material for the compiled database). The dilution method of Landry and Hassett (1982) provides estimates of phytoplankton community growth rate and total microzooplankton grazing rate. Additional ancillary information was compiled where available, including geographic location, depth, chlorophyll concentration (mg/m^3), nitrate concentration (μM), temperature (°C), and sampling month. To minimize the role of light limitation, we only included upper water column experiments ($<$ 30 m depth). We also excluded experiments where the linear regression used to estimate phytoplankton growth rate had a low r2 value ($<$ 0.33). Temperature was reported for 576 of these experiments, and showed a good correlation with the sea surface temperature predicted from the Community Earth System Model (CESM) - Biogeochemical Elemental Cycling (BEC) ocean biogeochemical model (Moore et al., 2004) (r = 0.937, Figure 4.2). Therefore, where temperature was not reported we substituted the monthly mean model sea surface temperature from the 1990s for that location (hereafter referred to as the combined temperature dataset). The CESM sea surface temperatures are a good match to the observations for the 1990s (r=0.99, Moore et al., 2013).

The satellite product analyzed was from the Carbon-based Productivity Model (CbPM), and was extracted at the same geographic location and month as the in situ data (Behrenfeld et al., 2005; Westberry et al. 2008; www.science.oregonstate.edu/ocean.productivity/index.php). A monthly climatology of CbPM growth rate estimates was created from 1999 to 2008. Growth rate estimates from the original CbPM from the Behrenfeld et al. (2005) study had a tendency to overestimate water column production from errors in photic zone depth. An updated version of the CbPM was used in this study (Westberry et al. 2008). The updated CbPM uses euphotic zone depths that are calculated from reconstructed profiles of irradiance based on profiles of chlorophyll/carbon and biomass. Temperature from our combined temperature dataset and CbPM growth rates were used to find the apparent Q10 coefficient and reference growth rate for the CbPM, subsetting the satellite data at the same month and location as the data in our in situ database. The CbPM does not include an explicit temperature effect on growth rates, but estimates growth as a function of the phytoplankton chlorophyll/carbon ratio (Behrenfeld et al., 2005; Westerberry et al., 2008).

The CESM-BEC model includes ecosystem and biogeochemical components. Three phytoplankton functional groups (diatoms, diazotrophs, and small phytoplankton) and the cycling of key biogeochemical elements (C, N, P, Fe, Si and O) are represented (Moore et al., 2004; Moore and Braucher, 2008). The Q10 model is used to simulate the temperature dependence on phytoplankton growth rates (Explicit Q10 = 2.0). The BEC model runs within the Parallel Ocean Program model, which is a part of the larger Community Earth System Model (CESM 1.0) (Gent et al., 2011; Danabasoglu et al., 2012; Moore et al., 2013). The GFDL models also include multiple phytoplankton groups and a Q10 model of temperature impacts on growth (Explicit Q10 = 1.88) (Bopp et al., 2013; Dunne, 2013). We define the explicit Q10 as the value assigned to individual phytoplankton groups within the models. This can differ from the emergent, or apparent Q10 factor, for the influence of temperature on community growth rates when the model output is analyzed in the same manner as the field data.

The three ESM simulations used in this study are from the Coupled Model Intercomparison Project 5 (CMIP5). Model simulations were conducted following the CMIP5 guidelines (http://cmip-pcmdi.llnl.gov, see Moore et al. 2013 for details). Model resolution for the BEC is ∼1 degree, and 1 degree for the GFDL models. Phytoplankton community growth rates were calculated by weighting the net primary production of each phytoplankton functional group (diatoms, diazotrophs and small phytoplankton) and dividing by the fractional component of community biomass in the upper 20m of the water column. A monthly climatology for 1990s period was created for community phytoplankton growth rates from the CESM (see Moore et al., 2013 for additional details and validation comparisons with observed biogeochemical and physical oceanographic fields). Modeled growth rates were extracted at the same location and sampling month as the in situ observations. The same approach was used for the GFDL-ESM2M and GFDL-ESM2G models. Averaged historical CMIP5 output from years 1990 to 1995 were used to construct a monthly climatology. Primary carbon production by phytoplankton (CMIP5 variable pp, [mol m^{-3} s^{-1}]) was divided by phytoplankton carbon concentration (CMIP5 variable phyc, [mol m^{-3}]) at the in situ observational locations over the upper 20m to estimate community net growth rates.

Using the temperature and the phytoplankton community growth rates (from the field data and from each model) we fit the temperature equations to determine the apparent phytoplankton community temperature-growth relationship. We define the apparent Q10 as the calculated optimal value fitting the Q10 model to the growth and temperature data. Thus the apparent, community Q10 value is calculated in the same way for the field measurements and for the models (model output sub-sampled only at the locations of the field observations). The explicit Q10 is the parameter value specified in numerical models for individual plankton groups, which can differ from the phytoplankton community apparent Q10 value.

To estimate the parameters of the Q10 and Arrhenius models we applied a logarithmic transformation to each model to make them linear in their adjustable parameters. We then

used ordinary least squares to estimate ln(Q10) and ln(g_o) for the Q10 model and to estimate ln(E) and ln(A) for the Arrhenius model. For temperatures in the range found in the oceans, the curvature of the graph of 1/kT versus T (when T is measured in units of K) is negligible - for the temperature range between °C to 32°C the relative error made in approximating 1/kT by a linear function of T is less than one part in 10^5 - so that the temperature dependence of both models is practically identical (Dixon and Webb,1964). This makes it impossible to select one model over the other based only on the quality of their respective fit to the in situ data. For the temperature range between -2°C and 32°C we can relate E to Q10 using Q10 = exp((δT E)/(k$\bar{T}^2$)), where δT = 10 K and $\bar{T}$= 288.15K (Dixon and Webb,1964).

To assign uncertainties to our estimates of the optimized parameter values, we assumed normally distributed errors for the logarithmically transformed growth rate data and reported 95% confidence intervals assuming uniform prior probabilities for the parameters. For the Arrhenius model there is a very strong correlation in the posterior probability of E and log(A), (p=0.9995). This makes the optimal value of A extremely sensitive to the value of E. We have therefore reported the uncertainty for A conditioned on E fixed at its optimal value. The unconditional uncertainty for A, obtained after marginalizing out E, is A = (3.5 $\pm^{2.80}_{13.50} \times 10^4)day^{-1}$.

4.4 Results

There is a strong influence of temperature on growth rates apparent in the observational dataset. Mean phytoplankton community growth rates, averaged within 3°C temperature bins, are plotted against temperature in Figure 4.3a. We estimated an optimal apparent Q10 value of 1.47 ± 0.08 [95% C.I.] with a reference growth rate at 30°C of 0.89 ($\pm^{0.08}_{0.07}$)day^{-1} [95% C.I.] (without log transformation the optimal Q10 value was 1.38) . We estimate an optimal activation energy of E = 0.28 (±0.04) eV [95% C.I.] for the Arrhenius equation. The optimal

value of A depends sensitively on the assumed choice for the activation energy. Conditioned on E fixed at its optimal value of 0.277 eV, we estimate A = $(3.5 \pm^{2.80}_{13.50} \times 10^4) day^{-1}$ [95% C.I.]. Figure 4.3 shows that both optimized models fit the data equally well, with approximately the same root mean square error of 0.45 day^{-1} (Table 4.1).

Our estimated activation energy of 0.28 ($\pm$0.04) eV is in good agreement with other estimates. Previous studies have found activation energies that range from 0.29 eV to 0.32 eV (Allen et al., 2005; Lopez-Urrutia et al., 2006; Regaudie-de-Gioux and Duarte 2012). However, our apparent Q10 value of $\sim$1.5 is significantly lower than the canonical value of 2.0 often used when assigning explicit Q10 values in models (Eppley 1972; Goldman and Carpenter 1974; Bissinger 2008). An apparent Q10 value of 2.0 overestimates the effect of temperature on community phytoplankton growth rates. This is illustrated in Figure 4.3, which compares our optimized equations with the growth rate computed as a function of temperature for a fixed apparent Q10 value of 2.0, and an optimized reference growth rate of 1.33 day^{-1} (blue line). Note the much steeper slope compared with the observational dataset.

To assess the influence of nutrient limitation in the observational dataset we compare subsets of the data from the studies that estimated growth rates both with and without nutrient addition (n= $\sim$200, Table 4.1). We calculated the apparent Q10 value for subsets of the data both with and without nutrient addition. The apparent Q10 value calculated from the experiments with nutrient additions is 1.48, and the apparent Q10 value calculated from the data without nutrient additions is 1.42, with overlapping 95% confidence intervals (Table 4.1). The very similar apparent Q10 values strongly suggest that spatial or temperature-correlated patterns in the degree of nutrient stress are not strongly skewing our optimized apparent Q10 values. However, the reference growth rate was higher in the nutrient-addition subset (1.1 day^{-1} versus 0.65 day^{-1} without nutrient addition, Table 4.1), demonstrating significant nutrient limitation of the in situ community growth rates. The estimated reference

growth rate with nutrient limitation was 65% of the reference growth rate with no nutrient limitation value. These results together indicate that the degree of nutrient limitation was not correlated with temperature, but was in fact very similar across different regions.

To further explore the role of nutrient and light limitation, we analyze output from the CESM-BEC model. We take the existing simulation results and calculate what the growth rate would have been without the nutrient and/or light limitation terms. This is a simplified approach, in that we assume that phytoplankton biomass and community composition are not changed, and by removing the light-limitation term we assume a saturating light field 24 hours per day. Then we re-fit the Q10 model with the modified growth rates. Modeled growth, both with and without nutrient limitation, was extracted at the same location and month as all of the in situ observations. Figure 4.4a shows BEC simulated growth (with nutrient limitation) versus temperature. Figure 4.5a shows BEC simulated growth without any nutrient limitation (assuming that phytoplankton biomass and community composition remain the same) versus temperature. The apparent Q10 value for CESM-BEC growth with nutrient limitation is 1.65±(0.06) with a reference growth rate of $0.86\pm(^{0.10}_{0.09})$, while the apparent Q10 value without nutrient limitation is 1.70±(0.02) with a reference growth rate of 1.73±(0.03). Much like in the observational dataset, we only see a modest nutrient influence on the apparent Q10 factor, but the reference growth rate is again significantly different. The reference growth rate with nutrient limitation for the BEC was 50% of the estimated rate without nutrient limitation. Overall, the CESM-BEC model (with nutrient limitation) slightly underestimates phytoplankton community growth rates in comparison to the in situ observations with the largest underestimation at low temperatures (Figure 4.4d).

Light limitation could potentially skew our analysis of the temperature influence on community phytoplankton growth rates. Figure 4.5b shows CESM-BEC community phytoplankton growth, at the in situ locations, without nutrient or light limitation. There is only a modest difference in apparent Q10 values without nutrient limitation (apparent Q10=1.7025)

and without nutrient and light limitation (apparent Q10=1.8982). The large majority of the field dilution experiments were sampled near the surface (∼5m) and incubated on deck (we excluded deep euphotic zone experiments). We therefore believe light limitation is not significantly skewing our results. Growth rates calculated without light limitation assume a 24 hours per day photoperiod, resulting in unrealistically high growth rates at low latitudes. Accounting for the latitudinal variations in summer-season photoperiod length would tend to flatten the growth-temperature relation (longer photoperiod at high latitudes), which may partially explain the ∼0.2 difference in apparent Q10 values noted above.

Diazotrophs have inherently slower growth rate than other phytoplankton (i.e., Falcon et al., 2005; Breitbarth et al., 2007), which has been incorporated in the CESM-BEC (Moore et al., 2004). The diazotrophs are excluded from high-latitude waters in the model by temperature constraints (Moore et al., 2004). If phytoplankton community biomass was weighted more towards diazotrophs in warmer regions, this may skew the apparent Q10 value low. Figure 4.5c shows BEC community phytoplankton growth rates without nutrient and light limitation while also excluding diazotrophs from the phytoplankton community at the in situ locations. Comparing the apparent Q10 value without nutrient and light limitation (apparent Q10=1.8982) and the apparent Q10 value without nutrient and light limitation and excluding diazotrophs (apparent Q10=2.0) we find the difference to be 0.1018. These results suggest that diazotrophs are not strongly skewing the in situ apparent Q10 estimation, which would still be an apparent Q10 value significantly lower than 2.0. The diazotrophs typically only account for 1-3% of primary production in the CESM, even in warm water, nutrient depleted regions. Diazotrophs would be included in the field estimates as well, and may contribute to the apparent modest flattening of the growth versus temperature relation at the warmest temperatures (Figure 4.3).

Although there is no explicit temperature effect included in the CbPM, there is a positive correlation between temperature and phytoplankton growth rates. The CbPM growth

rates are driven by the satellite estimates of the phytoplankton chlorophyll/carbon ratio. It appears that this ratio must correlate strongly with temperature at the global scale. We estimated an apparent Q10 value of 1.51(0.06) with a reference growth rate of $1.39(\pm^{0.10}_{0.09})$ at 30°C. Figure 4.4b shows CbPM growth rates versus temperature and estimated growth rates using the Q10 model and apparent CbPM Q10 value and reference growth rate values. The CbPM matches well the growth-temperature relation seen in the field data, but consistently overestimates community growth rates (Figure 4.4d).

Using data from the CMIP5 archives we also calculated apparent Q10s and reference growth rates for the GFDL-ESM2M and GFDL-ESM2G models (Figure 4.6). The GFDL-ESM2M apparent Q10 is 1.52±(0.02) with a reference growth rate of 1.08±(0.03). This apparent Q10 value closely matches the observation-based estimate of 1.47, however the reference growth rate is higher than in the observations, leading to a modest overestimation of community phytoplankton growth rates that increases with temperature (Figure 4.6). The GFDL-ESM2G apparent Q10 is 1.39±(0.02) with a reference growth rate of 0.82±(0.02).

Chen et al. (2012) reported a positive correlation between increasing temperatures and microzooplankton grazing rate/phytoplankton community growth rate for eutrophic conditions. Contrary to the findings of Chen et al. (2012) and Rose and Carons (2007) trophic decoupling by temperature theory, we found no temperature influence on the ratio of microzooplankton grazing rate/phytoplankton community growth rate (Figure 4.7a). We note that our examination of microzooplankton grazing rate/phytoplankton community growth rate was not assessed with respect to chlorophyll concentrations as was done in Chen et al. (2012).

There was a strong temperature trend for the microzooplankton grazing rates, nearly exactly matching that observed for phytoplankton growth rates (Figure 4.7b). Fitting our Q10 equation to the grazing rates gives an apparent Q10 value of 1.470.08 with a reference grazing rate at 30°C of 0.57±0.05 day^{-1}. This likely reflects not only the temperature sensitivity

of the grazer populations, whose respiration likely scales more strongly with temperature (Lopez-Urrutia et al., 2006; Regaudie-de-Gioux and Duarte 2012), but also a dynamic adjustment of grazing pressure (by modifying microzooplankton biomass and grazing rates) to match available food resources (a function of phytoplankton growth and biomass) (Peters, 1994). Most of the time, over much of the ocean there is a relatively tight coupling between primary production and grazing (Calbet and Landry 2004; and references therein). There was no correlation observed between phytoplankton community growth rates and nitrate or chlorophyll concentrations for the subset of studies that reported ambient nitrate and chlorophyll (Table 4.1, Figure 4.8).

The global mean growth rate for all the field observations was 0.71 day-1 and the mean grazing rate was 0.47 day^{-1}, indicating that on average about 66% of daily production was grazed by the microzooplankton. Dividing our computed reference grazing rate (0.57 day^{-1}) by the reference growth rate (0.89 day^{-1}), gives a similar value of 64% of daily production being grazed. The Calbet and Landry (2004) dataset had similar mean values of 0.67 day^{-1} for growth and 0.41 day^{-1} for grazing, which implies 61% of daily production on average being grazed. There are additional mortality terms in the model including a non-grazing mortality loss meant to account for losses to viruses, excretion, and respiration, and an additional loss to aggregation and sinking (Moore et al., 2004).

4.5 Discussion

It is perhaps not surprising that a weaker temperature-growth relation is observed in natural phytoplankton communities across ecosystems than has been observed in culture studies with single species. At the global scale, the dominant component of phytoplankton communities will be well-adapted to ambient temperatures. For example, phytoplankton can adapt to low temperatures by modifying internal resource allocations to compensate for some of the most

temperature sensitive metabolic reactions (Raven and Geider, 1988). Our results indicate that such adaptations may weaken, but certainly do not erase the temperature influence on metabolism and growth. It is important to keep in mind that our findings apply to the phytoplankton community growth rate at the global scale. It is possible that individual species, which typically thrive only in a fairly narrow temperature range (i.e., Eppley, 1972), but are well adapted for those temperatures, could all exhibit growth-temperature relations with an apparent Q10 value of 2.0, but when combined at the community level produce a weaker apparent growth-temperature relation as we report here. Phytoplankton may have more mechanisms to optimize and acclimate for growth at low temperatures than for high temperatures, for example by producing more substrates for the most temperature sensitive metabolic reactions (Raven and Geider, 1988). The longer summer-season photoperiod at high latitudes likely also plays a role in weakening the growth-temperature relation.

There was considerable spread in the data for any given temperature range (about one order of magnitude, Figure 4.3a, 4.3b). This could be due to several factors, including the seasonally varying nutrient and light fields, species-specific differences, bloom progression status, and experimental error in the measurements. One might expect the warmer waters to be more strongly nutrient limited, with a stronger suppression of growth rates. There is little indication of the growth rates falling off the optimal trend line, except at the very highest temperatures in the binned data (Figure 4.3a).

It appears that as community composition shifts in response to nutrient availability, often correlated with temperature, the resulting community growth rates and the relative degree of nutrient stress are similar across marine ecosystems at the global-scale, even as ambient nutrient concentrations and total phytoplankton biomass vary widely. This effect is seen in the relatively constant apparent Q10 values with and without nutrient stress in both the field observations and the CESM-BEC model output. The very small phytoplankton that dominate the community in warm, stratified regions, where nutrients are typically scarce,

are extremely efficient at taking up nutrients (Agawin et al., 2000; Raven 1998). This allows them to grow relatively quickly even when ambient nutrient concentrations are quite low. In regions with higher ambient nutrient concentrations, a larger fraction of the phytoplankton community will be made up of larger species, such as diatoms, that are much less efficient at nutrient uptake. The shifting community structure appears to adjust so that the relative degree of nutrient stress for the community is similar across biomes.

Our results show that the apparent Q10 value for phytoplankton community growth rates for natural populations is approximately 1.5. Utilizing the Arrhenius equation with an activation energy of ∼0.28 eV would be equally good at predicting the growth response to changing temperatures. Global-scale marine ecosystem models with only one phytoplankton group, or a few phytoplankton functional types, should strive to match the apparent Q10 value seen in our observational dataset. This may require explicit Q10 values imposed in the model that are less than the values of 1.88 or 2.0 often used today (or an equivalent Arrhenius model). Models that include a large number of phytoplankton types, or that explicitly account for internal resource allocation strategies to adapt to low temperatures, could a include a range of group-specific explicit Q10 values, but their integrated community growth rates should be compared with the observational dataset compiled here to ensure that the phytoplankton community growth rate displays a temperature sensitivity equivalent to an apparent Q10 value of ∼1.5.

Parameterization of the temperature effect on phytoplankton growth rates is important for simulating net primary production, especially under climate change scenarios (Taucher and Oschlies, 2011). Laufkotter et al. (2015) examined a suite of the CMIP5 ocean biogeochemical models, and suggested that the temperature-growth relationship could be as important as nutrient concentrations in driving NPP-climate interactions at the lower latitudes. Models with stronger temperature sensitivity (i.e., apparent Q10 value = 2.0) in their phytoplankton community growth rates, will overestimate the response to ongoing ocean warming, and will

have strongly biased growth rates in some regions for the current era.

4.6 Acknowledgements

We would like to thank all the researchers and technicians who helped collect the phytoplankton growth, grazing and other ancillary data that made this work possible. This contribution was supported by a grant to J.K. Moore as a part of the BGC Feedbacks Scientific Focus Area within the Regional and Global Climate Modeling (RGCM) Program in the Climate and Environmental Sciences Division (CESD) of the Biological and Environmental Research (BER) Program in the US Dept. of Energy Office of Science. Dr. Moore also received support from the NSF project Collaborative Research: Improved Regional and Decadal Predictions of the Carbon Cycle(AGS-1048890). Refer to Supplementary material for the compiled database.

4.7 Figures

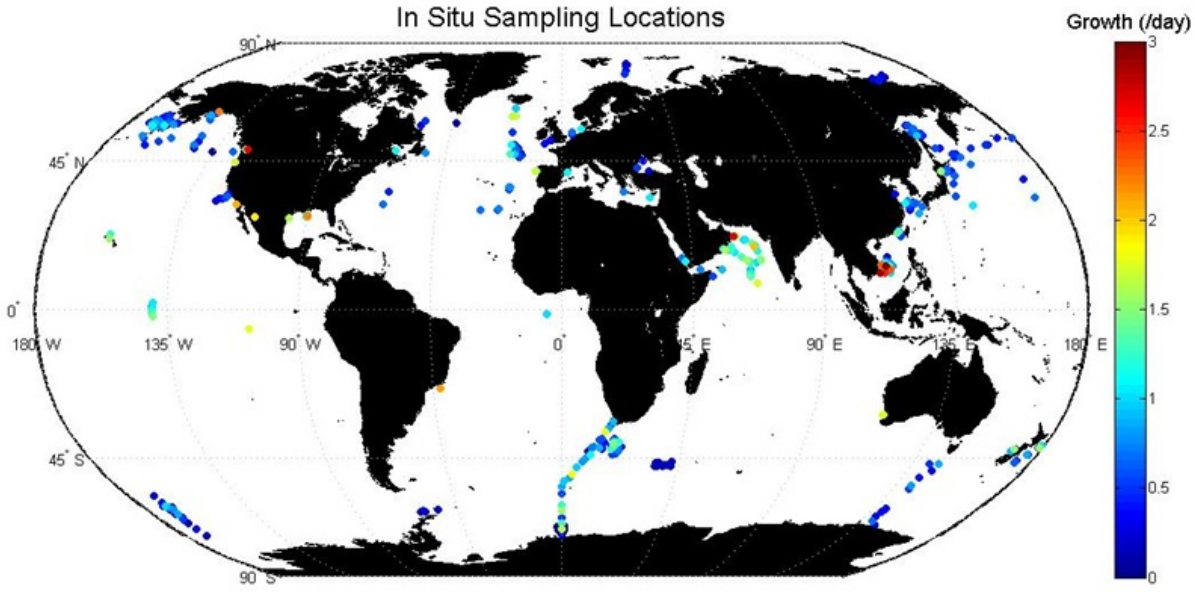

Figure 4.1: Spatial plot showing locations and observed phytoplankton community growth rates from the in situ dataset.

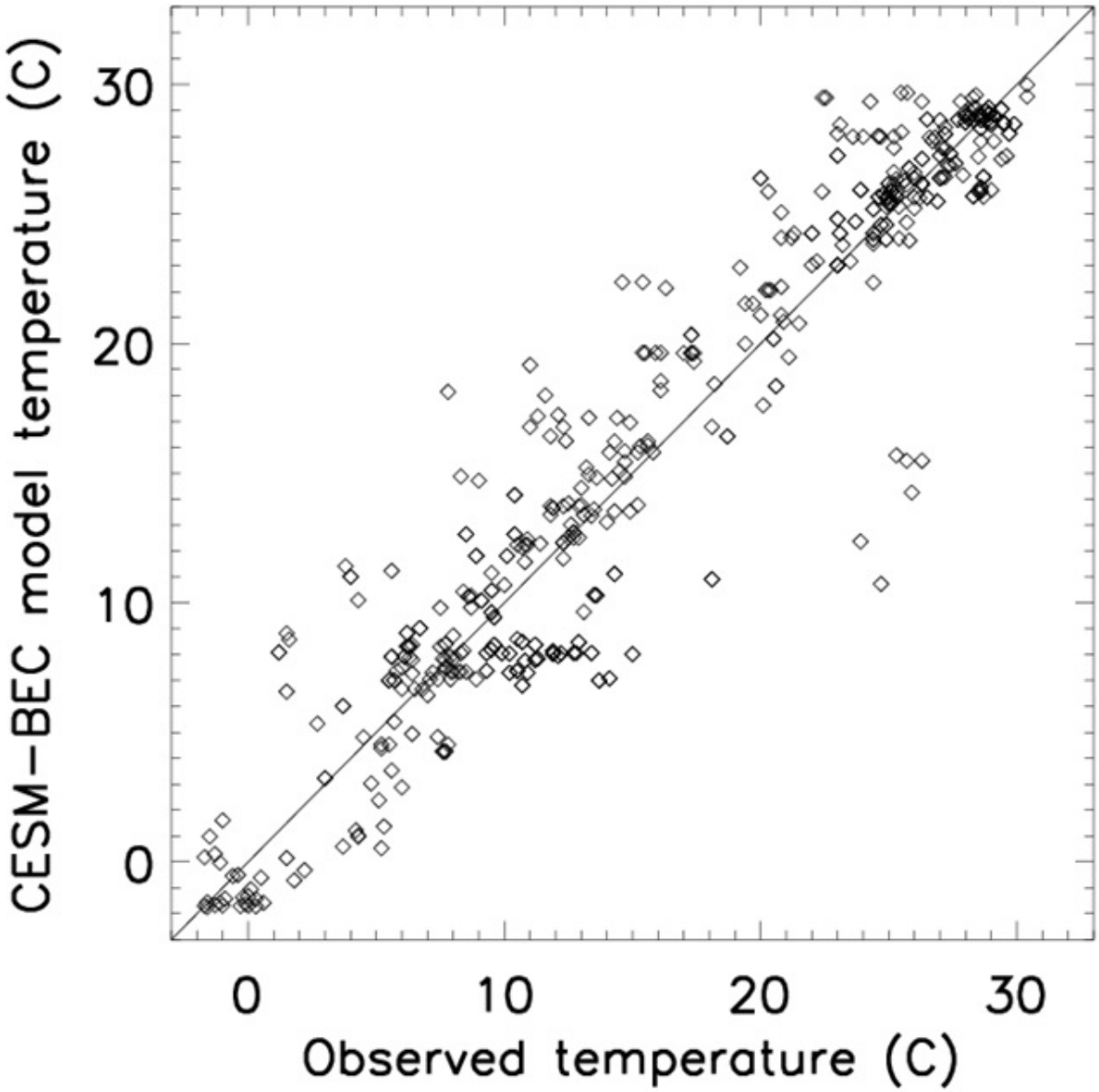

Figure 4.2: Scatter plot of BEC model sea surface temperature versus observed temperature for locations where temperature was reported in the field experiments.

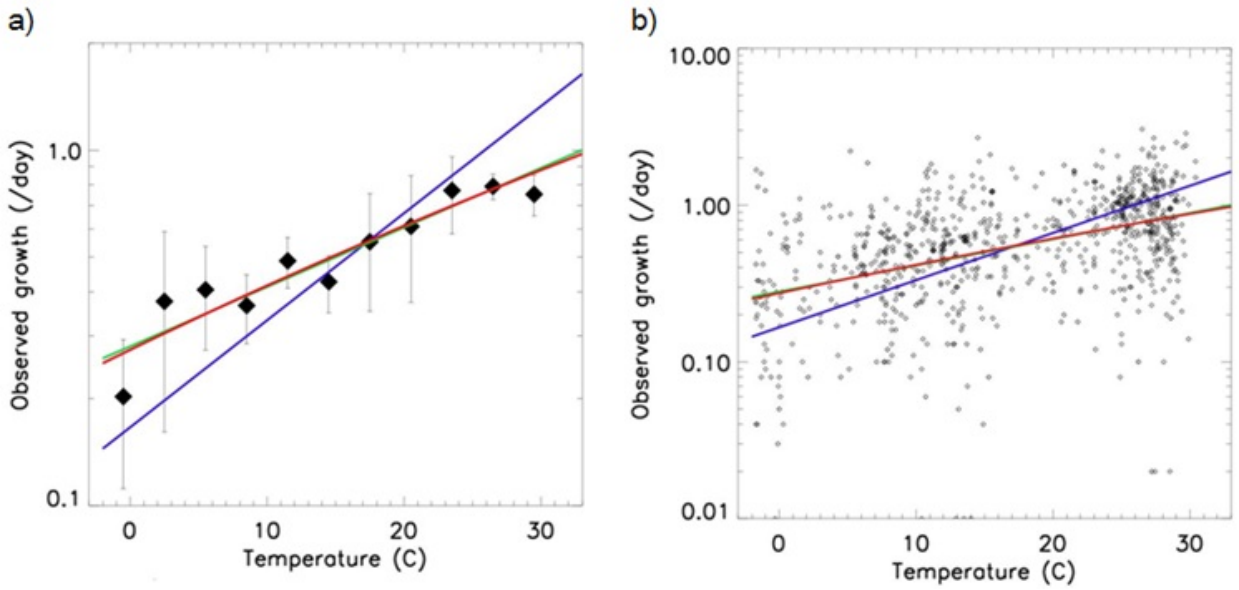

Figure 4.3: Observed phytoplankton community growth rates are plotted versus temperature averaged within 3°C bins (4.3a). Error bars show the 95% confidence intervals. The green line displays the modeled growth-temperature relation with the best fit to the Q10 equation (apparent Q10 value of 1.47). The red line (nearly identical to green) is the modeled growth-temperature relation with the best fit of the Arrhenius equation (activation energy of 0.28 eV, A coefficient value of 3.53 x 10^4, see text for details). The blue line shows the modeled growth-temperature relation with the best fit of the Q10 growth equation, imposing an apparent Q10 value of 2.0. Panel 4.3b displays the original un-binned data with the same three trend lines.

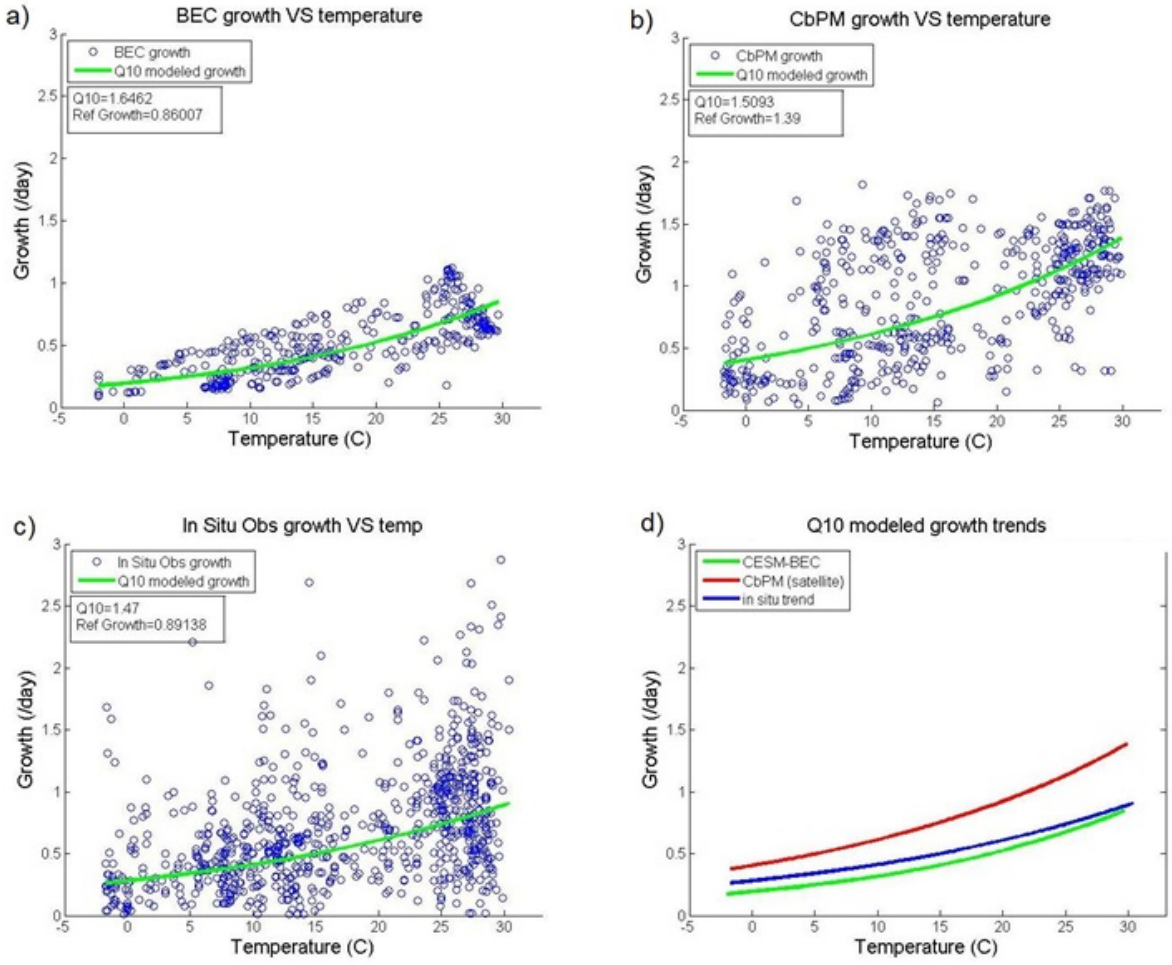

Figure 4.4: Panel 4.4a shows BEC community phytoplankton growth rates versus temperature at in situ sampling locations. Panel 4.4b shows CbPM community phytoplankton growth rates versus temperature at in situ sampling locations. Panel 4.4c shows in situ observations versus temperature. Panel 4.4d shows the Q10 modeled growth from panels 4.4a, 4.4b, and 4.4c plotted against temperature. Reported Q10 values are apparent values.

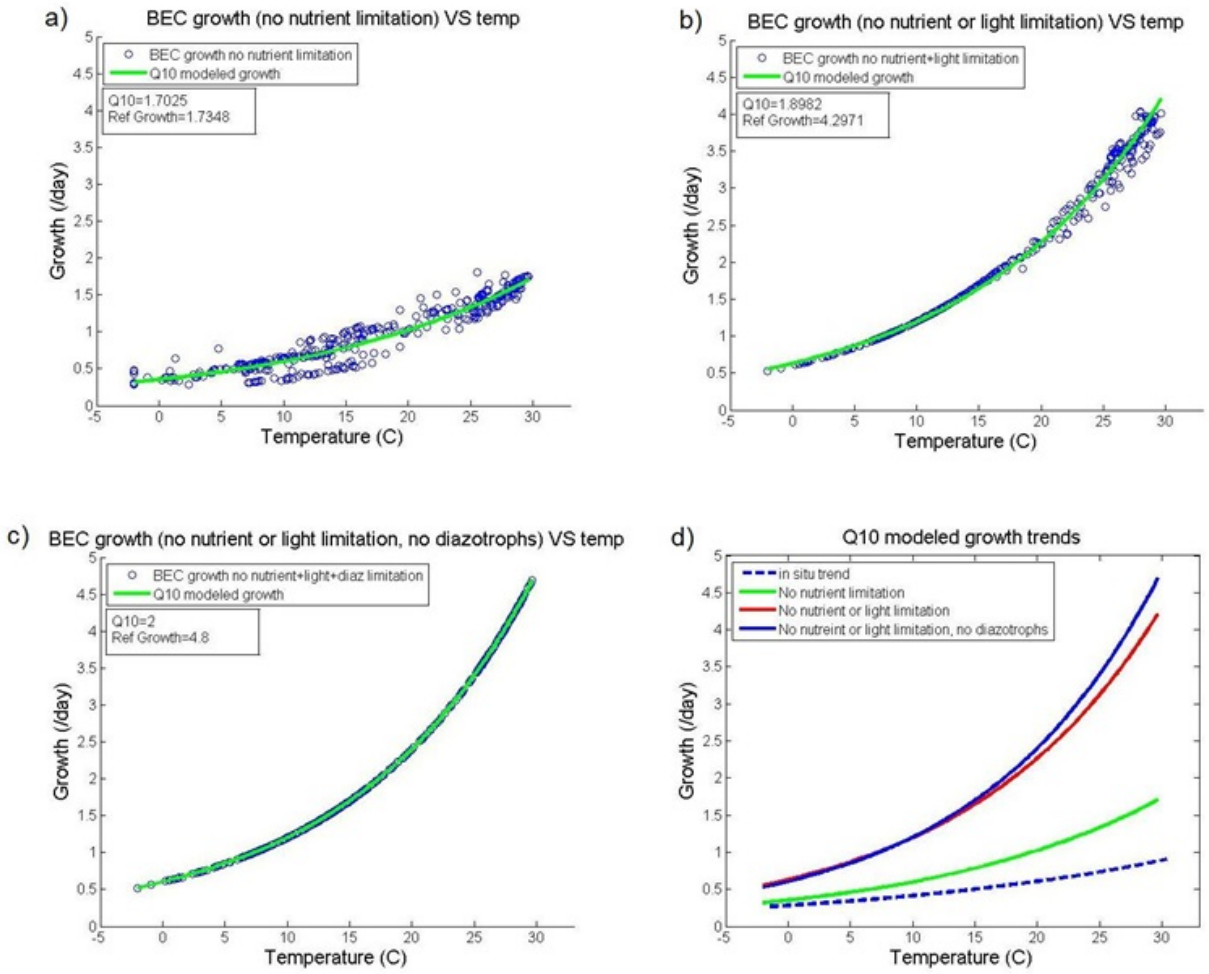

Figure 4.5: All growth rates shown are phytoplankton community growth rates. Panel 4.5a shows BEC growth without nutrient limitation versus temperature. Panel 4.5b shows BEC growth without nutrient or light limitation versus temperature. Panel 4.5c shows BEC growth without nutrient, light, or diazotrophs versus temperature. Panel 4.5d shows the Q10 modeled growth from panels 4.5a, 4.5b, and 4.5c plotted against temperature. Reported Q10 values are apparent Q10 values.

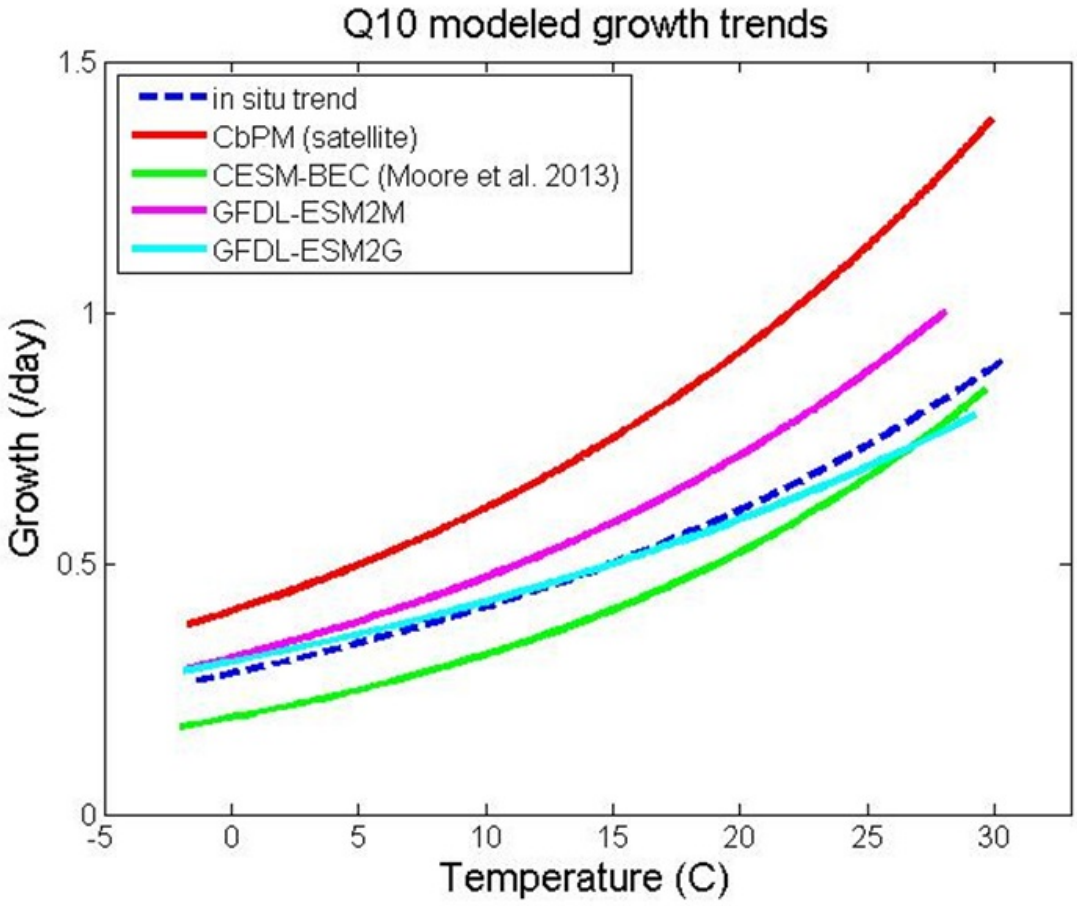

Figure 4.6: Q10 modeled growth, using respective apparent Q10 values and reference growth rates, for in situ observations, CbPM, CESM-BEC, GFDL-ESM2M and GFDL-ESM2G.

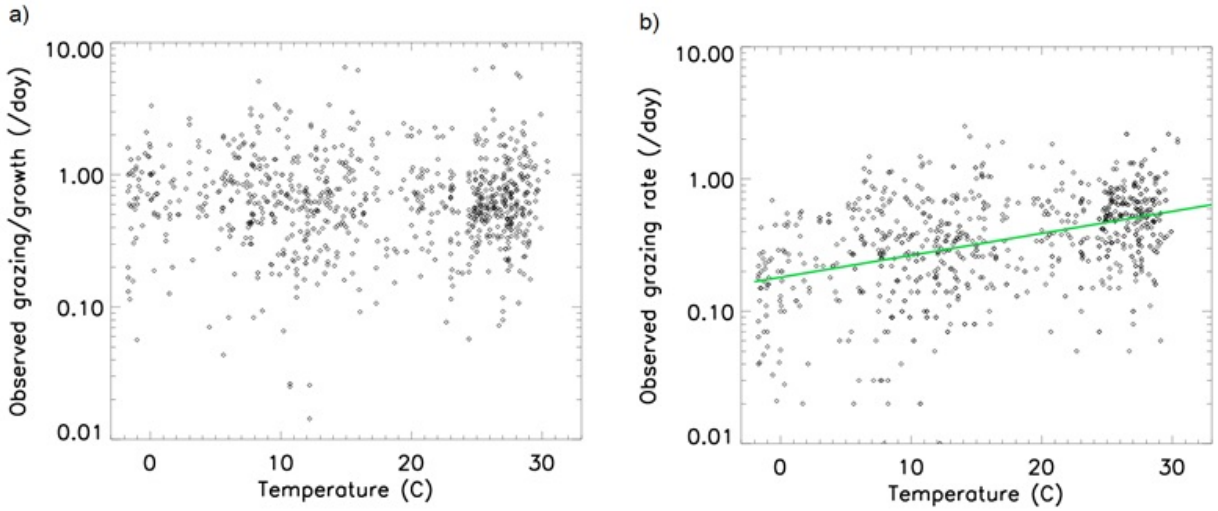

Figure 4.7: The ratio of observed microzooplankton grazing rate / phytoplankton community growth rate is plotted as a function of temperature (4.7a). Panel 4.7b displays the microzooplankton grazing rate as a function of temperature, with an optimal fit of the Q10 equation (here as the Q10 function multiplied by a reference grazing rate at 30 °C, see text for details)

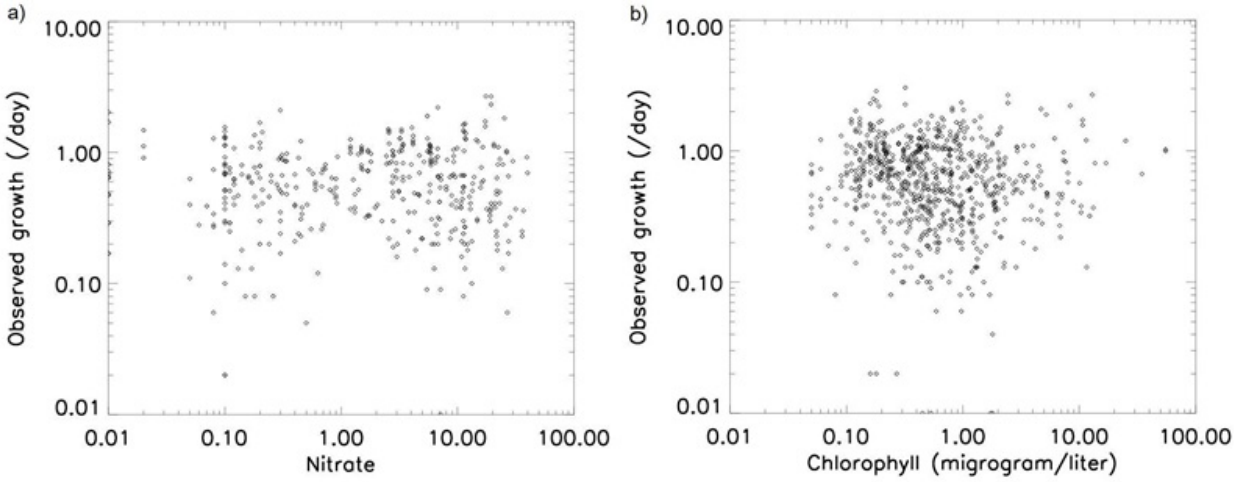

Figure 4.8: Observed phytoplankton community growth rates are plotted against observed nitrate in plot 4.8a, and observed phytoplankton community growth rates are plotted against observed chlorophyll concentrations in plot 4.8b.

4.8 Tables

	All	BothAdd	BothNoAdd
N	835	203	209
Temp (C°)	16.9626	20.9541	21.4408
Chl (µg/L)	1.3963	1.4475	1.2243
Nitrate (µM)	5.4873	5.0837	4.7001
Growth (day^{-1})	0.7055	0.9367	0.6526
Grazing (day^{-1})	0.4685	0.4939	0.5137
Grazing/Growth	0.6641	0.5272	0.7872
Fitted Q10	1.47	1.48	1.42
Fitted Q10 Ref. Growth Rate	0.89	1.1	0.65
Fittted Q10 rmse	0.4465	0.4541	0.4467
Fitted A coefficient	3.5315×10^4	5.9886×10^4	1.2013×10^4
Fitted E	0.2770	0.2852	0.2568
Fitted Arrhenius rmse	0.4462	0.4541	0.4468
Imposed Q10 2.0	2.0	2.0	2.0
Imposed Q10 2.0, Fitted Reference Growth Rate	1.33	1.41	0.88
Imposed Q10 2.0, rmse	0.4619	0.4619	0.4882

Table 4.1: Shown are the mean values and fitted growth equations for the entire observational database, and for the BothAdd and BothNoAdd subsets. These subsets include results from the field where experiments were conducted both with and without nutrient addition. BothAdd represents experiments where nutrients were added. BothNoAdd are experiments where nutrient additions were omitted.

Chapter 5

Conclusions

The iron cycle is an important component of biogeochemistry in the oceans as it's a strongly limiting micronutrient for phytoplankton. Dissolved iron is stabilized through complexation with organic ligands, which help prevent losses to particle scavenging. Research into the cycling of iron-binding ligands is still developing and large uncertainties remain with regards to its cycling processes. Identifying and quantifying the major cycling terms for iron-binding ligands will help elucidate what controls the distribution of dissolved iron in the oceans. Large uncertainties also exist for iron cycling processes. The Iron Model Intercomparison Project highlighted these uncertainties and how they have manifested into global biogeochemical ocean models (Tagliabue et al., 2016). Rates of iron source processes can vary by a factor of ten amongst models, yet all models can generally reproduce observed iron concentrations. This is because modelers tune their scavenging losses to best match observed concentrations. Due to the wildly differing source and sink rates for iron between models, the strength of the feedbacks between iron and other biogeochemical processes and climate could differ greatly. Sensitivity experiments of iron source processes should be conducted for global ocean biogeochemical models to quantify their sensitivity to iron sources and impacts on other biogeochemical processes. This would provide a baseline for interpretation and comparison amongst model results. The work presented in this dissertation aims to reduce the described unknowns of the marine iron cycle.

In chapter one we present results from the CESM which includes modifications to explicitly simulate iron-binding ligands and its speciation with iron. A ligand tracer, variable in space and time, was implemented into the CESM with explicit source and sink processes. The ligand component of the CESM was able to simulate ligand concentrations that compared well against observations along the GEOTRACES GA03 transect. Inclusion of a dynamic ligand tracer also improved the simulation of iron. The simulated ligand distributions appear a bit conservative compared to observations from Gerringa et al. (2015). This suggests we are likely missing some ligand source and sink processes. Many models assume a constant ligand concentration of $\sim$1 nM. Our results show that assuming a constant ligand concentration poorly matches observed ligands and places a strong constraint on the upper bound concentration for iron and the total iron inventory. Current knowledge of ligand cycling suggests it is strongly mediated by biology. Prescribing a constant ligand concentration may be problematic for simulation different climate scenarios as it will not capture the feedbacks between iron, ligands, biology and other biogeochemistry.

In chapter two we conduct sensitivity simulations of iron sources to better understand how each iron source impacts dissolved iron distributions and biogeochemistry in the model. Each iron source is turned off while the others remain active. The iron sources include: surface soluble iron from atmospheric dust, subsurface iron release from dust, sedimentary iron, river iron and iron from hydrothermal vents. Our results show that sedimentary iron had the largest impact on iron concentrations throughout the water column, except for regions of high dust deposition where the atmospheric dust source is more influential. Surface soluble iron from dust had the largest impact on biogeochemistry producing the largest reductions in NPP, export production, nitrogen fixation and iron limitation. However the sedimentary iron source still strongly impacted ocean biogeochemistry and shifted phytoplankton community composition towards small phytoplankton. Iron from hydrothermal vents had a strong impact on iron concentrations in the deep ocean. Our results suggest that hydrothermal vents have little impact on biogeochemistry on a global scale, but that shallow vents

may have regional importance. River iron did not significantly impact iron concentrations or biogeochemistry but may be important for coastal biogeochemistry.

The third chapter we reevaluate the temperature influence on community phytoplankton growth rates for use in global ocean biogeochemical and ecosystem models. We compile a dataset of in situ community phytoplankton growth rates and conduct an ordinary least squares regression to optimize the parameters for the Q10 and Arrhenius temperature-growth models. Our results show that both models are able to fit the data equally. The optimal apparent Q10 value was 1.47 and activation energy is 0.28 eV. Our optimized Q10 value is lower than what is traditionally used in models. Models with an apparent Q10 greater than $\sim$1.5 will likely overestimate the growth response to a warming climate. We also find that zooplankton grazing rates closely matched the temperature trend for community phytoplankton growth. This likely suggests an adjustment of zooplankton grazing rates to the available food source.

This dissertation helped to reduce uncertainties associated with the cycling of ligands in the ocean and their impacts on dissolved iron, modeling the iron cycle and the temperature influence on community phytoplankton growth rates. However, a great deal of uncertainty still exists for the dissolved iron budget of the ocean. Because of the influence iron has as a limiting nutrient, the influence on nitrogen fixation and the associated biogeochemical feedbacks it is imperative that the iron budget in the oceans is resolved. Ocean biogeochemical and Earth System models may predict an incorrect climate response to changes in the iron cycle without better observational constraints on the iron budget. The closing of the marine iron budget is currently the most important question in iron biogeochemistry.

To close the iron budget one would need to know the total flux of sources or sinks assuming a steady state. There are multiple sources for iron in the oceans, and creating datasets that encompass all of the sources heterogeneity in space and time is challenging. Atmospheric dust deposition is highly seasonal and patterns of deposition are highly dependent on the weather.

The solubility of the iron within the dust is highly variable and is influenced by processing in the atmosphere during transit. To quantify the benthic flux of iron would require a network of flux chambers dispersed throughout the world's continental shelves and along the ocean floor. Hydrothermal iron inputs are also challenging to quantify as they occur in one the planet's most inhospitable environments and the locations of all hydrothermal vents are unknown. A more convenient way to close the iron budget may be through isotopes of thorium and iron.

Removal in the surface ocean is partly due to biological uptake. Estimations of biological removal could come from models and constraints from observed Fe to carbon ratios in phytoplankton. The dominant removal term for iron through the water column is scavenging by sinking particles. Estimating the scavenging removal for iron is challenging because iron is constantly remineralized, desorbed from and scavenged onto sinking particles making, the total iron in sinking particles an unreliable estimate for scavenging removal. A convenient tracer to estimate scavenging removal would be produced uniformly throughout the oceans at a known rate and only be removed via scavenging by sinking particles. These properties happen to be that of ^{230}Thorium and ^{234}Thorium. ^{230}Thorium and ^{234}Thorium are produced uniformly throughout the oceans from decay of ^{234}Uranium and ^{238}Uranium respectively, and are only removed by scavenging of sinking particles (Savoye et al., 2006; Cheng et al., 2013). Knowing the rate of thorium production and water mass age would provide the thorium isotope concentration without removal due to scavenging. The difference between this calculated value and an observed value at the same location would provide an estimate of the amount of thorium that was lost to scavenging. Relating the amount of thorium scavenged to observed sinking mass fluxes would help to derive relationships of scavenged elements as a function of sinking mass and provide insights into scavenging losses. Data within low and high particle flux regions would be of particular importance as the upper and lower bounds of scavenging removal are not known. Both thorium isotopes and iron are highly particle reactive and it is thought that all trace metals susceptible to scavenging behave in a similar

fashion (Honeyman et al., 1988). Knowing the loss of thorium to scavenging would help quantify the loss of iron to scavenging.

Iron isotopes and their fractionation provide insights into iron source processes. Each iron source has a unique isotope fractionation. A study by Conway and John (2014) used iron isotopes and end-member mixing to construct a budget for iron sources along the GEOTRACES GA03 (west to east) transect in the Atlantic Ocean. This method does not calculate the flux of iron, but does provide the relative proportion of iron from each source. These values could be used in ocean biogeochemical models to help constrain iron source fluxes into the ocean. The GEOTRACES program will be instrumental for closing the iron budget by greatly expanding iron observations, and by constraining iron scavenging via thorium isotopes and iron sources from iron isotopes. The GEOTRACES campaigns measure a multitude of trace elements including thorium isotopes, iron isotopes and sinking mass fluxes. Programs such as GOSHIP, CLIVAR and GEOTRACES will be imperative to understanding the cycling of iron and other trace elements in the ocean. GEOTRACES has completed 41 basin transects with 21 planned over the next few years. GEOTRACES process studies will also provide insights into the mechanistic controls on marine iron cycling.

Bibliography

[1] N. S. Agawin, C. M. Duarte, S. Agusti, et al. Nutrient and temperature control of the contribution of picoplankton to phytoplankton biomass and production. *Limnology and Oceanography*, 45(3):591–600, 2000.

[2] A. Allen, J. Gillooly, and J. Brown. Linking the global carbon cycle to individual metabolism. *Functional Ecology*, 19(2):202–213, 2005.

[3] R. A. Armstrong, C. Lee, J. I. Hedges, S. Honjo, and S. G. Wakeham. A new, mechanistic model for organic carbon fluxes in the ocean based on the quantitative association of poc with ballast minerals. *Deep Sea Research Part II: Topical Studies in Oceanography*, 49(1):219–236, 2001.

[4] C. Arnosti, D. Repeta, and N. Blough. Rapid bacterial degradation of polysaccharides in anoxic marine systems. *Geochimica et Cosmochimica Acta*, 58(12):2639–2652, 1994.

[5] E. T. Baker and C. R. German. On the global distribution of hydrothermal vent fields. *Mid-ocean ridges*, pages 245–266, 2004.

[6] K. Barbeau. Photochemistry of organic iron (iii) complexing ligands in oceanic systems. *Photochemistry and Photobiology*, 82(6):1505–1516, 2006.

[7] K. Barbeau, E. Rue, K. Bruland, and A. Butler. Photochemical cycling of iron in the surface ocean mediated by microbial iron (iii)-binding ligands. *Nature*, 413(6854):409–413, 2001.

[8] K. Barbeau, E. L. Rue, C. G. Trick, K. W. Bruland, and A. Butler. Photochemical reactivity of siderophores produced by marine heterotrophic bacteria and cyanobacteria based on characteristic fe (iii) binding groups. *Limnology and Oceanography*, 48(3):1069–1078, 2003.

[9] S. Batchelli, F. L. Muller, K.-C. Chang, and C.-L. Lee. Evidence for strong but dynamic iron- humic colloidal associations in humic-rich coastal waters. *Environmental science & technology*, 44(22):8485–8490, 2010.

[10] S. E. Beaulieu, E. T. Baker, C. R. German, and A. Maffei. An authoritative global database for active submarine hydrothermal vent fields. *Geochemistry, Geophysics, Geosystems*, 14(11):4892–4905, 2013.

[11] M. J. Behrenfeld, E. Boss, D. A. Siegel, and D. M. Shea. Carbon-based ocean productivity and phytoplankton physiology from space. *Global biogeochemical cycles*, 19(1), 2005.

[12] S. A. Bennett, E. P. Achterberg, D. P. Connelly, P. J. Statham, G. R. Fones, and C. R. German. The distribution and stabilisation of dissolved fe in deep-sea hydrothermal plumes. *Earth and Planetary Science Letters*, 270(3):157–167, 2008.

[13] B. Bergquist, J. Wu, and E. Boyle. Variability in oceanic dissolved iron is dominated by the colloidal fraction. *Geochimica et Cosmochimica Acta*, 71(12):2960–2974, 2007.

[14] J. E. Bissinger, D. J. Montagnes, J. Sharples, and D. Atkinson. Predicting marine phytoplankton maximum growth rates from temperature: Improving on the eppley curve using quantile regression. *Limnology and Oceanography*, 53(2):487, 2008.

[15] L. Bopp, L. Resplandy, J. C. Orr, S. C. Doney, J. P. Dunne, M. Gehlen, P. Halloran, C. Heinze, T. Ilyina, R. Seferian, et al. Multiple stressors of ocean ecosystems in the 21st century: projections with cmip5 models. 2013.

[16] H. Boukhalfa and A. L. Crumbliss. Chemical aspects of siderophore mediated iron transport. *Biometals*, 15(4):325–339, 2002.

[17] P. Boyd and M. Ellwood. The biogeochemical cycle of iron in the ocean. *Nature Geoscience*, 3(10):675–682, 2010.

[18] P. Boyd, E. Ibisanmi, S. Sander, K. Hunter, and G. Jackson. Remineralization of upper ocean particles: Implications for iron biogeochemistry. *Limnology and Oceanography*, 55(3):1271, 2010.

[19] P. W. Boyd, C. S. Law, D. Hutchins, E. Abraham, P. L. Croot, M. Ellwood, R. Frew, M. Hadfield, J. Hall, S. Handy, et al. Fecycle: Attempting an iron biogeochemical budget from a mesoscale sf6 tracer experiment in unperturbed low iron waters. *Global Biogeochemical Cycles*, 19(4), 2005.

[20] M. Boye, J. Nishioka, P. L. Croot, P. Laan, K. R. Timmermans, and H. J. de Baar. Major deviations of iron complexation during 22 days of a mesoscale iron enrichment in the open southern ocean. *Marine chemistry*, 96(3):257–271, 2005.

[21] M. Boye, C. M. van den Berg, J. T. de Jong, H. Leach, P. Croot, and H. J. de Baar. Organic complexation of iron in the southern ocean. *Deep Sea Research Part I: Oceanographic Research Papers*, 48(6):1477–1497, 2001.

[22] E. Breitbarth, A. Oschlies, and J. LaRoche. Physiological constraints on the global distribution of trichodesmium? effect of temperature on diazotrophy. *Biogeosciences*, 4(1):53–61, 2007.

[23] J. H. Brown, J. F. Gillooly, A. P. Allen, V. M. Savage, and G. B. West. Toward a metabolic theory of ecology. *Ecology*, 85(7):1771–1789, 2004.

[24] K. N. Buck, K. E. Selph, and K. A. Barbeau. Iron-binding ligand production and copper speciation in an incubation experiment of antarctic peninsula shelf waters from the bransfield strait, southern ocean. *Marine Chemistry*, 122(1):148–159, 2010.

[25] K. N. Buck, B. Sohst, and P. N. Sedwick. The organic complexation of dissolved iron along the us geotraces (ga03) north atlantic section. *Deep Sea Research Part II: Topical Studies in Oceanography*, 116:152–165, 2015.

[26] R. M. Bundy, D. V. Biller, K. N. Buck, K. W. Bruland, and K. A. Barbeau. Distinct pools of dissolved iron-binding ligands in the surface and benthic boundary layer of the california current. *Limnol. Oceanogr*, 59(3):769–787, 2014.

[27] R. M. Bundy, M. Jiang, M. Carter, and K. A. Barbeau. Iron-binding ligands in the southern california current system: mechanistic studies. *Frontiers in Marine Science*, 3:27, 2016.

[28] A. Butler. Marine siderophores and microbial iron mobilization. *BioMetals*, 18(4):369–374, 2005.

[29] R. H. Byrne and D. R. Kester. Solubility of hydrous ferric oxide and iron speciation in seawater. *Marine Chemistry*, 4(3):255–274, 1976.

[30] A. Calbet, M. R. Landry, et al. Phytoplankton growth, microzooplankton grazing, and carbon cycling in marine systems. *Limnology and Oceanography*, 49(1):51–57, 2004.

[31] M.-E. Carr, M. A. Friedrichs, M. Schmeltz, M. N. Aita, D. Antoine, K. R. Arrigo, I. Asanuma, O. Aumont, R. Barber, M. Behrenfeld, et al. A comparison of global estimates of marine primary production from ocean color. *Deep Sea Research Part II: Topical Studies in Oceanography*, 53(5):741–770, 2006.

[32] B. Chen, M. R. Landry, B. Huang, and H. Liu. Does warming enhance the effect of microzooplankton grazing on marine phytoplankton in the ocean? *Limnology and Oceanography*, 57(2):519–526, 2012.

[33] H. Cheng, R. L. Edwards, C.-C. Shen, V. J. Polyak, Y. Asmerom, J. Woodhead, J. Hellstrom, Y. Wang, X. Kong, C. Spötl, et al. Improvements in 230 th dating, 230 th and 234 u half-life values, and u–th isotopic measurements by multi-collector inductively coupled plasma mass spectrometry. *Earth and Planetary Science Letters*, 371:82–91, 2013.

[34] J. J. Cole, S. Findlay, M. L. Pace, et al. Bacterial production in fresh and saltwater ecosystems: a cross-system overview. *Marine ecology progress series. Oldendorf*, 43(1):1–10, 1988.

[35] T. M. Conway and S. G. John. Quantification of dissolved iron sources to the north atlantic ocean. *Nature*, 511(7508):212–215, 2014.

[36] K. Croswell. The alchemy of the heavens. *The alchemy of the heavens., by Croswell, K.. Oxford University Press, Oxford (UK), 1996, XII+ 340 p., ISBN 0-19-286192-1, Price£ 7.99.*, 1, 1996.

[37] M.-H. Dai and J.-M. Martin. First data on trace metal level and behaviour in two major arctic river-estuarine systems (ob and yenisey) and in the adjacent kara sea, russia. *Earth and Planetary Science Letters*, 131(3):127–141, 1995.

[38] A. W. Dale, L. Nickelsen, F. Scholz, C. Hensen, A. Oschlies, and K. Wallmann. A revised global estimate of dissolved iron fluxes from marine sediments. *Global Biogeochemical Cycles*, 29(5):691–707, 2015.

[39] G. Danabasoglu, S. C. Bates, B. P. Briegleb, S. R. Jayne, M. Jochum, W. G. Large, S. Peacock, and S. G. Yeager. The ccsm4 ocean component. *Journal of Climate*, 25(5):1361–1389, 2012.

[40] H. J. de Baar and J. T. de Jong. Distributions, sources and sinks of iron in seawater. *IUPAC series on analytical and physical chemistry of environmental systems*, 7:123–254, 2001.

[41] Dixon, M. and Webb, C. *Enzymes, 3rd ed.* Academic Press, New York, NY, 1964.

[42] S. C. Doney, I. Lima, J. K. Moore, K. Lindsay, M. J. Behrenfeld, T. K. Westberry, N. Mahowald, D. M. Glover, and T. Takahashi. Skill metrics for confronting global upper ocean ecosystem-biogeochemistry models against field and remote sensing data. *Journal of Marine Systems*, 76(1):95–112, 2009.

[43] R. Duce. Sources, distributions, and fluxes of mineral aerosols and their relationship to climate. *Aerosol forcing of climate*, 6:43–72, 1995.

[44] R. A. Duce and N. W. Tindale. Atmospheric transport of iron and its deposition in the ocean. *Limnology and Oceanography*, 36(8):1715–1726, 1991.

[45] H. Ducklow. Bacterial production and biomass in the oceans. *Microbial ecology of the oceans*, 1:85–120, 2000.

[46] J. P. Dunne, J. G. John, E. Shevliakova, R. J. Stouffer, J. P. Krasting, S. L. Malyshev, P. Milly, L. T. Sentman, A. J. Adcroft, W. Cooke, et al. Gfdls esm2 global coupled climate–carbon earth system models. part ii: Carbon system formulation and baseline simulation characteristics*. *Journal of Climate*, 26(7):2247–2267, 2013.

[47] V. A. Elrod, W. M. Berelson, K. H. Coale, and K. S. Johnson. The flux of iron from continental shelf sediments: A missing source for global budgets. *Geophysical Research Letters*, 31(12), 2004.

[48] R. W. Eppley. Temperature and phytoplankton growth in the sea. *Fish. Bull*, 70(4):1063–1085, 1972.

[49] L. I. Falcón, S. Pluvinage, and E. J. Carpenter. Growth kinetics of marine unicellular n2-fixing cyanobacterial isolates in continuous culture in relation to phosphorus and temperature. *Marine Ecology Progress Series*, 285:3–9, 2005.

[50] R. A. Feely, M. Lewison, G. J. Massoth, G. Robert-Baldo, J. W. Lavelle, R. H. Byrne, K. L. Von Damm, and H. C. Curl. Composition and dissolution of black smoker particulates from active vents on the juan de fuca ridge. *Journal of Geophysical Research: Solid Earth*, 92(B11):11347–11363, 1987.

[51] Z. Finkel, A. Quigg, J. Raven, J. Reinfelder, O. Schofield, and P. Falkowski. Irradiance and the elemental stoichiometry of marine phytoplankton. *Limnology and Oceanography*, 51(6):2690–2701, 2006.

[52] R. D. Frew, D. A. Hutchins, S. Nodder, S. Sanudo-Wilhelmy, A. Tovar-Sanchez, K. Leblanc, C. E. Hare, and P. W. Boyd. Particulate iron dynamics during fecycle in subantarctic waters southeast of new zealand. *Global Biogeochemical Cycles*, 20(1), 2006.

[53] I. Y. Fung, S. K. Meyn, I. Tegen, S. C. Doney, J. G. John, and J. K. Bishop. Iron supply and demand in the upper ocean. *Global Biogeochem. Cycles*, 14(1):281–295, 2000.

[54] G. Gebbie and P. Huybers. The mean age of ocean waters inferred from radiocarbon observations: Sensitivity to surface sources and accounting for mixing histories. *Journal of Physical Oceanography*, 42(2):291–305, 2012.

[55] P. R. Gent, G. Danabasoglu, L. J. Donner, M. M. Holland, E. C. Hunke, S. R. Jayne, D. M. Lawrence, R. B. Neale, P. J. Rasch, M. Vertenstein, et al. The community climate system model version 4. *Journal of Climate*, 24(19):4973–4991, 2011.

[56] L. Gerringa, M. Rijkenberg, V. Schoemann, P. Laan, and H. de Baar. Organic complexation of iron in the west atlantic ocean. *Marine Chemistry*, 177:434–446, 2015.

[57] L. J. Gerringa, A.-C. Alderkamp, P. Laan, C.-E. Thuroczy, H. J. De Baar, M. M. Mills, G. L. van Dijken, H. van Haren, and K. R. Arrigo. Iron from melting glaciers fuels the phytoplankton blooms in amundsen sea (southern ocean): Iron biogeochemistry. *Deep Sea Research Part II: Topical Studies in Oceanography*, 71:16–31, 2012.

[58] R. J. Gibbs. Mechanisms of trace metal transport in rivers. *Science*, 180(4081):71–73, 1973.

[59] M. Gledhill and K. N. Buck. The organic complexation of iron in the marine environment: a review. *The microbial ferrous wheel: iron cycling in terrestrial, freshwater, and marine environments*, 29, 2012.

[60] M. Gledhill, P. McCormack, S. Ussher, E. P. Achterberg, R. F. C. Mantoura, and P. J. Worsfold. Production of siderophore type chelates by mixed bacterioplankton populations in nutrient enriched seawater incubations. *Marine Chemistry*, 88(1):75–83, 2004.

[61] M. Gledhill and C. M. van den Berg. Determination of complexation of iron (iii) with natural organic complexing ligands in seawater using cathodic stripping voltammetry. *Marine Chemistry*, 47(1):41–54, 1994.

[62] J. C. Goldman and E. J. Carpenter. A kinetic approach to the effect of temperature on algal growth. *Limnology and Oceanography*, 19(5):756–766, 1974.

[63] G. Group et al. The geotraces intermediate data product 2014. *Marine Chemistry*, 177:1–8, 2015.

[64] J. Hand, N. Mahowald, Y. Chen, R. Siefert, C. Luo, A. Subramaniam, and I. Fung. Estimates of atmospheric-processed soluble iron from observations and a global mineral aerosol model: Biogeochemical implications. *Journal of Geophysical Research: Atmospheres*, 109(D17), 2004.

[65] C. S. Hassler, V. Schoemann, C. M. Nichols, E. C. Butler, and P. W. Boyd. Saccharides enhance iron bioavailability to southern ocean phytoplankton. *Proceedings of the National Academy of Sciences*, 108(3):1076–1081, 2011.

[66] N. Hertkorn, R. Benner, M. Frommberger, P. Schmitt-Kopplin, M. Witt, K. Kaiser, A. Kettrup, and J. I. Hedges. Characterization of a major refractory component of marine dissolved organic matter. *Geochimica et Cosmochimica Acta*, 70(12):2990–3010, 2006.

[67] R. C. Hider and X. Kong. Chemistry and biology of siderophores. *Natural product reports*, 27(5):637–657, 2010.

[68] K. Hirose. Chemical speciation of trace metals in seawater: a review. *Analytical Sciences*, 22(8):1055–1063, 2006.

[69] B. D. Honeyman, L. S. Balistrieri, and J. W. Murray. Oceanic trace metal scavenging: the importance of particle concentration. *Deep Sea Research Part A. Oceanographic Research Papers*, 35(2):227–246, 1988.

[70] K. A. Hunter and P. W. Boyd. Iron-binding ligands and their role in the ocean biogeochemistry of iron. *Environmental Chemistry*, 4(4):221–232, 2007.

[71] J. W. Hurrell, M. M. Holland, P. R. Gent, S. Ghan, J. E. Kay, P. Kushner, J.-F. Lamarque, W. G. Large, D. Lawrence, K. Lindsay, et al. The community earth system model: a framework for collaborative research. *Bulletin of the American Meteorological Society*, 94(9):1339–1360, 2013.

[72] D. Hutchins and K. Bruland. Grazer-mediated regeneration and assimilation of fe, zn and mn from planktonic prey. *Marine Ecology-Progress Series*, 110:259–259, 1994.

[73] E. Ibisanmi, S. G. Sander, P. W. Boyd, A. R. Bowie, and K. A. Hunter. Vertical distributions of iron-(iii) complexing ligands in the southern ocean. *Deep Sea Research Part II: Topical Studies in Oceanography*, 58(21):2113–2125, 2011.

[74] T. Jickells, Z. An, K. K. Andersen, A. Baker, G. Bergametti, N. Brooks, J. Cao, P. Boyd, R. Duce, K. Hunter, et al. Global iron connections between desert dust, ocean biogeochemistry, and climate. *science*, 308(5718):67–71, 2005.

[75] T. D. Jickells and L. J. Spokes. Atmospheric iron inputs to the oceans. *IUPAC series on analytical and physical chemistry of environmental systems*, 7:85–122, 2001.

[76] K. S. Johnson, F. P. Chavez, and G. E. Friederich. Continental-shelf sediment as a primary source of iron for coastal phytoplankton. *Nature*, 398(6729):697–700, 1999.

[77] K. S. Johnson, R. M. Gordon, and K. H. Coale. What controls dissolved iron concentrations in the world ocean? *Marine Chemistry*, 57(3):137–161, 1997.

[78] Y. Kaufman, I. Koren, L. Remer, D. Tanré, P. Ginoux, and S. Fan. Dust transport and deposition observed from the terra-moderate resolution imaging spectroradiometer (modis) spacecraft over the atlantic ocean. *Journal of Geophysical Research: Atmospheres*, 110(D10), 2005.

[79] D. L. Kirchman et al. Oceanography-microbial ferrous wheel. *Nature*, 383(6598):303–304, 1996.

[80] R. Krachler, F. Jirsa, and S. Ayromlou. Factors influencing the dissolved iron input by river water to the open ocean. *Biogeosciences*, 2(4):311–315, 2005.

[81] K. Kuma, J. Nishioka, and K. Matsunaga. Controls on iron (iii) hydroxide solubility in seawater: the influence of ph and natural organic chelators. *Limnology and Oceanography*, 41(3):396–407, 1996.

[82] L. M. Laglera, G. Battaglia, and C. M. van den Berg. Determination of humic substances in natural waters by cathodic stripping voltammetry of their complexes with iron. *Analytica chimica acta*, 599(1):58–66, 2007.

[83] C. Lamborg, K. Buesseler, and P. Lam. Sinking fluxes of minor and trace elements in the north pacific ocean measured during the vertigo program. *Deep Sea Research Part II: Topical Studies in Oceanography*, 55(14):1564–1577, 2008.

[84] M. Landry and R. Hassett. Estimating the grazing impact of marine microzooplankton. *Marine biology*, 67(3):283–288, 1982.

[85] C. Laufkötter, M. Vogt, N. Gruber, M. Aita-Noguchi, O. Aumont, L. Bopp, E. Buitenhuis, S. Doney, J. Dunne, T. Hashioka, et al. Drivers and uncertainties of future global marine primary production in marine ecosystem models. *Biogeosciences*, 12:6955–6984, 2015.

[86] B.-G. Lee and N. S. Fisher. Release rates of trace elements and protein from decomposing planktonic debris. 1. phytoplankton debris. *Journal of marine research*, 51(2):391–421, 1993.

[87] R. T. Letscher, F. Primeau, and J. K. Moore. Nutrient budgets in the subtropical ocean gyres dominated by lateral transport. *Nature Geoscience*, 9(11):815–819, 2016.

[88] X. Liu and F. J. Millero. The solubility of iron in seawater. *Marine Chemistry*, 77(1):43–54, 2002.

[89] M. C. Long, K. Lindsay, S. Peacock, J. K. Moore, and S. C. Doney. Twentieth-century oceanic carbon uptake and storage in cesm1 (bgc)*. *Journal of Climate*, 26(18):6775–6800, 2013.

[90] Á. López-Urrutia, E. San Martin, R. P. Harris, and X. Irigoien. Scaling the metabolic balance of the oceans. *Proceedings of the National Academy of Sciences*, 103(23):8739–8744, 2006.

[91] C. Luo, N. Mahowald, T. Bond, P. Chuang, P. Artaxo, R. Siefert, Y. Chen, and J. Schauer. Combustion iron distribution and deposition. *Global Biogeochemical Cycles*, 22(1), 2008.

[92] C. Luo, N. M. Mahowald, and J. Del Corral. Sensitivity study of meteorological parameters on mineral aerosol mobilization, transport, and distribution. *Journal of Geophysical Research: Atmospheres*, 108(D15), 2003.

[93] M. T. Maldonado, M. P. Hughes, E. L. Rue, and M. L. Wells. The effect of fe and cu on growth and domoic acid production by pseudo-nitzschia multiseries and pseudo-nitzschia australis. *Limnology and Oceanography*, 47(2):515–526, 2002.

[94] J. Martinez, G. Zhang, P. Holt, H.-T. Jung, C. Carrano, M. Haygood, and A. Butler. Self-assembling amphiphilic siderophores from marine bacteria. *Science*, 287(5456):1245–1247, 2000.

[95] C. Measures, W. Landing, M. Brown, and C. Buck. High-resolution al and fe data from the atlantic ocean clivar-co2 repeat hydrography a16n transect: Extensive linkages between atmospheric dust and upper ocean geochemistry. *Global Biogeochemical Cycles*, 22(1), 2008.

[96] N. Meskhidze, W. Chameides, and A. Nenes. Dust and pollution: a recipe for enhanced ocean fertilization? *Journal of Geophysical Research: Atmospheres*, 110(D3), 2005.

[97] C. E. Mioni, L. Poorvin, and S. W. Wilhelm. Virus and siderophore-mediated transfer of available fe between heterotrophic bacteria: characterization using an fe-specific bioreporter. *Aquatic Microbial Ecology*, 41(3):233–245, 2005.

[98] K. Misumi, K. Lindsay, J. K. Moore, S. C. Doney, F. O. Bryan, D. Tsumune, and Y. Yoshida. The iron budget in ocean surface waters in the 20th and 21st centuries: projections by the community earth system model version 1. *Biogeosciences*, 11(1), 2014.

[99] K. Misumi, K. Lindsay, J. K. Moore, S. C. Doney, D. Tsumune, and Y. Yoshida. Humic substances may control dissolved iron distributions in the global ocean: Implications from numerical simulations. *Global Biogeochemical Cycles*, 27(2):450–462, 2013.

[100] J. Moore and O. Braucher. Sedimentary and mineral dust sources of dissolved iron to the world ocean. *Biogeosciences*, 5(3), 2008.

[101] J. K. Moore, S. C. Doney, D. M. Glover, and I. Y. Fung. Iron cycling and nutrient-limitation patterns in surface waters of the world ocean. *Deep Sea Research Part II: Topical Studies in Oceanography*, 49(1):463–507, 2001.

[102] J. K. Moore, S. C. Doney, and K. Lindsay. Upper ocean ecosystem dynamics and iron cycling in a global three-dimensional model. *Global Biogeochemical Cycles*, 18(4), 2004.

[103] J. K. Moore, K. Lindsay, S. C. Doney, M. C. Long, and K. Misumi. Marine ecosystem dynamics and biogeochemical cycling in the community earth system model [cesm1 (bgc)]: Comparison of the 1990s with the 2090s under the rcp4. 5 and rcp8. 5 scenarios. *Journal of Climate*, 26(23):9291–9312, 2013.

[104] J. W. Morgan and E. Anders. Chemical composition of earth, venus, and mercury. *Proceedings of the National Academy of Sciences*, 77(12):6973–6977, 1980.

[105] C. Moulin, C. E. Lambert, F. Dulac, U. Dayan, et al. Control of atmospheric export of dust from north africa by the north atlantic oscillation. *Nature*, 387(6634):691, 1997.

[106] Y. Nozaki, H.-S. Yang, and M. Yamada. Scavenging of thorium in the ocean. *Journal of Geophysical Research: Oceans*, 92(C1):772–778, 1987.

[107] I. Obernosterer, U. Christaki, D. Lefèvre, P. Catala, F. Van Wambeke, and P. Lebaron. Rapid bacterial mineralization of organic carbon produced during a phytoplankton bloom induced by natural iron fertilization in the southern ocean. *Deep Sea Research Part II: Topical Studies in Oceanography*, 55(5):777–789, 2008.

[108] P. Parekh, M. J. Follows, and E. A. Boyle. Decoupling of iron and phosphate in the global ocean. *Global Biogeochemical Cycles*, 19(2), 2005.

[109] F. Peters. Prediction of planktonic protistan grazing rates. *Limnology and Oceanography*, 39(1):195–206, 1994.

[110] L. Poorvin, J. M. Rinta-Kanto, D. A. Hutchins, and S. W. Wilhelm. Viral release of iron and its bioavailability to marine plankton. *Limnology and Oceanography*, 49(5):1734–1741, 2004.

[111] R. T. Powell and A. Wilson-Finelli. Photochemical degradation of organic iron complexing ligands in seawater. *Aquatic Sciences*, 65(4):367–374, 2003.

[112] J. M. Prospero, F.-X. Collard, J. Molinié, and A. Jeannot. Characterizing the annual cycle of african dust transport to the caribbean basin and south america and its impact on the environment and air quality. *Global Biogeochemical Cycles*, 28(7):757–773, 2014.

[113] J. M. Prospero, P. Ginoux, O. Torres, S. E. Nicholson, and T. E. Gill. Environmental characterization of global sources of atmospheric soil dust identified with the nimbus 7 total ozone mapping spectrometer (toms) absorbing aerosol product. *Reviews of geophysics*, 40(1), 2002.

[114] R. Raiswell, L. Benning, L. Davidson, and M. Tranter. Nanoparticulate bioavailable iron minerals in icebergs and glaciers. *Mineralogical Magazine*, 72(1):345–348, 2008.

[115] J. Raven. The twelfth tansley lecture. small is beautiful: the picophytoplankton. *Functional ecology*, 12(4):503–513, 1998.

[116] J. A. Raven, M. C. Evans, and R. E. Korb. The role of trace metals in photosynthetic electron transport in o2-evolving organisms. *Photosynthesis Research*, 60(2-3):111–150, 1999.

[117] J. A. Raven and R. J. Geider. Temperature and algal growth. *New phytologist*, 110(4):441–461, 1988.

[118] A. Regaudie-de Gioux and C. M. Duarte. Temperature dependence of planktonic metabolism in the ocean. *Global Biogeochemical Cycles*, 26(1), 2012.

[119] R. T. Reid, D. H. Livet, D. J. Faulkner, and A. Butler. A siderophore from a marine bacterium with an exceptional ferric ion affinity constant. 1993.

[120] J. A. Resing, P. N. Sedwick, C. R. German, W. J. Jenkins, J. W. Moffett, B. M. Sohst, and A. Tagliabue. Basin-scale transport of hydrothermal dissolved metals across the south pacific ocean. *Nature*, 523(7559):200–203, 2015.

[121] M. J. Rijkenberg, L. J. Gerringa, I. Velzeboer, K. R. Timmermans, A. G. Buma, and H. J. de Baar. Iron-binding ligands in dutch estuaries are not affected by uv induced photochemical degradation. *Marine Chemistry*, 100(1):11–23, 2006.

[122] M. J. Rijkenberg, R. Middag, P. Laan, L. J. Gerringa, H. M. van Aken, V. Schoemann, J. T. de Jong, and H. J. de Baar. The distribution of dissolved iron in the west atlantic ocean. *PloS one*, 9(6):e101323, 2014.

[123] J. M. Rose and D. A. Caron. Does low temperature constrain the growth rates of heterotrophic protists? evidence and implications for algal blooms in cold waters. *Limnology and Oceanography*, 52(2):886–895, 2007.

[124] E. L. Rue and K. W. Bruland. Complexation of iron (iii) by natural organic ligands in the central north pacific as determined by a new competitive ligand equilibration/adsorptive cathodic stripping voltammetric method. *Marine Chemistry*, 50(1):117–138, 1995.

[125] E. L. Rue and K. W. Bruland. The role of organic complexation on ambient iron chemistry in the equatorial pacific ocean and the response of a mesoscale iron addition experiment. *Limnology and Oceanography*, 42(5):901–910, 1997.

[126] G. Sarthou, D. Vincent, U. Christaki, I. Obernosterer, K. R. Timmermans, and C. P. Brussaard. The fate of biogenic iron during a phytoplankton bloom induced by natural fertilisation: Impact of copepod grazing. *Deep Sea Research Part II: Topical Studies in Oceanography*, 55(5):734–751, 2008.

[127] M. Sasakawa and M. Uematsu. Relative contribution of chemical composition to acidification of sea fog (stratus) over the northern north pacific and its marginal seas. *Atmospheric Environment*, 39(7):1357–1362, 2005.

[128] M. Sato, S. Takeda, and K. Furuya. Iron regeneration and organic iron (iii)-binding ligand production during in situ zooplankton grazing experiment. *Marine Chemistry*, 106(3):471–488, 2007.

[129] N. Savoye, C. Benitez-Nelson, A. B. Burd, J. K. Cochran, M. Charette, K. O. Buesseler, G. A. Jackson, M. Roy-Barman, S. Schmidt, and M. Elskens. 234 th sorption and export models in the water column: a review. *Marine Chemistry*, 100(3):234–249, 2006.

[130] C. Schlosser and P. Croot. Controls on seawater fe (iii) solubility in the mauritanian upwelling zone. *Geophysical Research Letters*, 36(18), 2009.

[131] C. Schlosser, J. K. Klar, B. D. Wake, J. T. Snow, D. J. Honey, E. M. S. Woodward, M. C. Lohan, E. P. Achterberg, and C. M. Moore. Seasonal itcz migration dynamically controls the location of the (sub) tropical atlantic biogeochemical divide. *Proceedings of the National Academy of Sciences*, 111(4):1438–1442, 2014.

[132] P. N. Sedwick, E. R. Sholkovitz, and T. M. Church. Impact of anthropogenic combustion emissions on the fractional solubility of aerosol iron: Evidence from the sargasso sea. *Geochemistry, Geophysics, Geosystems*, 8(10), 2007.

[133] R. Strzepek, M. Maldonado, J. Higgins, J. Hall, K. Safi, S. Wilhelm, and P. Boyd. Spinning the ferrous wheel: The importance of the microbial community in an iron budget during the fecycle experiment. *Global biogeochemical cycles*, 19(4), 2005.

[134] W. G. Sunda. Trace metal interactions with marine phytoplankton. *Biological Oceanography*, 6(5-6):411–442, 1989.

[135] W. G. Sunda. Bioavailability and bioaccumulation of iron in the sea. *IUPAC Series on Analytical and Physical Chemistry of Environmental Systems*, 7:41–84, 2001.

[136] W. G. Sunda and S. A. Huntsman. Interrelated influence of iron, light and cell size on marine phytoplankton growth. *Nature*, 390(6658):389–392, 1997.

[137] W. G. Sunda and S. A. Huntsman. Interactive effects of external manganese, the toxic metals copper and zinc, and light in controlling cellular manganese and growth in a coastal diatom. *Limnology and Oceanography*, 43(7):1467–1475, 1998.

[138] A. Tagliabue, O. Aumont, R. DeAth, J. P. Dunne, S. Dutkiewicz, E. Galbraith, K. Misumi, J. K. Moore, A. Ridgwell, E. Sherman, et al. How well do global ocean biogeochemistry models simulate dissolved iron distributions? *Global Biogeochemical Cycles*, 2015.

[139] A. Tagliabue, L. Bopp, J.-C. Dutay, A. R. Bowie, F. Chever, P. Jean-Baptiste, E. Bucciarelli, D. Lannuzel, T. Remenyi, G. Sarthou, et al. Hydrothermal contribution to the oceanic dissolved iron inventory. *Nature Geoscience*, 3(4):252–256, 2010.

[140] A. Tagliabue, T. Mtshali, O. Aumont, A. Bowie, M. Klunder, A. Roychoudhury, and S. Swart. A global compilation of dissolved iron measurements: focus on distributions and processes in the southern ocean. *Biogeosciences*, 9(6):2333–2349, 2012.

[141] J. Taucher and A. Oschlies. Can we predict the direction of marine primary production change under global warming? *Geophysical Research Letters*, 38(2), 2011.

[142] B. M. Toner, M. A. Marcus, K. J. Edwards, O. J. Rouxel, and C. R. German. Measuring the form of iron in hydrothermal plume particles. 2012.

[143] B. S. Twining and S. B. Baines. The trace metal composition of marine phytoplankton. *Annual review of marine science*, 5:191–215, 2013.

[144] P. Van Cappellen and Y. Wang. Cycling of iron and manganese in surface sediments; a general theory for the coupled transport and reaction of carbon, oxygen, nitrogen, sulfur, iron, and manganese. *American Journal of Science*, 296(3):197–243, 1996.

[145] C. Völker and A. Tagliabue. Modeling organic iron-binding ligands in a three-dimensional biogeochemical ocean model. *Marine Chemistry*, 173:67–77, 2015.

[146] L. Vong, A. Laës, and S. Blain. Determination of iron–porphyrin-like complexes at nanomolar levels in seawater. *Analytica chimica acta*, 588(2):237–244, 2007.

[147] T. Wagener, E. Pulido-Villena, and C. Guieu. Dust iron dissolution in seawater: Results from a one-year time-series in the mediterranean sea. *Geophysical Research Letters*, 35(16), 2008.

[148] T. Westberry, M. Behrenfeld, D. Siegel, and E. Boss. Carbon-based primary productivity modeling with vertically resolved photoacclimation. *Global Biogeochemical Cycles*, 22(2), 2008.

[149] A. E. Witter, B. L. Lewis, and G. W. Luther III. Iron speciation in the arabian sea. *Deep Sea Research Part II: Topical Studies in Oceanography*, 47(7):1517–1539, 2000.

[150] J. Wu and E. Boyle. Iron in the sargasso sea: Implications for the processes controlling dissolved fe distribution in the ocean. *Global Biogeochemical Cycles*, 16(4), 2002.

[151] U. L. Zweifel, B. Norrman, and A. Hagstrom. Consumption of dissolved organic carbon by marine bacteria and demand for inorganic nutrients. *Marine Ecology-Progress Series*, 101:23–23, 1993.